A numerical investigation and optimization by machine learning for the growth of InGaSb crystals with a flatter interface by Vertical Gradient Freezing method under microgravity and normal gravity conditions

Rachid Ghritli

September 2023

A numerical investigation and optimization by machine learning for the growth of InGaSb crystals with a flatter interface by Vertical Gradient Freezing method under microgravity and normal gravity conditions

A dissertation submitted to
THE GRADUATE SCHOOL OF ENGINEERING SCIENCE
OSAKA UNIVERSITY
in partial fulfillment of the requirements for the degree of
DOCTOR OF PHILOSOPHY IN ENGINEERING

BY

Rachid Ghritli

September 2023

Abstract

Semiconductors materials represent the foundation of present-day electronic devices. InGaSb is an III-V semiconductor compound that became of great interest, thanks to having tunable properties between its binary compounds InSb and GaSb. The lattice constant and wavelength of this ternary alloy can be varied in the range 6.096 ~ 6.48 A and 1.7 ~ 6.8 μm, respectively. This characteristic makes InGaSb suitable for developing new thermophotovoltaic (TPV) devices, gas sensors and infrared (IR) detectors, etc. High quality crystals are naturally desirable as the substrate for device applications. However, the growth of such homogeneous InGaSb alloy bulk crystals with uniform compositions on earth is difficult because of the adverse effects of natural convection, compositional segregation, and heat and mass transfer in the vicinity of the dissolution and growth interfaces. These undesirable effects can be minimized under microgravity, which is an appropriate environment for investigating the growth kinetics and gaining deeper insight into the transport phenomena. The use of adequate growth conditions is crucial in order to avoid undesirable solid-liquid interface shape deformations and compositional non-uniformity. Hence, we carried out a numerical simulation analysis in order to determine the conditions for an optimum interface shape in the growth of InGaSb crystals using a combination of different techniques.

In the first place, as it is important to employ accurate physical properties in our numerical model, the diffusion coefficient of GaSb in InSb melt was estimated by using the microgravity experimental results performed onboard the International Space Station (ISS), where the effect of natural convection was minimized. Furthermore, it was deduced that the growth rate is dominated by the solute diffusion in the melt. the crystal growth rate was well explained by adopting a diffusion coefficient with function of GaSb concentration, obtained by analyzing the available experimental results and utilizing Bayesian optimization.

Then, the growth of high-quality InGaSb crystals by Vertical Gradient Freezing (VGF) method under microgravity was numerically simulated, with a focus on controlling growth interface shape which directly affects the quality and homogeneity of the grown crystals. Machine learning tools were used to optimize the growth conditions; Initially, Bayesian optimization was utilized to search for the most favorable temperature gradient that promotes a desirable flatter growth interface shape. Afterwards, an adaptive control recipe (reinforcement learning model) was developed. The system was subjected to a lower temperature gradient near the feed crystal

and to crucible rotation with a rate ranging according to the obtained optimal strategy. Results showed that the interface deformation is considerably reduced, and a flatter growth interface could be maintained. The growth rate and solute concentration uniformity were also improved. Subsequently, growth of InGaSb crystals by VGF method under normal gravity was numerically investigated. In order to obtain a flatter growth interface and better compositional uniformity in the melt, the applications of crucible rotation and external magnetic field are considered. We carried out a numerical study to optimize growth parameters for these purposes and used Bayesian optimization to have a fast search for the most favorable control parameters. Such an optimization has led to a significant reduction in the growth interface deflection and a flatter growth interface was maintained during the entire growth process. Strength of natural convection in the melt was minimized and melt solute uniformity was improved. The growth rate was also increased without compromising crystal quality.

The findings of this research study demonstrate the effectiveness of employing crucible rotation, external forces, and optimized temperature gradient for achieving enhanced control over the growth interface shape and composition uniformity. Additionally, machine learning proves to be a valuable tool in the search for optimal control parameters. This thesis not only contributes to a deeper understanding of InGaSb crystal growth process under normal gravity but also lays the groundwork for future growth experiments conducted under Earth's gravity level.

Contents

Chapter 1

General introduction

1.1 Background

1.1.1 III-V semiconductors

Semiconductors play a crucial role in the modern world, serving as the foundation for numerous technological advancements. They are essential components of electronic devices, enabling the development of computers, smartphones, televisions, and countless other gadgets we rely on in our daily lives [1, 2]. Among the various types of semiconductors, III-V group semiconductors hold particular significance due to their unique properties and wide-ranging applications [3, 4]. III-V group semiconductors refer to compounds composed of elements from groups III and V of the periodic table, such as Gallium Arsenide (GaAs), Gallium Antimonide (GaSb), Indium Antimonide (InSb), Indium Phosphide (InP), and Gallium Nitride (GaN). These materials possess several advantageous characteristics that make them highly desirable for various technological fields [5, 6].

One of the key advantages of III-V group semiconductors is their direct bandgap, which allows for efficient absorption and emission of light. This property makes them ideal for optoelectronic applications, including light-emitting diodes (LEDs), lasers, solar cells, and photodetectors [7, 8, 9].

Furthermore, III-V group semiconductors exhibit excellent electron mobility, which refers to the ease with which electrons can move through the material. This high mobility makes them suitable for high-frequency and high-power electronic devices, such as transistors and amplifiers. They are commonly used in radio-frequency (RF) amplifiers, microwave devices, and satellite communications, where high-speed signal processing and efficient power handling are crucial.

In addition, III-V group semiconductors have shown exceptional performance in the field of power electronics. Their high breakdown voltage, high thermal conductivity, and excellent power-handling capabilities make them ideal for applications such as power amplifiers, voltage converters, and energy-efficient devices. These materials have the potential to revolutionize

energy systems, enabling more efficient power generation, storage, and distribution [10].

Figure 1.1 illustrates the lattice constant, band gap energy, and band gap wavelength of common III-V compound semiconductors. Among these III-V group semiconductors, including GaN, InN, GaP, InP, GaSb, and InSb, higher mobility is observed, making them suitable for high-speed electronic device applications [4]. Moreover, III-V compounds such as GaSb, GaAs, and InSb exhibit longer wavelengths compared to silicon, which is widely used in electronic devices. Therefore, the advancement of optoelectronic device applications is closely connected to the development of III-V semiconductor properties. As shown in **Fig. 1.1**, the lattice constant and wavelength and structural properties of III-V alloys can be varied from GaP to InSb by forming ternary and quaternary alloys. Nonetheless, the growth of quaternary alloys is a complex and expensive process. A more feasible and cost-effective approach involves tuning the material properties by forming ternary alloys, such as InGaAs, AlGaAs, InGaN, AlGaN, InGaSb, and AlGaSb, within the desired range. The tunable lattice constant of these ternary alloys enables the development of semiconductor heterostructures with enhanced functional properties [11]. The present thesis primarily centers on the investigation and growth of InGaSb alloy.

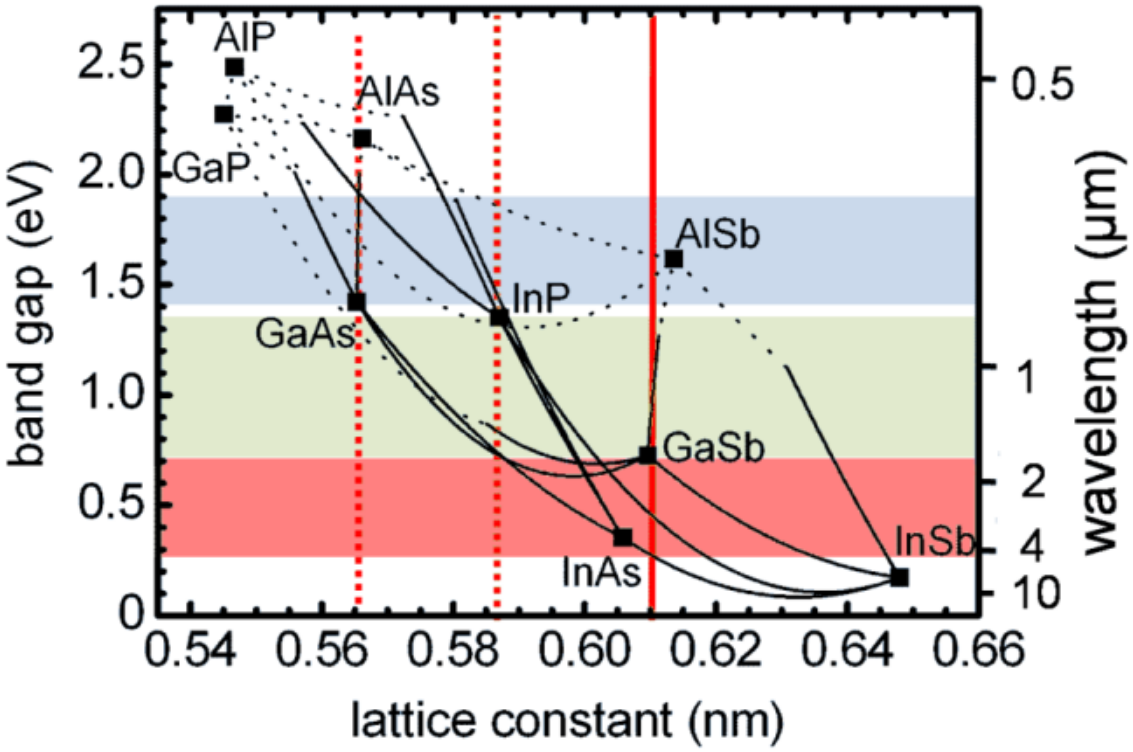

Figure 1.1. Lattice constant, band gap energy and band gap wavelength for common III-V compound semiconductors [4].

1.1.2 Importance of InGaSb alloy

InGaSb (Indium Gallium Antimonide) is a member of the III-V group semiconductors and holds significant importance in various technological applications due to its unique properties. Its importance stems from its favorable bandgap and energy band structure, which make it suitable for a range of optoelectronic and electronic devices [12, 13]. InGaSb exhibits a tunable lattice constant and wavelength ranging from 6.096 to 6.479 A and 1.7 to 6.8 μm, respectively. Some of the key areas where this alloy finds application include [14, 15, 16, 17, 18]:

- Infrared detectors and imaging: InGaSb exhibits a narrow bandgap, typically ranging from 0.17 eV to 0.74 eV, depending on the Indium and Gallium composition. This makes it well-suited for infrared detectors and imaging systems, especially in the mid- to long-wavelength infrared (MWIR-LWIR) range. InGaSb-based photodiodes and focal plane arrays (FPAs) enable the detection and imaging of thermal radiation, making them valuable in applications such as night vision, surveillance, remote sensing, and thermal imaging cameras [19].

- High-Speed electronics: InGaSb possesses excellent electron transport properties, including high electron mobility, which makes it suitable for high-speed electronic devices. InGaSb-based transistors and integrated circuits can operate at high frequencies, making them valuable for applications such as high-speed communication systems, microwave electronics, and signal processing.

- Thermophotovoltaic cells: InGaSb has been explored for thermophotovoltaic (TPV) devices, which convert thermal radiation into electricity. TPV systems utilizing InGaSb as the photovoltaic material can harness waste heat from industrial processes or other sources and convert it into usable electrical power. This has potential applications in energy harvesting and efficient power generation [20].

- Quantum wells and superlattices: InGaSb is frequently used in the construction of quantum wells and superlattices, where thin layers of different materials are stacked together to create unique electronic properties. These structures enable the design of novel electronic and optoelectronic devices with tailored energy levels, bandgaps, and charge carrier dynamics. InGaSb-based quantum well structures have been employed in lasers, infrared photodetectors, and quantum cascade lasers, which operate in the mid- to long-wavelength infrared regions [4].

- Nanowires: Material-wise, the antimonide family brings unique advantages complementary to other III–V nanowires, such as large wavelength coverage (from near- toward long-wavelength infrared), type II and type III band alignments (e.g. in InAs/GaSb), useful for photodetector and solar energy applications, and the highest hole and electron

mobilities, respectively for GaSb and InSb. These advantages have already been used in devices based on binary nanowires. Further developments will require the use of ternary Sb-based nanowires. In particular, it has been shown that the Er-doped InGaSb alloy is a promising candidate for thermoelectricity and also the nanowire geometry reduces the thermal conductivity. Therefore, the epitaxial growth of the Er-doped InGaSb nanowires could make a very good thermoelectric candidate in the future [21].

- Research in fundamental physics: InGaSb is of interest to researchers studying condensed matter physics, semiconductor physics, and related fields. Its unique electronic and optical properties provide opportunities for investigating fundamental phenomena and exploring novel quantum effects. Researchers use InGaSb in experiments related to quantum transport, spintronics, and topological insulators, contributing to our understanding of advanced materials and their behavior.

The importance of InGaSb semiconductor extends beyond these specific applications, as ongoing research and development continue to explore new avenues for its utilization. By harnessing its unique properties, scientists and engineers can develop innovative devices and technologies that improve areas such as sensing, communication, energy efficiency, and fundamental scientific research.

1.1.3 Issues related to the growth of InGaSb under terrestrial conditions

To successfully grow the ternary alloy InGaSb, it is crucial to comprehend the properties of its binary constituents, InSb and GaSb. The growth process of InGaSb is influenced by multiple parameters due to the distinct properties of its constituents. Segregation, constitutional supercooling, and convection are one of the factors that impact the growth and quality of InGaSb crystals. The following paragraphs will elaborate on the origins of these factors, their effects on the resulting crystal, and potential solutions to overcome them.

Natural convection

The growth of InGaSb crystals under normal gravity conditions can pose several challenges and issues [22, 23, 24, 25, 26]. For instance, density gradients in the growth solution (due to density differences between its compound InSb and GaSB) can cause convection currents that prevent achieving a steady state and can disturb the growth interface. This leads to non-uniformities, compositional variations, and defects within the crystal structure [27]. These convective flows and buoyancy effects can significantly impact the quality of the resulting crystal.
Moreover, The growth of InGaSb crystals involves the controlled diffusion and transport of Indium, Gallium, and Antimony species. Under normal gravity, diffusion rates and mass transport can be affected by buoyancy-driven flows and natural convection. These flow effects can alter

the concentration gradients, resulting in non-uniform composition and impurity incorporation in the crystal. When InGaSb crystal grows, the solidification front tends to have an irregular shape due to the effects of buoyancy-driven convection. This can lead to crystal defects such as dislocations, grain boundaries, and stacking faults, compromising the overall crystal quality. Natural convection can also exacerbate segregation effects, leading to non-uniform distribution of Indium and Gallium atoms within the crystal lattice. This can affect the optical and electronic properties of the crystal.

Segregation

The segregation effect in InGaSb refers to the preferential concentration of Indium or Gallium atoms in certain regions of the crystal during its growth. It occurs due to the differences in atomic sizes and chemical affinities between the constituent elements, leading to compositional variations and non-uniformity in the crystal structure [28, 29].
During crystal growth, the atoms in the melt diffuse and incorporate into the crystal lattice. However, the diffusion rates of Indium and Gallium atoms differ due to their distinct atomic sizes. Indium atoms, being larger in size, have slower diffusion rates compared to Gallium atoms. As a result, when Indium and Gallium are present in the melt, there can be a tendency for Indium atoms to accumulate or segregate in certain regions of the crystal.
The primary factors influencing the likelihood of segregation occurring are the growth conditions (higher temperature and faster growth rates enhance diffusion and reduce segregation, and non-uniform temperature profile and uncontrolled temperature gradient can exacerbate the segregation effect [30]), composition, and degree of supersaturation [31, 32, 33, 34]. In addition, if we look at the binary phase diagram of InSb and GaSb, which gives the relationship between concentration and temperature as shown in **Fig. 1.2**, we can see observe a large separation between the liquidus and solidus lines. This indicates that the concentrations of liquid and solid phases of InGaSb at a given temperature are quite different. Hence segregations occur during the solidification process of InGaSb crystal.
Segregation in InGaSb can have important implications for device performance and material properties. Non-uniform Indium or Gallium distribution can result in variations in the bandgap and composition, affecting the optical and electronic properties of the material. Segregation can introduce compositional fluctuations, dislocations, and defects, which can impact the crystal quality and device characteristics.
Understanding and managing the segregation effect in InGaSb is crucial for producing high-quality crystals with desired compositional and structural properties. By optimizing growth conditions and employing suitable techniques (for example, a Vertical Gradient Freezing with a three-zone furnace system [35]), we can minimize segregation and enhance the performance of InGaSb-based devices, such as infrared detectors, lasers, and thermophotovoltaic cells.

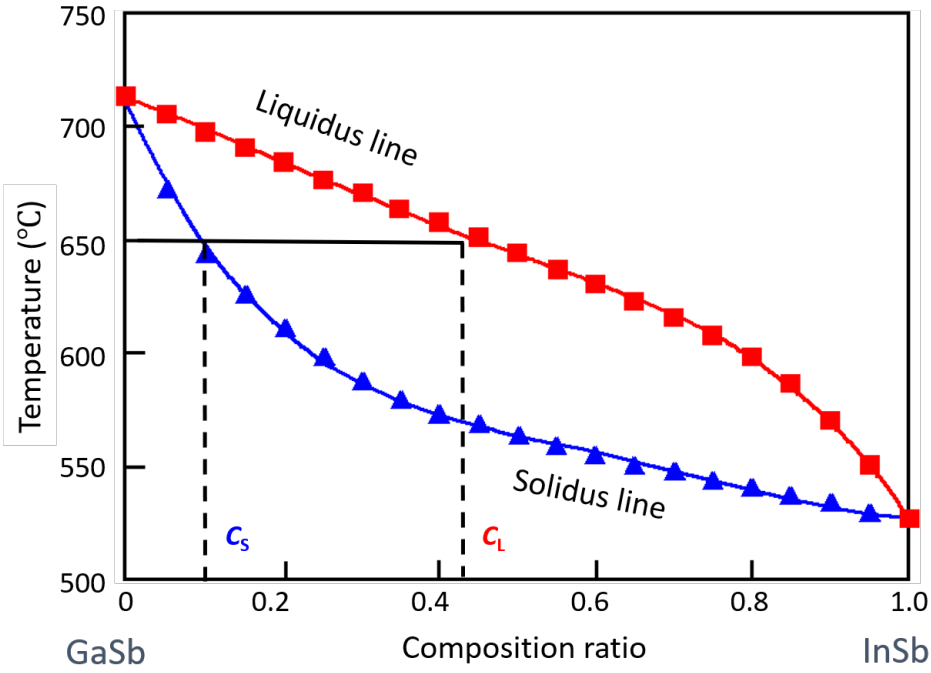

Figure 1.2. GaSb-InSb binary phase diagram [36].

Supercooling effect

The supercooling problem in InGaSb crystal growth refers to the phenomenon where the melt temperature is significantly higher than the actual solidification temperature, leading to delayed or inhibited nucleation and crystal growth. Supercooling can result in the formation of non-uniform structures, defects, and reduced crystal quality.
This effect occurs due to the presence of impurities, foreign particles, or defects that act as nucleation barriers, preventing the formation of solid crystals even when the temperature is below the melting point as illustrated in **Fig. 1.3**. This delay in nucleation allows the melt to cool further before solidification occurs, resulting in a larger temperature difference between the melt and the solid phase. The supercooling problem in InGaSb crystal growth can have several detrimental effects:

- Increased defect formation: Supercooling can lead to the formation of structural defects such as dislocations, stacking faults, and grain boundaries. The delayed nucleation and subsequent rapid growth can result in non-uniform crystal structures with higher defect densities.

- Non-Uniform composition: Supercooling can cause variations in the composition of the grown crystal. The delayed nucleation and prolonged growth in the supercooled melt can

lead to segregation effects, resulting in non-uniform distribution of Indium and Gallium atoms within the crystal lattice.

- Reduced crystal quality: Supercooling can lead to the formation of regions with different crystal orientations or polytypes, affecting the overall crystal quality. The presence of defects and non-uniform composition can further degrade the structural and optical properties of the crystal.

InGaSb exhibits a segregation coefficient below 1. During the crystal growth process, surplus solute molecules are expelled from the growth interface, leading to a change in solute concentration near the interface. This increase in solute concentration causes a reduction in temperature, enabling spontaneous nucleation to occur. Consequently, constitutional supercooling arises, resulting in interface breakdown.
Ozawa et al. [37] conducted a numerical analysis to investigate the impact of gravity level and cooling rate on the shape of the growth interface and supercooling in InGaSb. They employed a GaSb/InGaSb/GaSb sandwich system model for their calculations. The study revealed that the degree of constitutional supercooling decreased with decreased gravity levels and cooling rates because the influence of solutal convection was weaker. Therefore, in order to prevent constitutional supercooling and interface breakdown, a slow cooling rate was deemed necessary for the directional solidification of InGaSb.

Microcracks formation

The formation of microcracks in InGaSb crystals can be a significant problem during crystal growth and post-growth processes. Microcracks are small, localized fractures or discontinuities in the crystal structure, often invisible to the naked eye. These cracks can degrade the mechanical integrity, electrical performance, and overall quality of InGaSb crystals. Several factors contribute to the formation of microcracks in InGaSb crystals [38, 39, 40, 41]:

- Thermal stress: InGaSb crystals experience thermal stress during the crystal growth process, especially during cooling. As the crystal cools, thermal contraction can induce stress, leading to the development of microcracks. The magnitude of thermal stress depends on the coefficient of thermal expansion (CTE) mismatch between the crystal and the substrate or environment.

- Mismatched Lattice Parameters: InGaSb crystals are often grown on substrates with slightly different lattice parameters. The lattice parameter mismatch between the crystal and the substrate can result in strain accumulation during growth, leading to the formation of microcracks.

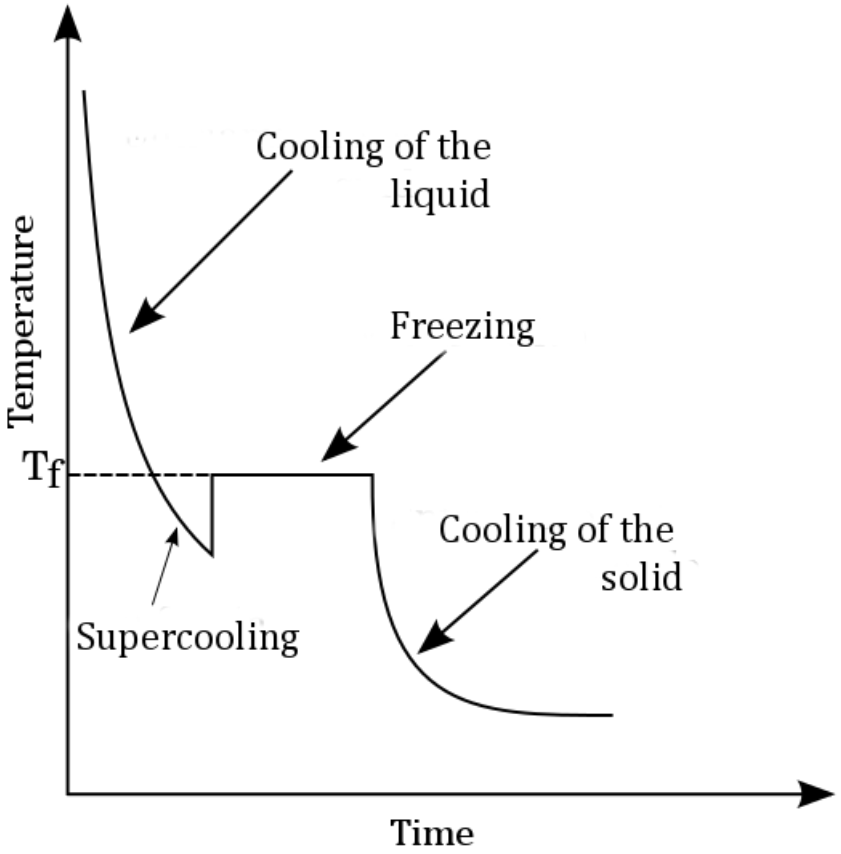

Figure 1.3. Plot of temperature vs. time of a substance showing supercooling.

- Growth conditions: Inadequate control of growth parameters such as temperature, growth rate, and composition can promote the formation of microcracks. Rapid cooling or abrupt changes in growth conditions can induce thermal gradients and stress, contributing to crack formation.

- Post-Growth processes: Microcracks can also form during post-growth processes, such as wafer sawing, polishing, or device fabrication. Mechanical stresses during these processes can propagate or initiate cracks in the crystal lattice.

The presence of microcracks in InGaSb crystals can have several negative consequences:

- Reduced mechanical strength: Microcracks weaken the mechanical strength of the crystal, making it more prone to breakage or failure during handling or device fabrication.

- Increased surface roughness: Microcracks on the crystal surface can cause roughness, which can affect the optical properties and the quality of subsequent thin film deposition or device integration processes.

- Electrical performance degradation: Microcracks can disrupt the electrical continuity of

the crystal, leading to increased resistance, reduced carrier mobility, and compromised device performance.

1.1.4 InGaSb alloy growth under microgravity

Achieving precise control over the composition and homogeneity of InGaSb crystals is crucial for their desired properties and device applications. However, under normal gravity, it can be challenging to maintain a uniform composition throughout the crystal growth process. Buoyancy-driven convection can cause compositional segregation and variations, leading to non-uniform alloy compositions.
To mitigate these issues, various techniques and strategies can be employed, such as the use of rotation, stirring, magnetic fields, or modified growth configurations to minimize convection and buoyancy effects [22, 42, 43, 44, **?**, 45, 46]. Overall, better control over crystal growth parameters helps reduce the impact of gravity-related issues.
Furthermore, some of these issues can be addressed by conducting crystal growth experiments under microgravity conditions, such as in space-based environments (The International Space Station for instance) or utilizing ground-based facilities that simulate microgravity. These approaches allow for improved control over the growth process and can lead to higher quality InGaSb crystals with enhanced properties suitable for various applications, including infrared detectors, lasers, and optoelectronic devices.
The growth of InGaSb crystals under reduced gravity fields has attracted significant interest due to the potential advantages it offers over growth under normal gravity. Under such conditions, the growth process is free from the buoyancy-driven convection and sedimentation effects that typically occur in Earth's gravity, leading to unique crystal growth characteristics. The growth of InGaSb crystals under microgravity can offer several benefits [47, 48, 49]:

- Reduced convection: In microgravity, the convective fluid motion caused by density differences is minimized or eliminated. This absence of convection allows for a more controlled and uniform distribution of temperature, concentration, and dopant species throughout the crystal. As a result, crystal growth can proceed in a more stable and uniform manner, leading to improved crystal quality.

- Uniform doping: InGaSb crystals often require precise doping control for specific device applications. Under microgravity conditions, dopant species are evenly distributed without the influence of convection, enabling more accurate and uniform doping profiles. This can enhance the performance and reproducibility of electronic and optoelectronic devices based on InGaSb crystals.

- Reduced defects: The absence of convection-induced stresses and concentration gradients in the melt under microgravity conditions can lead to a reduction in crystal defects, such

as dislocations, stacking faults, and grain boundaries. The improved crystal quality can result in enhanced optical and electrical properties, making the crystals more suitable for high-performance applications.

- Enhanced crystal morphology: Crystal growth under microgravity can promote the formation of smooth and faceted crystal surfaces. Without the influence of gravity-induced fluid flow, crystal growth occurs without disturbances and irregularities, resulting in well-defined crystal facets and reduced surface roughness. This can be beneficial for applications where precise control over crystal morphology is important.

However, it's important to note that the growth of InGaSb crystals under microgravity also poses some challenges:

- Limited access: Conducting crystal growth experiments in microgravity environments is logistically challenging and often limited to space missions or specialized facilities. Access to microgravity environments may be restricted, making it difficult to perform experiments on a regular basis.

- Technical constraints: Conducting crystal growth experiments in microgravity requires specialized equipment and modifications to accommodate the unique conditions. The design and operation of growth apparatus need to account for factors such as containment of the melt, heat transfer mechanisms, and sample handling.

- Time constraints: Experiments conducted under microgravity conditions have limited durations due to the finite time available during space missions or parabolic flights. This can restrict the growth time and size of the crystals that can be obtained.

The study of InGaSb crystal growth under microgravity conditions is an active area of research, and experiments are often conducted in collaboration with space agencies and research institutions. By exploring crystal growth under microgravity, researchers aim to improve the understanding of fundamental crystal growth mechanisms and enhance the quality and performance of InGaSb crystals for various technological applications.

1.1.5 Vertical Gradient Freeze technique

Vertical Gradient Freezing (VGF) is a melt growth technique used to produce high-quality compound (multi-component) single crystal semiconductors such as InGaAs, CdZnTe and others. This method involves controlled solidification of a melt while maintaining a temperature gradient along the growth axis of the crystal. The crucible containing the growth melt is preferentially cooled from one end by the application of a proper temperature profile that is moved electronically. There is no mechanically moving parts in VGF method and the growth could be achieved

without (or with) a seed. Simplicity of the system is the main advantage of VGF method in controlling growth parameters to realize the growth of high-quality single crystals, and also allows the use of easy-to-implement procedures and automation [50, 51]. The resulting single crystals can be used in a range of applications, including electronic devices, optoelectronics, and high-power devices that require precise crystal quality and control.

The basic principle of VGF method involves melting the desired material in a crucible at the top of a vertical growth furnace. The temperature of the melt is carefully controlled to create a stable thermal gradient. The lower part of the furnace is cooler, and as the material melts, it gradually solidifies while being pulled downwards through the temperature gradient [52]. Dopant materials can be introduced into the melt during the growth process if the desired crystal requires intentional doping with impurities to modify its electrical or optical properties. Once the crystal has been grown to the desired length, the temperature of the growth environment is gradually reduced, allowing the crystal to cool and anneal, thereby reducing strain and defects.

The vertical temperature gradient in VGF method helps to control the growth rate and maintain uniform crystal quality. The temperature gradient prevents the incorporation of impurities and defects, allowing for the production of high-purity and high-quality single crystals. Additionally, careful control of growth parameters enable the formation of large and single crystals suitable for various applications.

Besides the adequately designed heat flow, the thermal stability of the crystal growth system is the most critical factor for successful single crystal growth. Temperature fluctuations and thermal drift of the growth furnace can cause uncontrolled changes in the shape of the growth interface and induce spurious nucleation. In a classical Bridgman growth for example, where the charge and the furnace move relative to each other, it is difficult to achieve adequate long-term stability of the growth interface, as the radiative heat transport continuously changes at the ends of the growth crucible with the progress of the translation (**Fig. 1.4(a)**). Such effects can be eliminated. and the heat-transport control stabilized, in the gradient freeze technique where the growth crucible and the heater are stationary and the translation of the temperature gradient is achieved by programmed lowering of the temperature set-points in a multi-zone furnace (**Fig. 1.4(b)**. The disadvantage of the gradient freeze technique is the continuous change of the temperature gradient at the melt-solid interface as the solidification progresses. As a result, both the crystallization rate and the convection in the melt changes during crystal growth and need to be taken into consideration to obtain larger single crystals

1.1.6 InGaSb solid-liquid interface shape

The shape of the crystal/solution interface plays a crucial role in the growth of InGaSb crystals and significantly impacts their quality, properties, and performance in various applications. The interface shape refers to the morphology and characteristics of the boundary between the

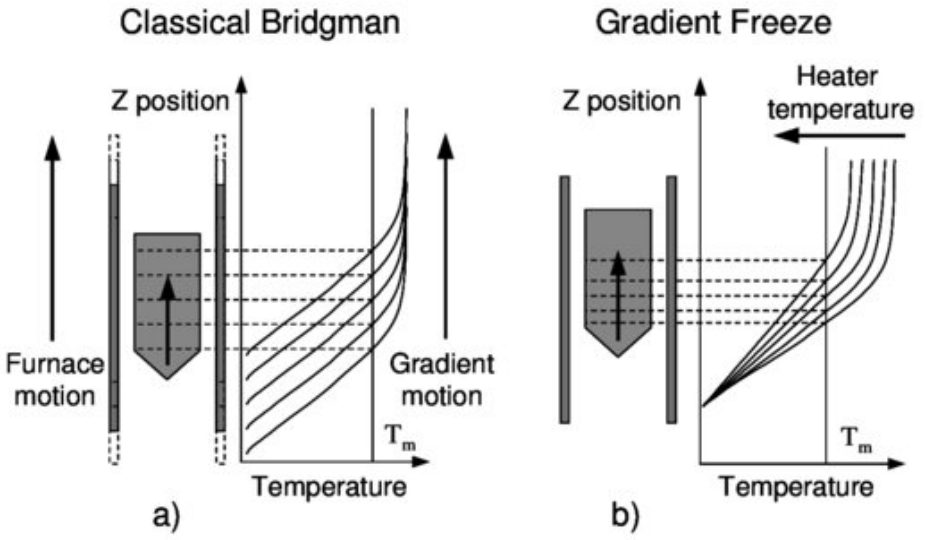

Figure 1.4. Comparison of the classical vertical Bridgman (a) and the gradient freeze crystal growth technique (b). T_m is the melting point and the horizontal dashed lines show the progress of the solid-liquid interface [53].

growing crystal and the surrounding environment or substrate. The control and optimization of the growth interface shape are essential for achieving high-quality InGaSb crystals with desired properties. The importance of growth interface shape in InGaSb crystals can be understood through the following points [54]:

- Crystal quality: The growth interface shape influences the crystal's structural perfection and defects. A smooth and flat growth interface is desirable as it minimizes lattice imperfections such as dislocations, stacking faults, and twins. By maintaining a uniform and well-defined interface shape, crystal quality can be enhanced, leading to improved electrical, optical, and mechanical properties.

- Epitaxial growth: InGaSb crystals are often grown epitaxially, where the crystal lattice of the growing layer aligns with that of the underlying substrate. The growth interface shape determines the degree of epitaxial alignment and the lattice matching between the crystal and the substrate. A well-matched and uniform interface shape promotes epitaxial growth, enabling the deposition of high-quality, strain-free layers with controlled composition and thickness.

- Surface roughness: The growth interface shape directly influences the surface roughness of the crystal. A smooth and uniform growth interface results in a low surface roughness, which is desirable for applications requiring precise control of surface quality, such as optoelectronic devices and integrated circuits. Reduced surface roughness also facilitates subsequent processing steps, such as thin film deposition and device fabrication.

- Interface dopant incorporation: Dopant incorporation at the growth interface plays a critical role in controlling the electrical properties of InGaSb crystals. The shape and characteristics of the growth interface can impact the diffusion and distribution of dopant species, affecting the doping profiles and carrier concentrations within the crystal. Precise control of the growth interface shape allows for tailored doping profiles, enabling the fabrication of specific device structures and functionalities.

- Interface stability: The growth interface shape influences the stability of the crystal growth process. A well-defined interface shape promotes stable growth conditions and minimizes the occurrence of growth instabilities, such as morphological defects, irregular growth fronts, or undesired surface features. A stable growth interface allows for controlled and reproducible crystal growth, leading to consistent material properties and device performance.

Growth interface shape comparison under 1G and μG

InGaSb alloy crystal was grown under the 'Alloy Semiconductor' crystal growth project on the Japanese Experiment Module (KIBO) on the ISS by VGF method using a GaSb (111)A/Te-doped InSb/GaSb (111)A sandwich sample [55]. A similar experiment was conducted under 1G on Earth and the dissolution and growth processes of μG and 1G samples were comparatively analyzed. **Figure 1.5** shows the Electron Probe Micro Analysis (EPMA) mapping of Indium distribution in the μG and 1G samples. The magnified images of indium mapping at seed and feed interfaces of both samples illustrate the variations of the interface shape at the initial and final stages of growth under μG (left) and 1G (right). From the mapping, it is clear that the shape of the growth interface of the μG sample remained almost the same from the initial to the final stage of growth. However, the growth interface of the 1G sample was nearly flat at the initial stage and highly concave toward the feed at the final stage of growth. Moreover, a V-shaped feed interface was observed in both samples beyond the residual solution region.
The understanding and control of growth interface shape are crucial for achieving high-quality InGaSb crystals with tailored properties for specific applications, including infrared detectors, high-speed electronic devices, and optoelectronic devices. Overall, the growth interface shape in InGaSb crystals plays a significant role in determining crystal quality, surface properties, and device performance. Controlling and optimizing the growth interface shape allows then the production of high-performance InGaSb crystals with enhanced functionality and improved integration capabilities.

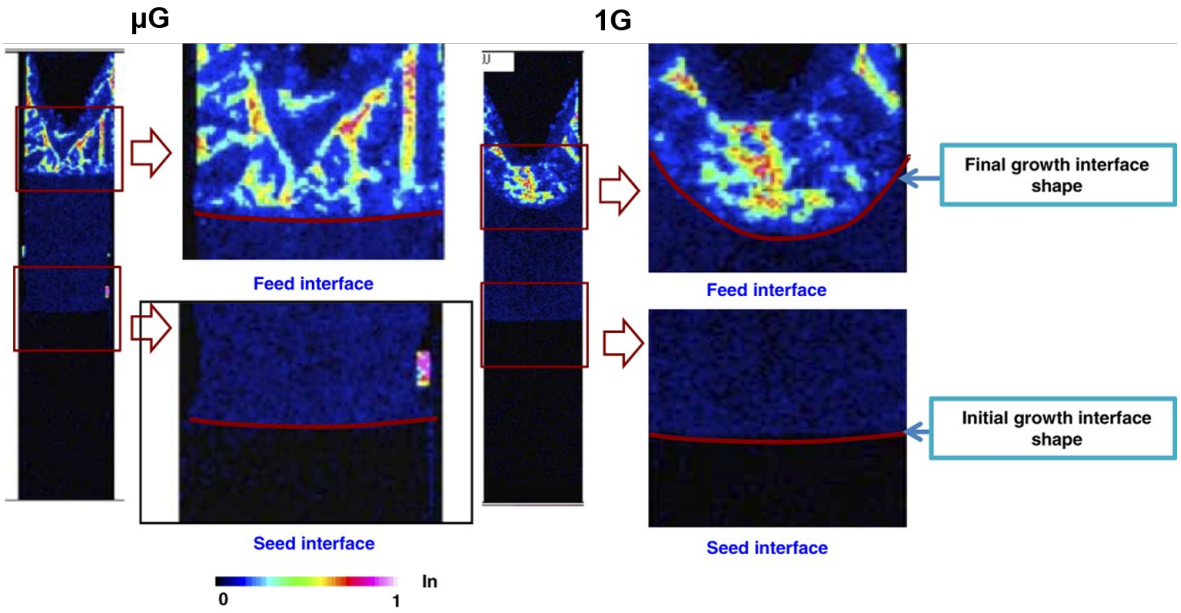

Figure 1.5. EPMA mapping of Indium distribution in μG and 1G experiments for the growth of InGaSb, and corresponding seed/feed interfaces in the initial and final stages of growth [55].

1.2 Objectives of the research work

The research objectives can be summarized as follows:

1. Explain the disparities between experimental results from the International Space Station (ISS) and numerical results regarding feed/seed dissolution lengths and crystal growth rates for different GaSb orientations (111A, 111B, 110).

2. Determine and utilize accurate physical properties, specifically the diffusion coefficient of GaSb in InSb melt, which is crucial for precise numerical calculations in a diffusion-dominant environment such as the ISS.

3. Conduct a numerical analysis of the InGaSb alloy crystal growth process via Vertical Gradient Freeze (VGF) method under microgravity conditions, surpassing the limitations of costly and scarce space experiments. Additionally, gain insights into the transport phenomena, kinetics and growth mechanism of InGaSb crystals in the VGF method.

4. Identify optimization possibilities and investigate the growth conditions necessary to achieve a flatter solid-liquid interface in InGaSb crystals under microgravity. This includes studying the effects of crucible rotation and temperature gradient on the growth interface shape, solute distribution, and growth rates.

5. Analyze the influence of natural convection on the melt flow and its impacts on the growth interface shape and homogeneity of InGaSb solution and growth rates.

6. Study the effects of external forces (e.g., magnetic fields), crucible rotation and temperature gradient on the melt flow. By controlling the melt flow, it is possible to achieve a flatter growth interface shape, improved compositional uniformity, and increased growth rate, while maintaining crystal quality.

7. Address the computational cost, accelerate the optimization process and efficiently determine the desired control parameters and optimal growth conditions by utilizing Bayesian optimization and machine learning techniques.

Ultimately, this research aims to enhance the understanding and control of the InGaSb crystal growth process and serve as a preparation for future growth experiments on the ground, paving the way for future advancements in electronic, optoelectronic, and energy conversion device technologies.

1.3 Thesis outline

This dissertation is structured as follows:

Chapter 1 provides a general introduction and background on III-V semiconductors, with a focus on InGaSb. It discusses the importance of InGaSb, the challenges associated with its growth and reviews related experimental and numerical studies. The research objectives are also introduced in this chapter.
Chapter 2 describes the numerical simulation model used to investigate the growth process of InGaSb crystals, i.e., the volume-averaging continuum technique. It covers the governing equations and computation procedure and also highlights the relevance of machine learning usage in crystal growth research.
In Chapter 3 we establish a relationship between the diffusion coefficient of GaSb in InSb melt and its concentration by using the International Space Station (ISS) microgravity experimental results, as well as Bayesian optimization. Under a diffusion-controlled environment, the growth rate and crystal quality of InGaSb alloy semiconductors are influenced by the diffusion coefficient values, and an exponential variation of the diffusion coefficient according to the concentration is deduced and considered for future optimization studies.
Chapter 4 focuses on a numerical simulation study that aims to control the growth interface shape of InGaSb crystals in the Vertical Gradient Freezing (VGF) method under microgravity conditions, which directly affects the quality and homogeneity of the grown crystals. An adaptive control recipe, combining Bayesian optimization and reinforcement learning, is introduced to maintain a flatter growth interface and a high growth rate through crucible rotation and optimized thermal boundary conditions.
Chapter 5 presents numerical simulations of InGaSb crystal growth under normal gravity conditions and discusses the impact of natural convection on solute transport and crystal growth. The chapter focuses on improving the growth rate while controlling the growth interface shape of InGaSb crystals, even on earth's gravity level, by searching for optimum growth conditions utilizing Bayesian optimization. The findings offer promising insights for future ground-based experiments aimed at growing high-quality InGaSb crystals for various electronic, optoelectronic, and energy conversion applications.
Chapter 6 summarizes the conclusions drawn from the research and outlines future perspectives.

Chapter 2

Numerical model and optimization scheme

2.1 Numerical simulation in the crystal growth field

Numerical simulations play a crucial role in the study and understanding of crystal growth processes. They provide a powerful tool for predicting and analyzing various aspects of crystal growth, including the growth dynamics, temperature distribution, fluid flow, and crystal morphology. By simulating the growth process using mathematical models and computational algorithms, researchers can gain insights into the underlying physics, optimize growth conditions, and guide experimental efforts. Some key aspects and benefits of numerical simulations in the crystal growth field are:

- Growth process modeling: Numerical simulations allow researchers to construct mathematical models that capture the fundamental physics and phenomena involved in crystal growth. These models can incorporate various parameters, such as temperature gradients, fluid flow, species diffusion, and crystal growth kinetics. By solving the governing equations numerically, simulations provide a detailed understanding of the growth process and enable the exploration of different growth scenarios and conditions [56].

- Prediction of growth conditions: Simulations help in predicting the optimal growth conditions for achieving desired crystal properties. By varying the input parameters and analyzing the simulation results, researchers can identify the optimal temperature profiles, growth rates, and other process parameters that lead to the desired crystal quality, morphology, and defect distribution. This predictive capability allows for the efficient design and optimization of crystal growth experiments.

- Visualization of growth dynamics: Numerical simulations provide a visual representation of the growth dynamics, allowing researchers to observe and analyze the growth process in detail, which is not always easy to achieve in actual experiments. Simulations can generate visual outputs, such as temperature distributions, concentration profiles, and

crystal morphologies, which provide valuable insights into the evolving interface shapes, nucleation, and crystal growth mechanisms. This visualization aids in understanding the complex dynamics of crystal growth.

- Investigation of growth challenges: Crystal growth can be affected by various challenges, such as heat transfer limitations, fluid flow instabilities, and impurity segregation. Numerical simulations enable researchers to study and analyze these challenges by quantifying their effects on the growth process. Simulations can provide insights into the causes of issues, guide the development of mitigation strategies, and optimize growth conditions to overcome these challenges.

- Design of growth methods and equipment: Numerical simulations contribute to the design and optimization of growth methods and equipment. They can be used to model and analyze different growth techniques, such as Bridgman-Stockbarger, Vertical Gradient Freezing, Czochralski, or vapor phase epitaxy, to optimize their parameters and guide the design of growth furnaces, crucibles, and other equipment. Simulations aid in the development of innovative growth methods and the improvement of existing techniques.

- Reduction of experimental efforts: Numerical simulations complement experimental studies by providing a cost-effective and time-efficient means of exploring and analyzing various growth scenarios. Simulations help in reducing the number of experimental iterations required to achieve desired results by providing insights into the growth process and guiding experimental efforts toward optimal conditions. This reduces the cost and time associated with experimental trial and error.

It's important to note that the accuracy of numerical simulations relies on the quality of the mathematical models, input parameters, and computational algorithms used. Validation of simulation results through comparison with experimental data is crucial to ensure their reliability. In summary, numerical simulations in crystal growth provide a valuable tool for understanding, predicting, and optimizing growth processes. They enable researchers to explore growth dynamics, predict growth conditions, investigate challenges, and guide the design of growth methods and equipment. Through numerical simulations, researchers can gain valuable insights that aid in the development of high-quality crystals with tailored properties for a wide range of applications.

2.2 InGaSb growth process: Model formulation

A new volume-averaging continuum method developed by Yamamoto *et al.* [57] is used to simulate the dissolution and growth process of InGaSb crystal growth. During the dissolution and growth processes, the system of GaSb/InSb/GaSb is considered a binary mixture. Based

on the volume-averaging continuum models [58, 59, 60], the mathematical description of this problem consists of a macroscopic model that includes the conservation of continuity, energy, and species to find the mixture variables, shown in the equations below:

$$\frac{\partial \rho}{\partial t} + \nabla \cdot (\rho \boldsymbol{u}) = 0 \tag{2.1}$$

$$\frac{\partial (\rho \boldsymbol{u})}{\partial t} + \nabla \cdot (\rho \boldsymbol{u}\boldsymbol{u}) = -\nabla p + \nabla \cdot (\mu_{\mathrm{l}} \nabla \boldsymbol{u}) + D^{\boldsymbol{u}} + F^{\boldsymbol{u}} + \boldsymbol{B} + \boldsymbol{M} \tag{2.2}$$

$$\frac{\partial (\rho h)}{\partial t} + \nabla \cdot (\rho h \boldsymbol{u}) = \nabla \cdot (\frac{\lambda}{c} \nabla h) + D^{h} + F^{h} \tag{2.3}$$

$$\frac{\partial (\rho C)}{\partial t} + \nabla \cdot (\rho C \boldsymbol{u}) = \nabla \cdot (\rho D \nabla C) + D^{C} + F^{C} \tag{2.4}$$

where $\boldsymbol{u}$ is flow velocity, ρ mixture density, p pressure, μ mixture viscosity, λ thermal conductivity, h enthalpy $\boldsymbol{g}$ gravitational acceleration, c heat capacity, T temperature, C solute concentration, D diffusion coefficient and t is the time. In Eq. (2.2), the momentum source term $\boldsymbol{B}$ stands for body forces, such as gravity in terms of Boussinesq approximation and the momentum source term $\boldsymbol{M}$ stands for interfacial drag force, such as damping in porous mushy structure in terms of Kozeny-Carman equation [61]. The energy and species source terms in Eqs (2.3-4) are diffusion-like and convection-like mixture sources [62] derived as:

$$D^{h} = -\nabla \cdot (\frac{\lambda}{c} \nabla h) + \nabla \cdot (\lambda \nabla T) \tag{2.5}$$

$$F^{h} = \nabla \cdot (\rho h \boldsymbol{u}) - \sum_{\mathrm{j=l,s}} \nabla \cdot (\varepsilon_{\mathrm{j}} \rho_{\mathrm{j}} \boldsymbol{u}_{\mathrm{j}} h_{\mathrm{j}}) \tag{2.6}$$

$$D^{c} = -\nabla \cdot (\rho D \nabla C) + \sum_{\mathrm{j=l,s}} \nabla \cdot (\varepsilon_{\mathrm{j}} \rho_{\mathrm{j}} D_{\mathrm{j}} \nabla C_{\mathrm{j}}) \tag{2.7}$$

$$F^{c} = \nabla \cdot (\rho \boldsymbol{u} C) - \sum_{\mathrm{j=l,s}} \nabla \cdot (\varepsilon_{\mathrm{j}} \rho_{\mathrm{j}} \boldsymbol{u}_{\mathrm{j}} C_{\mathrm{j}}) \tag{2.8}$$

The mixture properties and variables are defined as follows:

$$\rho = \varepsilon_{\mathrm{l}}\rho_{\mathrm{l}} + \varepsilon_{\mathrm{s}}\rho_{\mathrm{s}} \qquad \lambda = \varepsilon_{\mathrm{l}}\lambda_{\mathrm{l}} + \varepsilon_{\mathrm{s}}\lambda_{\mathrm{s}} \qquad c = f_{\mathrm{l}}c_{\mathrm{l}} + f_{\mathrm{s}}c_{\mathrm{s}} \qquad D = f_{\mathrm{l}}D_{\mathrm{l}} + f_{\mathrm{s}}D_{\mathrm{s}} \tag{2.9}$$
$$h = f_{\mathrm{l}}h_{\mathrm{l}} + f_{\mathrm{s}}h_{\mathrm{s}} \qquad \boldsymbol{u} = f_{\mathrm{l}}\boldsymbol{u}_{\mathrm{l}} + f_{\mathrm{s}}\boldsymbol{u}_{\mathrm{s}} \qquad C = f_{\mathrm{l}}C_{\mathrm{l}} + f_{\mathrm{s}}C_{\mathrm{s}}$$

The volume fraction of solid and liquid (ε_{s}, ε_{l}) are related to the mass fraction of solid and liquid (f_{s}, f_{l}) via:

$$f_{\mathrm{s}} = \frac{\rho_{\mathrm{s}}\varepsilon_{\mathrm{s}}}{\rho} \qquad f_{\mathrm{l}} = \frac{\rho_{\mathrm{l}}\varepsilon_{\mathrm{l}}}{\rho} \tag{2.10}$$

The total of the mass and volume fractions must be unity. Enthalpy and temperature are related by specific heat. Thus, the general expressions for the phase enthalpies are:

$$h_{\mathrm{l}} = \int_0^T c_{\mathrm{l}} \mathrm{d}T + h_{\mathrm{l}}^0 \qquad h_{\mathrm{s}} = \int_0^T c_{\mathrm{s}} \mathrm{d}T + h_{\mathrm{s}}^0 \tag{2.11}$$

In the above equations, h_s^0 can be set to zero, and h_s^0 set to L, the latent heat of the phase change. Further, using average specific heat one obtains:

$$h_l = c_l T + f_l L \qquad h_s = c_s T \tag{2.12}$$

Substituting Eqs. (2.12) into Eq. (2.9), we can get the following equation:

$$h = cT + f_l L \tag{2.13}$$

β_T thermal expansion coefficient, β_C solutal expansion coefficient, α thermal diffusivity, $\boldsymbol{F}_r$ centrifugal force term, $\boldsymbol{J}$ induced electric current density, $\boldsymbol{B}$ magnetic field,

Closure of the system of conservation equations requires additional relationships for phase mass fraction f and concentration C. With the assumption of local phase equilibrium, the concentrations of the solid and liquid phases (C_s, C_l) in the volume elements within the mushy zone, i.e. for $0 < \varepsilon < 1$, are related to the temperature (($T = T_l = T_s$) through the equilibrium phase diagram of a particular binary mixture.

For binary phase diagrams that do not exhibit eutectic, for example, the binary phase diagram of SiGe and pseudo-binary phase diagram of InGaSb, the solidus and liquidus curves can be simplified in a similar way as in the case of binary eutectic phase diagram by separating the phase diagram into two regions as illustrated in **Fig. 2.1**.

In the present study, we utilize the new volume-average continuum model developed by Yamamoto *et al.* [57]. This is a good choice for simulating the transport phenomena (momentum, mass and heat transport with phase changes) involved in the melts of binary and ternary growth systems. This technique can handle both microscopic and macroscopic considerations together in one system of equations. The solution procedure can be summarized as follows (see also [57, 63]): The governing equations (complemented with additional relationships in terms of phase mass or volume fractions, concentrations of the solid and liquid phases. . .) are first solved with the available mass fraction field of the liquid phase f_l. The newly estimated T and C values are then used to update the liquid mass fraction f_l field using the phase diagram of InGaSb. This pseudo-binary phase diagram does not exhibit eutectics; therefore, it is divided into two regions, each region having a set of equations used to update the liquid mass fraction f_l field. Also, at this stage, new values of liquid phase concentration C_l and solid phase concentration C_s are updated using the new f_l field. The iterative procedure continues until the solution converges. Once the solution has converged, the simulation moves to the next time step where the iterative cycle is followed once again. In summary, the motion of melting/dissolution and solidifying/growth interfaces can easily be traced by calculating the phase volume fractions (therefore identifying the liquid and solid phases in the domain) from the applied temperature and composition profiles, as well as the pseudo-binary phase diagram of InSb-GaSb. For clarity, we illustrate the different interfaces in Fig. 2.2. The interface positions are calculated from the contour of volume

fraction equal to 0.5 in this numerical domain. Further information regarding the numerical approach and code validation for comparable systems can be found in previous articles [57, 63, 64].

After the above considerations, the following governing equations are finally solved:

$$\nabla \cdot \boldsymbol{u} = 0 \tag{2.14}$$

$$\frac{1}{\varepsilon_\mathrm{l}}\frac{\partial \boldsymbol{u}}{\partial t} + \frac{1}{{\varepsilon_\mathrm{l}}^2}\boldsymbol{u}\cdot\nabla\boldsymbol{u} = -\frac{1}{\rho}\nabla p + \frac{1}{\rho\varepsilon_\mathrm{l}}\nabla\cdot(\mu_\mathrm{l}\nabla\boldsymbol{u}) + \frac{1}{\rho\varepsilon_\mathrm{l}}(\boldsymbol{B}+\boldsymbol{M}) \tag{2.15}$$

$$\begin{aligned}\frac{\partial(\rho c T)}{\partial t} + \nabla\cdot(\rho c \boldsymbol{u} T) = \nabla\cdot(\lambda\nabla T) - \rho_\mathrm{l}(c_\mathrm{s}-c_\mathrm{l})T_\mathrm{m}\frac{\partial\varepsilon_\mathrm{l}}{\partial t} - \\ - \rho_\mathrm{l}L\frac{\partial\varepsilon_\mathrm{l}}{\partial t} - \rho_\mathrm{l}(c_\mathrm{s}-c_\mathrm{l})T_\mathrm{m}\boldsymbol{u}\nabla\varepsilon_\mathrm{l} - \rho_\mathrm{l}L\boldsymbol{u}\nabla\varepsilon_\mathrm{l}\end{aligned} \tag{2.16}$$

$$\frac{\partial C}{\partial t} + \frac{\rho_\mathrm{l}}{\rho}\nabla\cdot(C_\mathrm{l}\boldsymbol{u}) = \nabla\cdot(\frac{\varepsilon_\mathrm{l}\rho_\mathrm{l}}{\rho}D_\mathrm{l}\nabla C_\mathrm{l}) \tag{2.17}$$

In computing these equations, the liquid, solid, and total enthalpies are defined as:

$$h_\mathrm{l} = \int_{T_\mathrm{m}}^{T} c_\mathrm{l}\mathrm{d}T + h_\mathrm{l}^{T_\mathrm{m}} = c_\mathrm{l}(T-T_\mathrm{m}) + L + c_\mathrm{s}T_\mathrm{m} \tag{2.18}$$

$$h_\mathrm{s} = \int_{0}^{T} c_\mathrm{s}\mathrm{d}T = c_\mathrm{s}T \tag{2.19}$$

$$h = cT + f_\mathrm{l}L + f_\mathrm{l}(c_\mathrm{s}-c_\mathrm{l})T_\mathrm{m} \tag{2.20}$$

The governing equations are solved together with the phase diagram. In the solid phases (solid feed/seed and the crucible wall), the energy equation is the only balance law which reduces to the heat conduction equation in the form:

$$\frac{\partial T}{\partial t} = \lambda_\mathrm{i}\nabla^2 T \tag{2.21}$$

where λ_i is the thermal conductivity of the solid phase. The coupling between the computational domains such as the grown crystal and the crucible wall is accomplished by outer iterations.

2.3 OpenFOAM

OpenFOAM (Open Field Operation and Manipulation) is an open-source computational fluid dynamics (CFD) software package. It provides a comprehensive set of tools and solvers for simulating fluid flow, heat transfer, and other related phenomena using numerical methods. OpenFOAM is widely used in academia, research, and industry for modeling and analyzing complex fluid flow problems. Key features and characteristics of OpenFOAM include [65, 66, 67]:

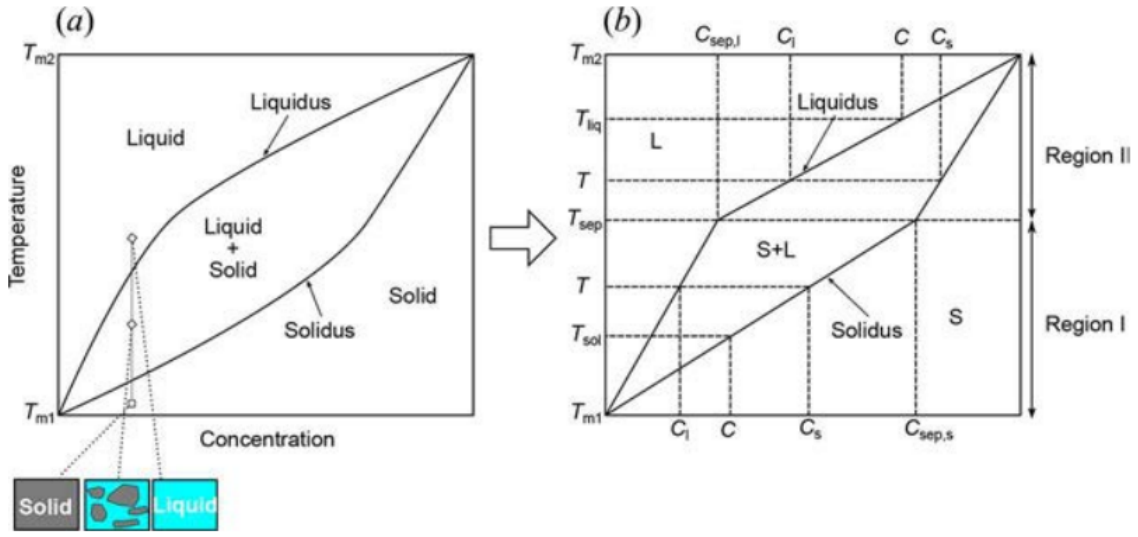

Figure 2.1. Phase diagram of a pseuo-binary system of GaSb–InSb. (a) Actual phase diagram and (b) linearized phase diagram used in the simulations.

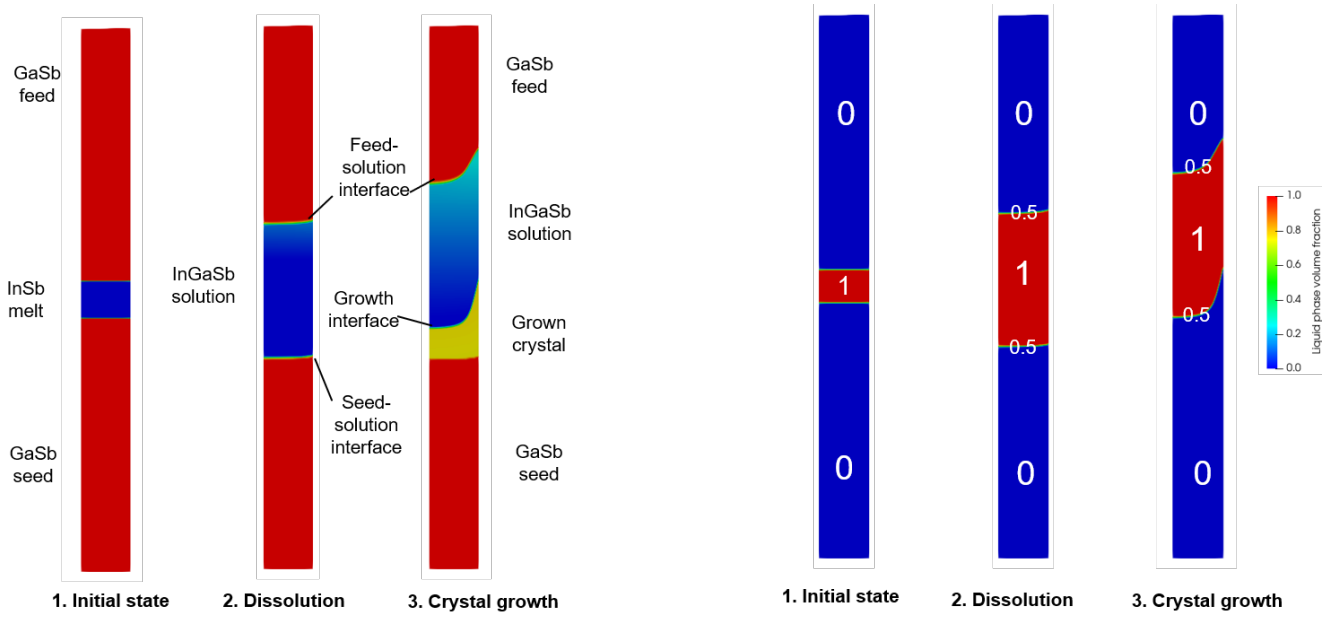

Figure 2.2. Simplified schematic diagram illustrating the stages of InGaSb crystals growth by VGF method and the S-L interfaces involved. Solute concentration distribution (left), liquid volumes fraction distribution (right).

- Open-Source nature: OpenFOAM is an open-source software, which means its source code is freely available to the public. This allows users to modify and customize the software according to their specific needs, fostering collaboration and innovation within the CFD community.

- Numerical methods: OpenFOAM employs finite volume methods to discretize and solve the governing equations of fluid flow. It offers a range of numerical schemes for spatial and temporal discretization, allowing users to choose the most appropriate scheme for their specific simulation requirements.

- Multiphysics capabilities: OpenFOAM supports the simulation of multiphysics problems, including fluid-structure interaction, conjugate heat transfer, combustion, and turbulence modeling. This enables the study of complex phenomena and their interactions in a single simulation framework.

- Pre-Processing and Post-Processing tools: OpenFOAM provides pre-processing tools for geometry creation, mesh generation, and boundary condition specification. It also offers post-processing utilities for visualizing and analyzing simulation results, including contour plots, vector plots, and data extraction.

- Solver libraries: OpenFOAM features a wide range of solver libraries that cover various flow regimes and physical models. These solvers include both steady-state and transient solvers for laminar and turbulent flows, compressible and incompressible flows, and single-phase and multiphase flows.

- Meshing flexibility: OpenFOAM supports both structured and unstructured mesh formats, allowing users to generate meshes that suit their specific simulation needs. It offers meshing utilities for creating meshes directly within OpenFOAM or importing meshes from external software.

- Extensibility: OpenFOAM's modular architecture enables the development of custom solvers, models, and utilities. Users can extend the software's capabilities by writing their own code or incorporating third-party extensions into their simulations.

- Validation and verification: OpenFOAM has an active community that conducts extensive validation and verification studies to ensure the accuracy and reliability of the software. This involves benchmarking simulations against analytical solutions, experimental data, and other well-established CFD codes.

OpenFOAM has been utilized in various industries, including automotive, aerospace, energy, and environmental engineering, to address complex fluid flow problems. Its open-source nature, coupled with its extensive capabilities and flexibility, makes it a valuable tool for researchers and engineers seeking to simulate and analyze fluid dynamics phenomena.

2.4 ParaView

ParaView is an open-source, multi-platform data analysis and visualization software widely used in scientific and engineering fields. Developed by Kitware Inc., ParaView provides a powerful set of tools for visualizing and analyzing large datasets generated by various simulation and data processing applications. Key features and characteristics of ParaView include [68, 69]:

- Data visualization: ParaView enables users to visualize and explore data in 2D and 3D formats. It supports a wide range of data types, including structured grids, unstructured meshes, point clouds, and volumetric data. Users can interactively manipulate and explore the data, apply various rendering techniques, and create visualizations such as isosurfaces, volume renderings, contours, and streamlines.

- Parallel processing: ParaView leverages parallel processing capabilities to handle large datasets efficiently. It can distribute computation and rendering tasks across multiple processors or machines, enabling users to work with massive datasets that would be otherwise impractical to handle on a single system.

- Extensibility: ParaView offers an extensive application programming interface (API) that allows users to extend its capabilities and customize the software. Users can develop plugins, scripts, and custom filters using Python or C++, enabling them to tailor ParaView to their specific needs and integrate it into their existing workflows.

- Data processing and analysis: ParaView provides a wide range of data processing and analysis features. Users can apply filters to manipulate and preprocess data, perform quantitative analysis, extract statistical information, compute derived quantities, and apply algorithms for tasks such as smoothing, interpolation, and data reduction.

- Integration with other tools: ParaView integrates well with other scientific computing and visualization tools. It can read and write data in various formats commonly used in scientific and engineering applications, including VTK, NetCDF, HDF5, and many others. It also supports interoperability with other software packages like MATLAB and Python scientific libraries.

ParaView is utilized in a wide range of fields, including computational fluid dynamics, climate modeling, geophysics, materials science, biomedical engineering, and many others. Its user-friendly interface, advanced visualization capabilities, and support for large-scale datasets make it a valuable tool for researchers, engineers, and scientists who need to visualize, analyze, and communicate complex data.

2.5 Machine learning in the crystal growth field

Machine learning is a subfield of artificial intelligence (AI) that focuses on developing algorithms and models capable of learning from data and making predictions or decisions without explicit programming. It aims to enable computers to automatically learn and improve from experience, similar to how humans learn from past observations and examples [70].
Machine learning algorithms rely on data as their input. This data can come in various forms, such as structured data (e.g., tables), unstructured data (e.g., text, images), or even sequential data (e.g., time series). The quality and quantity of data play a crucial role in training accurate and reliable machine learning models. Machine learning algorithms are designed to analyze and learn patterns from data. These algorithms can be broadly categorized into three main types [71]:

- Supervised Learning: In supervised learning, the algorithm learns from labeled examples, where the input data is associated with corresponding target outputs. The goal is to learn a mapping function that can predict the correct output for new, unseen inputs.

- Unsupervised Learning: Unsupervised learning involves learning patterns and structures from unlabeled data. The algorithm discovers inherent relationships, clusters, or representations within the data without any predefined target outputs.

- Reinforcement Learning: Reinforcement learning involves an agent interacting with an environment, learning from feedback in the form of rewards or punishments. The agent learns through trial and error to maximize its cumulative reward by taking actions in the environment.

Machine learning models are trained by feeding them with labeled or unlabeled data. During the training process, the model adjusts its internal parameters and learns the underlying patterns in the data [72]. The objective is to minimize a predefined loss or error function, optimizing the model's performance. To assess the performance of a machine learning model, it is essential to evaluate its predictions or decisions on new, unseen data. This involves splitting the available data into training and testing sets, or employing more advanced techniques such as cross-validation or holdout validation. Evaluation metrics, such as accuracy, precision, recall, or F1 score, help quantify the model's performance. Once a machine learning model is trained and validated, it can be deployed in real-world applications. The model takes new input data and produces predictions or decisions based on what it has learned. Inference can happen in real-time or batch processing, depending on the specific use case.
Machine learning has a wide range of applications across various industries, including healthcare, finance, transportation, manufacturing, and more. It is used for tasks such as image and speech recognition, natural language processing, recommendation systems, anomaly detection, fraud

detection, and predictive maintenance, among others. It is important to note that machine learning is an active area of research, and new algorithms, techniques, and advancements continue to emerge. As technology progresses, more sophisticated models and methods, such as deep learning and neural networks, have gained prominence in tackling complex problems and achieving state-of-the-art results [73, 74].

Applications in the crystal growth field

Machine learning techniques have found valuable applications in the field of crystal growth, aiding researchers in understanding and optimizing the growth processes [75]. Some ways in which machine learning is used in crystal growth are:

- Predictive modeling: Machine learning algorithms can be trained to predict the growth behavior and properties of crystals based on input parameters such as temperature, pressure, concentration, and growth conditions. By analyzing historical data and experimental results, these models can provide insights into the relationship between process parameters and crystal properties, helping researchers optimize growth conditions for desired crystal properties.

- Process optimization: Machine learning algorithms can optimize crystal growth processes by exploring large parameter spaces and identifying optimal growth conditions. By incorporating objective functions and constraints, these algorithms can search for the best combination of growth parameters to achieve specific crystal properties, such as size, shape, purity, and defect density. This approach can save time and resources by reducing trial-and-error experiments [76, 77].

- Crystal quality assessment: Machine learning techniques can be used to assess the quality and characteristics of grown crystals. By analyzing images or spectroscopic data obtained during crystal growth, algorithms can identify defects, impurities, and crystallographic orientations. This helps in determining the suitability of crystals for specific applications and provides insights for process improvement.

- Crystal structure prediction: Machine learning methods, such as neural networks and genetic algorithms, can be utilized to predict the crystal structures of materials based on their composition and bonding patterns. By training models on known crystal structures and their corresponding properties, these algorithms can generate predictions for new compositions, enabling researchers to explore novel materials with tailored properties [78, 79].

- Data analysis and visualization: Machine learning techniques can aid in the analysis and visualization of large datasets generated during crystal growth experiments. Clustering

algorithms can identify patterns and group similar crystals based on their properties, aiding in the classification and understanding of crystal growth behavior. Dimensionality reduction techniques can help visualize high-dimensional data, making it easier to interpret and analyze experimental results.

It is important to note that the success of machine learning in crystal growth heavily relies on the availability of high-quality and well-curated data [76]. Accurate and representative datasets are crucial for training robust models. Furthermore, domain expertise is essential for interpreting the results generated by machine learning algorithms and integrating them into the crystal growth process. The integration of machine learning techniques in crystal growth research has the potential to accelerate discoveries, optimize processes, and enable the design of advanced materials with desired properties. Ongoing research in this field continues to explore and refine the use of machine learning methods for crystal growth optimization and materials discovery [80, 81, 82, 83, 84].

2.6 Reinforcement learning

Reinforcement learning is a subfield of machine learning that focuses on training agents to make sequential decisions by learning from interactions with an environment. It draws inspiration from how humans and animals learn through trial and error, receiving feedback in the form of rewards or punishments [85, 86]. In reinforcement learning, an agent learns to navigate an environment and take actions to maximize cumulative rewards or achieve a specific objective. The agent interacts with the environment in discrete time steps, observing the current state, selecting an action, receiving a reward, and transitioning to a new state as summarized in **Fig. 2.3**. The goal is to find an optimal policy that maps states to actions, maximizing the expected cumulative reward over time [87, 88, 89]. Key components of reinforcement learning include:

1. Agent: The entity that learns and takes actions in the environment. It can be a software agent, a robot, or any entity capable of interacting with the environment.

2. Environment: The external system with which the agent interacts. It can be a simulated environment, a physical environment, or a combination of both.

3. State: The representation of the environment at a given time step. The state provides the necessary information for the agent to make decisions.

4. Action: The set of possible actions that the agent can take in a given state. Actions can have short-term consequences and influence the subsequent state.

5. Reward: The feedback signal that the agent receives after taking an action. It quantifies the desirability or quality of the agent's actions in a given state. The agent's goal is to maximize the cumulative reward over time.

6. Policy: The strategy or rule that the agent uses to select actions based on the observed states. The policy can be deterministic (selecting a single action) or stochastic (selecting actions based on a probability distribution).

7. Value Function: The value function estimates the expected cumulative reward or value of being in a certain state and following a particular policy. It helps the agent evaluate and compare different states or state-action pairs.

Reinforcement learning algorithms employ various techniques to learn optimal policies. These include:

- Value-Based Methods: These algorithms estimate the value function and use it to derive an optimal policy. Examples include Q-learning and Deep Q-Networks (DQN).

- Policy-Based Methods: These algorithms directly optimize the policy without explicitly estimating the value function. Examples include policy gradients and the REINFORCE algorithm.

- Model-Based Methods: These algorithms build a model of the environment and use it to simulate interactions and plan future actions. Model-based reinforcement learning combines model learning and decision-making.

Reinforcement learning has been successfully applied in various domains, including robotics, game playing, resource management, recommendation systems, and autonomous driving. Notable achievements include AlphaGo, which used reinforcement learning to defeat human champions in the game of Go, and DeepMind's AlphaStar, which reached grandmaster level in the game of StarCraft II. Reinforcement learning algorithms have the ability to learn complex and adaptive behaviors, but they sometimes require significant computational resources, extensive exploration, and careful tuning of hyperparameters.

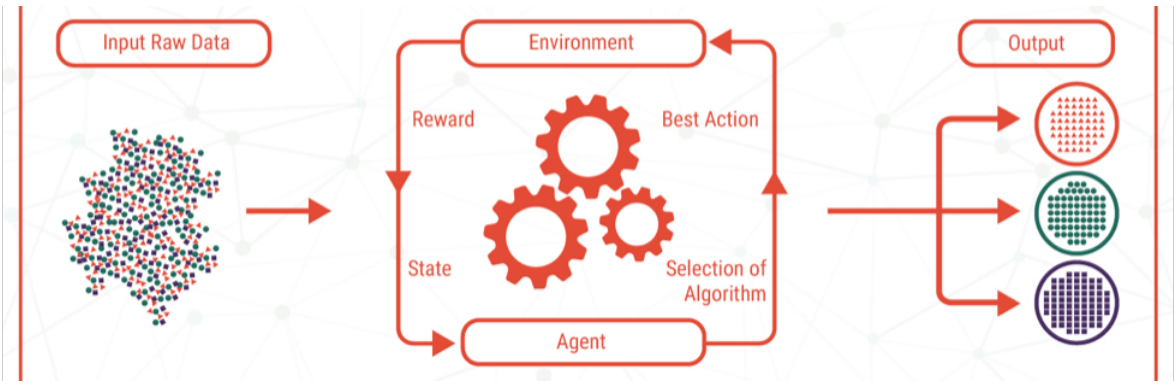

Figure 2.3. Reinforcement learning schematic [90].

2.7 Bayesian optimization

Bayesian optimization is a powerful technique for the optimization of black-box functions that are expensive to evaluate. It leverages the principles of Bayesian inference to efficiently search for the optimal solution while minimizing the number of function evaluations. In many real-world optimization problems, the objective function is unknown and costly to evaluate. Bayesian optimization tackles this challenge by building a probabilistic model, known as a surrogate or response surface, that approximates the unknown objective function. This surrogate model is continuously updated as new evaluations of the objective function are obtained [91, 92, 93]. The key idea behind Bayesian optimization is to balance exploration and exploitation. Exploration involves sampling points in the search space where the objective function is uncertain or poorly understood, while exploitation focuses on sampling points that are likely to yield high values of the objective function. This balance is achieved through an acquisition function, which guides the selection of the next point to evaluate based on the surrogate model and its uncertainty. The acquisition function trades off exploration and exploitation by considering both the predicted mean and uncertainty of the surrogate model. Popular acquisition functions include:

- Expected Improvement (EI): This function selects the point that has the highest expected improvement over the current best solution. It balances exploration by considering the uncertainty of the surrogate model.

- Upper Confidence Bound (UCB): This function trades off exploration and exploitation by considering both the mean and the variance of the surrogate model. It seeks to minimize the regret of not evaluating potentially better points.

- Probability of Improvement (PI): This function selects the point that has the highest probability of improving upon the current best solution. It focuses more on exploitation and is suitable when the objective function is well understood.

Bayesian optimization proceeds iteratively by sequentially evaluating the objective function at the selected points. The surrogate model is updated based on the observed data, and the acquisition function is recalculated to select the next point for evaluation (see **Fig.2.4**). This process continues until a termination criterion is met, such as reaching a maximum number of iterations or achieving a satisfactory solution.
The benefits of Bayesian optimization include its ability to handle noisy and expensive objective functions, its adaptability to different types of optimization problems, and its efficiency in finding optimal solutions with limited function evaluations. It has been successfully applied in various domains, including hyperparameter tuning of machine learning models, experimental design, robotics, and drug discovery [94]. It is important to note that the effectiveness of Bayesian optimization relies on choosing appropriate surrogate models, priors, and acquisition functions

that suit the characteristics of the optimization problem. Additionally, the computational cost of Bayesian optimization can become a limitation when dealing with high-dimensional or computationally expensive problems.

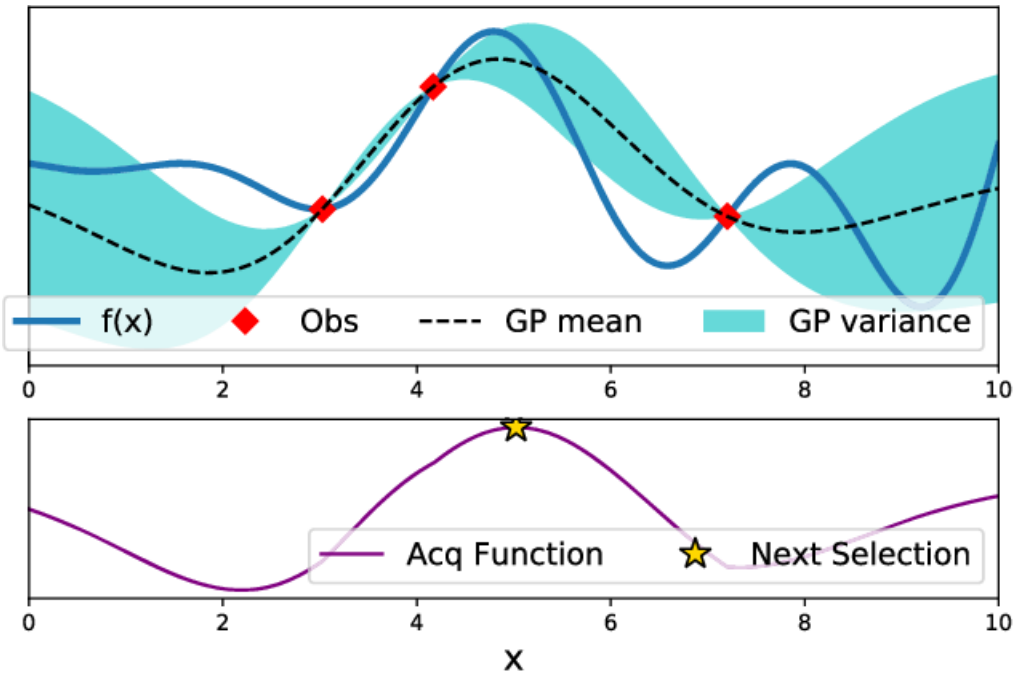

Figure 2.4. Example of Gaussian process and Bayesian optimization which suggests the next optimal point to evaluate given initial three observations [95].

Chapter 3

Estimation of the diffusion coefficient of GaSb in InSb melt using Bayesian optimization and the ISS experimental results

3.1 Background and purpose

As already stated in previous sections, the undesirable effects of natural convection can be minimized under microgravity, which is an appropriate environment for investigating the growth kinetics and gain deeper insight into the transport phenomena involved. Therefore, valuable crystal growth space experiments have been carried out for that purpose. Microgravity environment not only allows the growth of high quality homogeneous crystals, but also largely increases the growth rates compared with the crystals grown on Earth. However, the dominant factors, which determines the feed/seed dissolution rates and the crystal growth rates remain uncertain. In our study, we focus mainly on the experimental work performed onboard the International Space Station (ISS) [55]. InGaSb alloy crystal was grown under prolonged microgravity by Vertical Gradient Freezing (VGF) method using a GaSb(seed)/Te-dopped InSb/GaSb(feed) sandwich-structured sample as illustrated in **Fig. 3.1**. In this method, the sample is subjected to a fixed temperature gradient in the axial direction being hotter at the top and cooler at the bottom. The system is heated over the melting point of InSb which melts first. GaSb material then dissolves in the molten InSb (dissolution process) resulting in a mixture of InGaSb (growth solution) that becomes supersaturated under the applied temperature profile. GaSb is fed from the higher temperature feed crystal into the solution and $In_xGa_{1-x}Sb$ crystal grows on the surface of the lower temperature seed crystal (growth process).

Microgravity experiments with different GaSb crystal orientations (111A, 111B, 110, and 100)

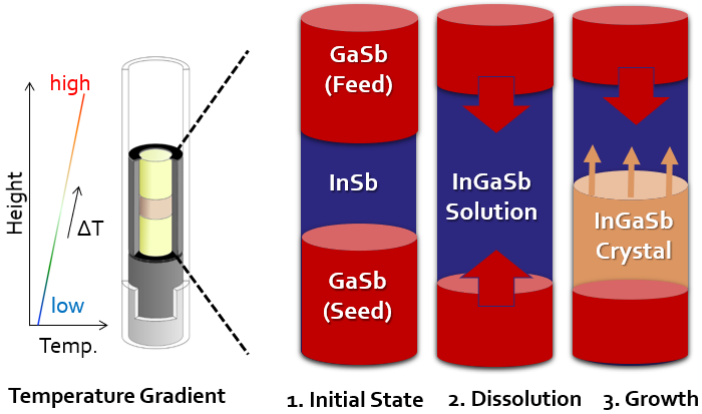

Figure 3.1. Schematic diagram of the Vertical Gradient Freezing method [55].

had been conducted for the growth of InGaSb crystals. Similar heating profiles and heat pulses for each sample were applied during the growth process in order to induce striations in the grown crystals, indicating solid–liquid interface shapes and growth rates at various time periods. The temperature inside the cartridge was measured and recorded by five equidistant thermocouples positioned at 21 mm intervals, covering the whole ampoule height as shown in **Fig. 3.2**, which was adequate to monitor and record the temperature at various positions of the ampoule during the growth experiment [96]. Experimental temperature gradients and growth rates are compared in **Fig. 3.3**. The results showed differences in the crystal growth rates between the samples, which is attributed to the effects of interfacial kinetics that depend on the orientation of the crystals.

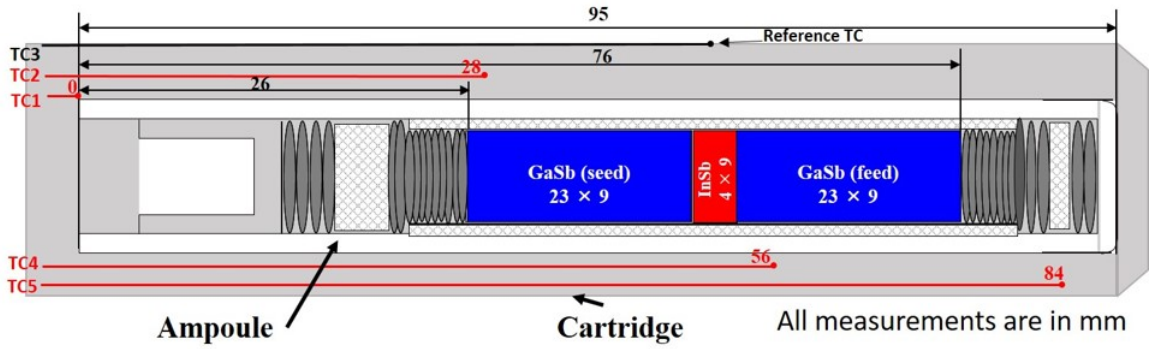

Figure 3.2. Design of the cartridge containing the ampoule and position of the thermocouples [55].

Unsurprisingly, the opportunity to reproduce such space experiments and further investigate the growth kinetics is rare, expensive and cannot be available for a full-scale study. To this end, we invoke the numerical approach by developing a numerical analysis technique and using the results of the experiments performed on the ISS. As in any numerical study, the physical properties need

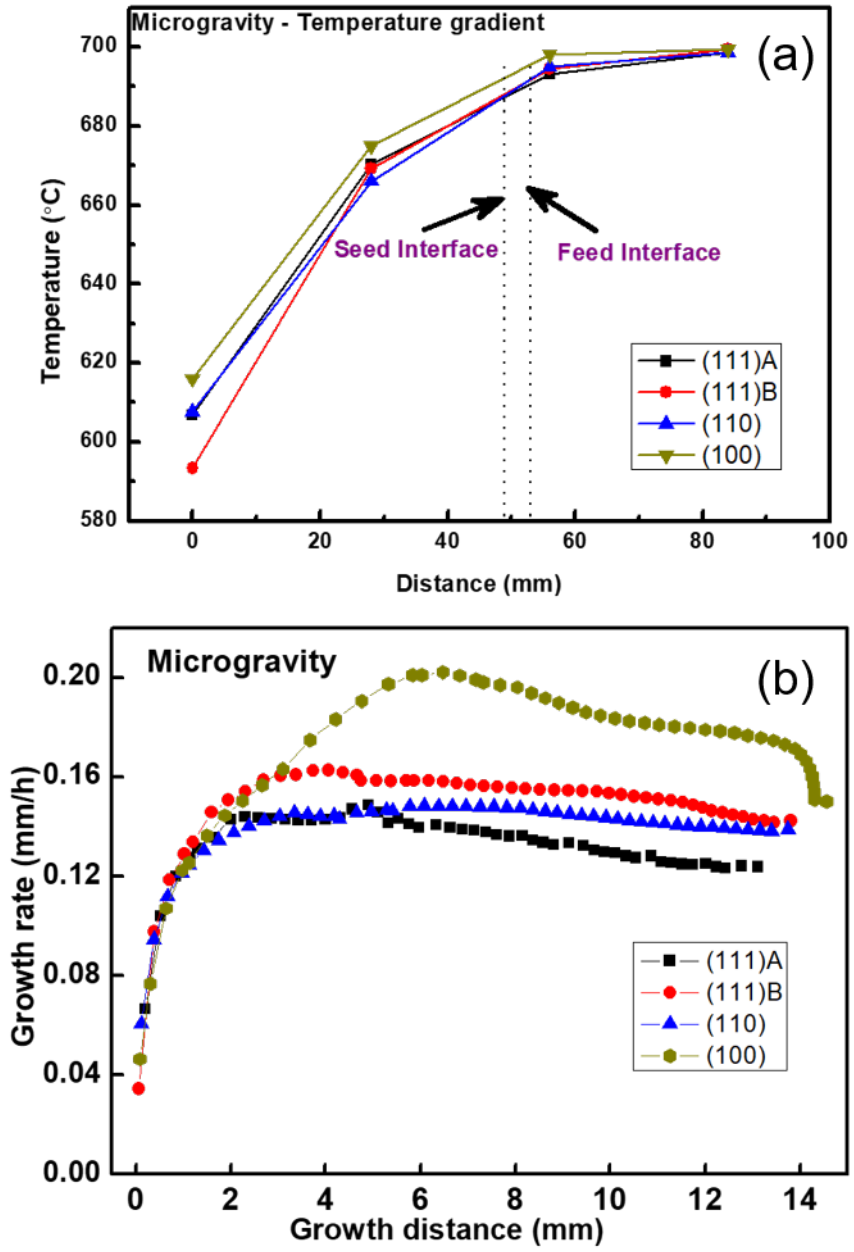

Figure 3.3. Comparison between temperature gradients (a) and growth rates (b) of samples with different GaSb orientations in the microgravity experiments [55].

to be accurately defined, however, measurements of diffusion coefficients on Earth are affected by natural convection. Thus, numerical simulation models using these diffusion coefficients overpredict growth and dissolution rates. Therefore, in order to provide more accurate diffusion coefficient estimations, we analyzed the available microgravity experimental results by utilizing Bayesian optimization methods.

3.2 Numerical Analysis

3.2.1 Simulation model

A schematic description of the InGaSb crystal dissolution/growth system used is shown in **Fig. 3.4**. The GaSb(feed)/Te-dopped InSb/GaSb(seed) sandwich sample was stacked in a quartz ampoule and sealed with Boron Nitride (BN) and carbon sheet as seen in **Fig. 3.4(a)**. The system was subjected to three vertical temperature gradients (**Fig. 3.4(b)**) with the top being hotter and the bottom being cooler. The whole system was heated at a heating rate of 0.001 K/s up to the target temperature and then kept constant. The grid system used for the simulation is also shown in **Fig. 3.4(c)**.

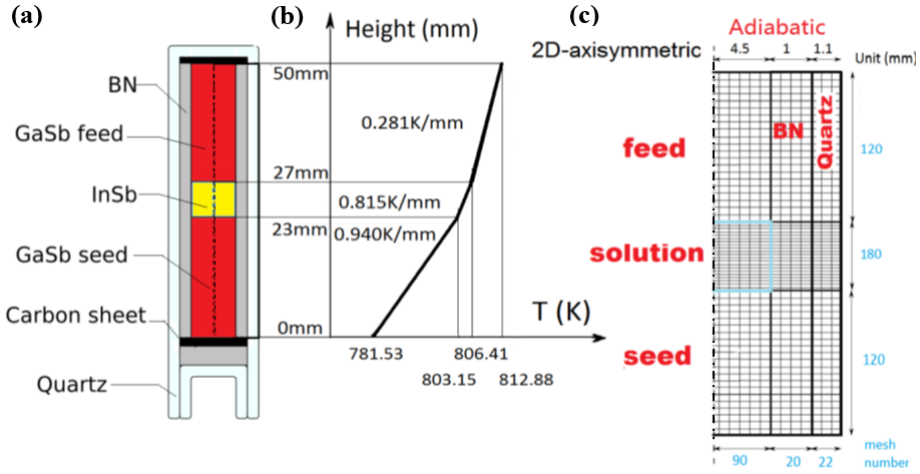

Figure 3.4. Schematics of the growth ampoule (a), the applied temperature profile (b) and the grid system of the simulation (c) [64].

3.2.2 Governing equations

In the present numerical simulation model, the following assumptions were made:

(1) Liquid phase is an incompressible Newtonian fluid;
(2) Densities of the solid and liquid phases are constant, thus the associated volume changes (shrinkage and expansion) during phase changes are negligible;
(3) Changes in physical properties (because of compositional variations) during the dissolution and growth processes are not significant;
(4) The complete molten state of InSb was regarded as the initial state, thus, the initial GaSb concentration in the solution was taken zero;
(5) The g-jitter effect (gravity fluctuation) on the ISS was not taken into account.

The calculation region consists of the Crystal, the BN crucible and the Quartz ampoule whose physical properties and operational conditions are listed in **Table 3.1**. Under the above assumptions, the governing equations of the liquid phase, namely continuity, momentum conservation, energy conservation and mass transport equations are given as:

$$\nabla \cdot \boldsymbol{u} = 0 \tag{3.1}$$

$$\frac{\partial \boldsymbol{u}}{\partial t} + (\boldsymbol{u} \cdot \nabla)\boldsymbol{u} = -\frac{1}{\rho}\nabla p + \nu \nabla^2 \boldsymbol{u} + \boldsymbol{g}(\beta_{\mathrm{T}} \Delta T + \beta_{\mathrm{C}} \Delta C) \tag{3.2}$$

$$\frac{\partial T}{\partial t} + (\boldsymbol{u} \cdot \nabla)T = \alpha \nabla^2 T \tag{3.3}$$

$$\frac{\partial C}{\partial t} + (\boldsymbol{u} \cdot \nabla)C = \nabla \cdot (D \nabla C) \tag{3.4}$$

where u is the velocity, ρ density, p pressure, ν kinematic viscosity, g gravitational acceleration, β_{T} thermal expansion coefficient, β_{C} solutal expansion coefficient, T temperature, α thermal diffusivity, and C and D are, respectively, the concentration and diffusion coefficient of GaSb. In the solid phases (BN and Quartz), only the energy balance equation is considered:

$$\frac{\partial T}{\partial t} = \alpha_{\mathrm{i}} \nabla^2 T \tag{3.5}$$

i subscript standing for BN and Quartz.

Table 3.1 Physical properties and operating conditions used in the numerical study [97, 98, 99].

Physical property	**Symbol**	**Value**
	InGaSb	
Thermal conductivity	λ_{L} [W/(m K)]	17
Specific heat	$c_{p\mathrm{L}}$ [J/(kg K)]	300
Viscosity	μ_{L} [Pa s]	$1.1 \cdot 10^{-3}$
Thermal diffusivity	α_{L} [m^2/s]	$9.0 \cdot 10^{-6}$
Kinematic viscosity	ν_{L} [m^2/s]	$1.7 \cdot 10^{-7}$
Latent heat	L [J/kg]	$3.1 \cdot 10^{5}$
Thermal expansion coefficient	β_{T} [1/K]	$1.0 \cdot 10^{-4}$
Solutal expansion coefficient	β_{C} [-]	0.05
Electrical conductivity	σ [S/m]	$1.0 \cdot 10^{6}$
Melting point	T_{InGaSb} [K]	979
Density	$\rho_{\mathrm{InGaSb(s)}}$ [kg/m^3]	5600
	$\rho_{\mathrm{InGaSb(l)}}$ [kg/m^3]	6060
	GaSb	
Density	$\rho_{\mathrm{GaSb(s)}}$ [kg/m^3]	5610
	$\rho_{\mathrm{GaSb(l)}}$ [kg/m^3]	6010
Melting point	T_{GaSb} [K]	985
	InSb	
Density	$\rho_{\mathrm{InSb(s)}}$ [kg/m^3]	5780
	$\rho_{\mathrm{InSb(l)}}$ [kg/m^3]	6320
Melting point	T_{InSb} [K]	800
	Quartz	
Thermal conductivity	λ_{Q} [W/(m K)]	2.68
Density	ρ_{Q} [kg/m^3]	2200
Specific heat	$c_{p\mathrm{Q}}$ [J/(kg K)]	1000
Thermal diffusivity	α_{Q} [m^2/s]	$1.0 \cdot 10^{-6}$
	BN	
Thermal conductivity	λ_{BN} [W/(m K)]	54
Density	ρ_{BN} [kg/m^3]	2280
Specific heat	$c_{p\mathrm{BN}}$ [J/(kg K)]	2900
Thermal diffusivity	α_{BN} [m^2/s]	$8.2 \cdot 10^{-6}$
	Operational conditions	
GaSb Feed/Seed lengths	[mm]	23
InSb length	[mm]	3
BN crucible diameter	[mm]	11
Quartz ampoule diameter	[mm]	13.2
Crystals diameter	[mm]	9

3.2.3 Boundary conditions and discretization

The boundary conditions for the top and bottom walls are adiabatic for the temperature field, no-slip conditions for the velocity field, and no flux condition (in the normal direction to the ampoule walls) for the concentration field. In addition, on the boundaries between the feed and seed crystals, the walls and the seals (BN and Quartz) are assumed no-slip condition for the velocity field. The same along the normal direction to the wall and seal boundaries; no mass and heat fluxes are allowed. On the outside of the ampoule along the outer walls, the temperature profile has been determined from the measured values from the ISS experiment [55]. The simulation was performed under the microgravity level of 10^{-4} G which corresponds to a typical average gravity level observed on the ISS. The gravity direction was aligned with the axis of the sandwich system and directed towards the seed crystal. The governing equations together with the boundary conditions were discretized by the finite volume method and the pressure-velocity coupling was handled by the Pressure Implicit with Splitting of Operators (PISO) algorithm and then solved using the open-source CFD code: OpenFOAM [65] and the new volume-average continuum model. This model utilizes volume fractions of the solid and liquid phases determined by using the applied temperature and concentration profiles, as well as the phase diagram of the binary system GaSb-InSb. Relevant details on the numerical method and its code validation for different and similar systems can be found in previous articles [64, 57].

3.3 Results and discussion

3.3.1 Initial estimation: Constant diffusion coefficient

Figure 3.5(a) illustrates the growth rate variation along the growth direction for the case where GaSb (111)A crystal orientation was used in the µG experiments (black dots) and the initial numerical calculations (blue curve). To measure the experimental growth rate of the crystal, periodic intentional heat pulses were applied during the growth process. By means of such heat pulses, the tellurium impurity concentration modulates and consequently gives rise to growth striations in the grown crystal, which show the evolution of the solid/liquid interfaces during growth. Measuring the distances between these growth striations determines the growth rate [55].

When the reported diffusion coefficient value [98] is used, large discrepancies are observed as the calculated growth rate is found to be much higher than that of the experiments. This reached a maximum of about 0.15 mm/h, while the predicted growth rate surpasses this value and attains 0.6 mm/h.

Considering that, onboard the ISS, the gravity-driven convection in the melt is minimized and diffusion-controlled heat and mass transport conditions are achieved, it is anticipated that the crystal growth rate is strongly affected by the diffusion coefficient of GaSb in the InSb melt.

Initially, the value of the diffusion coefficient used in the calculation is taken from the literature as $D = 1.2 \cdot 10^{-8}$ m^2/s [98]. It is assumed to be too large, hence, we optimized this value and determined that using a diffusion coefficient of about a fifth of the initial value ($D = 0.22 \cdot 10^{-8}$ m^2/s) reproduced better results as shown in **Fig. 3.5(b)** where the experimental and calculated growth rates for three different GaSb orientations ((111)A, (111)B and (110)) are plotted. For instance, with reference to GaSb (111)A crystal orientation case, the calculated growth rate has the same tendency as the experimental one. It reaches a value of about 0.14 mm/h at 6 mm of crystal grown length and 0.124 mm/h at the end of growth, with the final crystal length being 13 mm. However, the value of $D = 0.22 \cdot 10^{-8}$ m^2/s is not as adequate for the other GaSb orientations (111)B and (110).

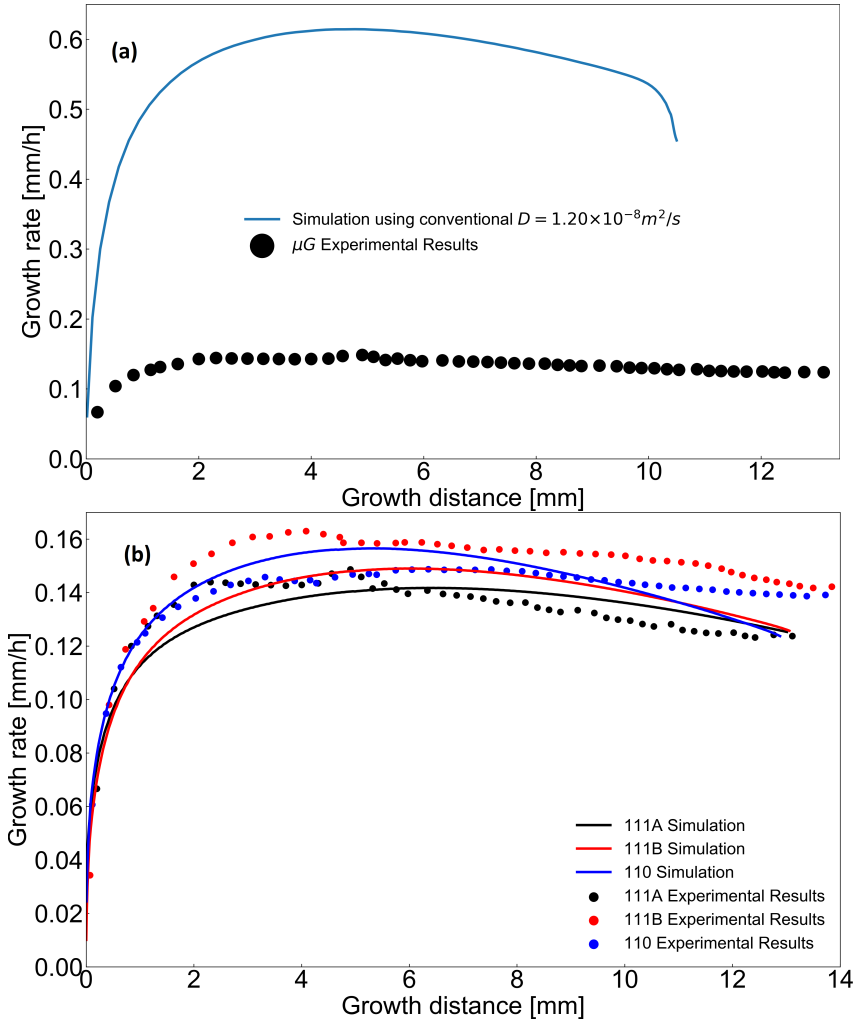

Figure 3.5. Comparison between the experimental and calculated growth rates using conventional (a) and modified (b) diffusion coefficient.

Furthermore, we notice that for both the experiment and simulation, the growth rate at the initial stage of growth is relatively low and then gradually increases. This could be explained by the

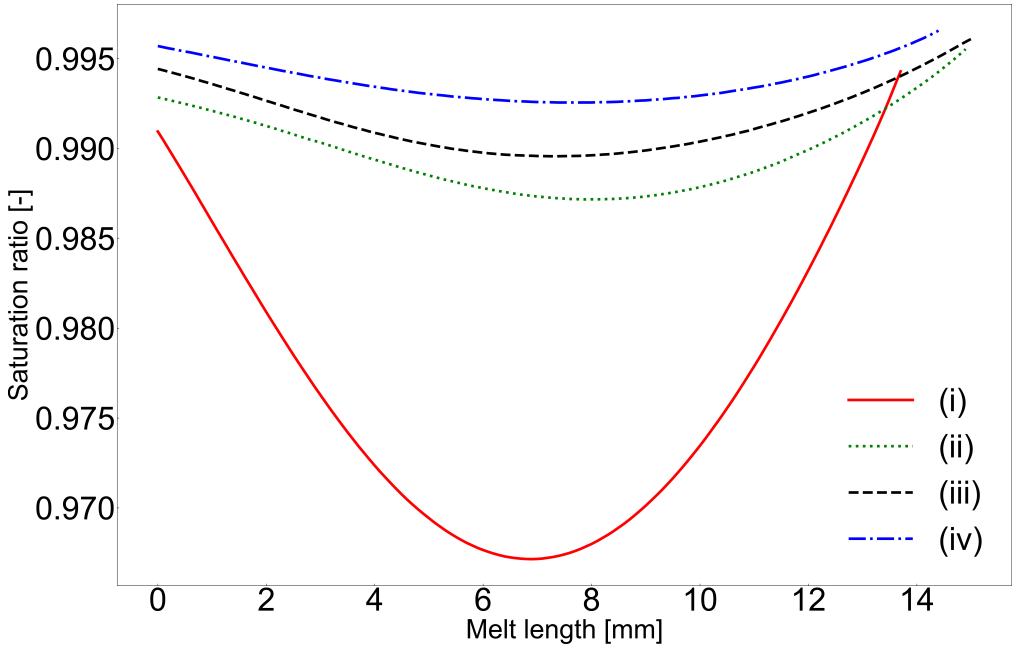

Figure 3.6. Melt saturation ratio during different stages of growth: initial stage (i), middle stages (ii-iii) and end of growth (iv).

low saturation in the melt during the early stages of growth as illustrated in **Fig. 3.6**, where the saturation ratio along the melt is plotted in four different stages of growth: beginning of growth (i), middle stages (ii, iii) corresponding to a crystal length of 2 mm and 7 mm after a growth time of 16 h and 50 h respectively and final stage (iv) that is after 105 h of growth. It is deduced that the amount of GaSb supplied to the melt was not yet sufficient during the first stages of growth (steps i to ii), but then the melt progressively becomes saturated due to the feed crystal further dissolution and the growth rate increases reaching the steady-state growth (steps ii to iv). The results presented in **Fig. 3.6** show that:
- The solute concentration clearly affects the diffusion-controlled crystal growth process; and
- The use of a constant diffusion coefficient value does not lead to good predictions in the calculations for all three GaSb orientations.

In addition, a solute concentration dependence of the diffusivity for the growth of InGaSb alloy by the Bridgman method was once introduced [100], but, to the best of our knowledge, the subject was not further studied. In order to examine the validity of this assumption, we decided to investigate the effect of solute concentration on diffusivity and the crystal growth process.

3.3.2 Optimization: Concentration-dependent diffusion coefficient

In general, the Arrhenius equation can be used to predict the temperature variation of diffusion coefficients for thermally induced processes. In our model, a number of similar expressions, but

considering the solute concentration instead, was tried out, and Eq. (3.6) was found to be the most suitable one as it gives the best predictions in terms of growth rates and feed dissolution lengths. Hence, it is adopted as a model equation to estimate the diffusion coefficient of GaSb in InSb melt.

$$D = D_0 \times e^{b \cdot C} \tag{3.6}$$

where C is the solute concentration in the melt, and D_0 and b represent the parameters to be determined relying on the ISS experimental results and using Bayesian optimization algorithms to ensure computational time and cost-efficiency.

Bayesian Optimization

In Bayesian optimization, we search for the parameter vector $\boldsymbol{x} = (x_0, ..., x_\mathrm{n})^\mathrm{T}$ that maximizes the objective function $y = f(\boldsymbol{x})$ based on the Gaussian process regression and using the variance and the predicted mean value.

Supposing that D is a known dataset obtained by initial trials: $D = \{(\boldsymbol{x}^0, y^0), ..., (\boldsymbol{x}^\mathrm{m}, y^\mathrm{m})\}$, If the value y^new of the objective function at the new parameter $\boldsymbol{x}^\mathrm{new} = ({x_0}^\mathrm{new}, ..., {x_\mathrm{n}}^\mathrm{new})^\mathrm{T}$ is predicted by Gaussian process regression using the dataset D, then y^new follows the Gaussian distribution and its mean value m and variance σ^2 are as follows:

$$m = \boldsymbol{k}^\mathrm{T} \boldsymbol{\Sigma}^{-1} \boldsymbol{y} \tag{3.7}$$

$$\sigma^2 = \boldsymbol{K}(\boldsymbol{x}^\mathrm{new}, \boldsymbol{x}^\mathrm{new}) - \boldsymbol{k}^\mathrm{T} \boldsymbol{\Sigma}^{-1} \boldsymbol{k} \tag{3.8}$$

where

$$\boldsymbol{k} = \begin{pmatrix} \boldsymbol{K}(\boldsymbol{x}^1, \boldsymbol{x}^\mathrm{new}) \\ \vdots \\ \boldsymbol{K}(\boldsymbol{x}^\mathrm{m}, \boldsymbol{x}^\mathrm{new}) \end{pmatrix} \quad \boldsymbol{\Sigma} = \begin{pmatrix} \boldsymbol{K}(\boldsymbol{x}^1, \boldsymbol{x}^1) & \dots & \boldsymbol{K}(\boldsymbol{x}^1, \boldsymbol{x}^\mathrm{m}) \\ \vdots & \ddots & \vdots \\ \boldsymbol{K}(\boldsymbol{x}^\mathrm{m}, \boldsymbol{x}^1) & \dots & \boldsymbol{K}(\boldsymbol{x}^\mathrm{m}, \boldsymbol{x}^\mathrm{m}) \end{pmatrix} \tag{3.9}$$

and $\boldsymbol{K}(\boldsymbol{x}^\mathrm{i}, \boldsymbol{x}^\mathrm{j})$ is the kernel function used in this research and is defined as:

$$\boldsymbol{K}(\boldsymbol{x}^\mathrm{i}, \boldsymbol{x}^\mathrm{j}) = \theta_0 \exp\left(-\frac{\theta_1}{2} \parallel \boldsymbol{x}^\mathrm{i}, \boldsymbol{x}^\mathrm{j} \parallel^2\right) + \theta_2 \tag{3.10}$$

θ_0, θ_1 and θ_2 are hyperparameters determined by the maximum likelihood estimation.

In Bayesian optimization, an acquisition function $a(\boldsymbol{x})$ is used in order to decide the next sample point ($\boldsymbol{x}^\mathrm{next}$) so as:

$$\boldsymbol{x}^\mathrm{next} = \arg\max_x a(\boldsymbol{x}) \tag{3.11}$$

In other words, the parameter with the largest value of the acquisition function is the parameter that should be calculated next. There are a wide variety of acquisition functions that can be used

in Bayesian Optimization. In our research, we used 3 types of acquisition functions: Probability of Improvement (PI), Expected Improvement (EI) and Upper Confidence Bound (UCB).
The flow of the Bayesian optimization is shown in **Fig. 3.7** and is performed using the python machine learning library *scikit-learn* [101][102]. An example code used in our research is also shown in the Appendix.

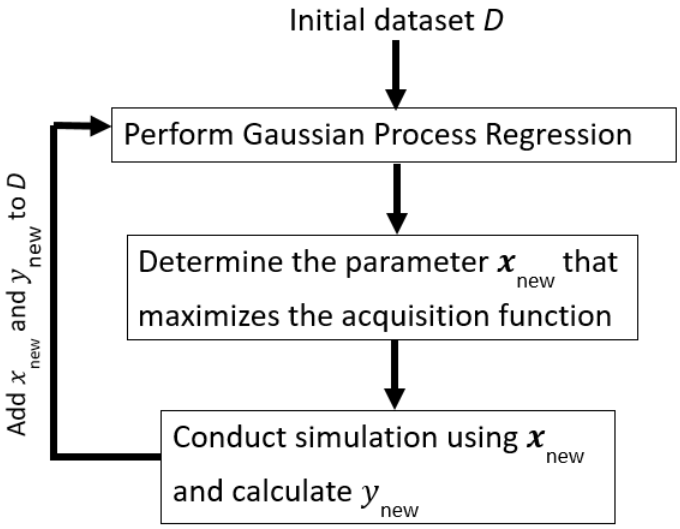

Figure 3.7. Flowchart of the Bayesian Optimization.

In this research work, the diffusion coefficient is estimated from Eq. (3.6) after determining the two unknowns b and D_0 using Bayesian Optimization. The crystal growth rate V and the mean squared error MSE are defined for that purpose:

$$V = \frac{l}{t_{\text{growth}}} \tag{3.12}$$

$$MSE = \frac{1}{l}\int (V_{\text{sim}}(l') - V_{\text{exp}}(l'))^2 dl' \tag{3.13}$$

where l is the crystal growth length, t_{growth} is the elapsed time from the beginning of the growth and $V_{\text{sim}}(l')$ and $V_{\text{exp}}(l')$ are, respectively, the calculated and experimental values of the growth rate at the crystal length l'.
The parameter $\boldsymbol{x}$ and the objective function y are also selected as:

$$\boldsymbol{x} = \begin{pmatrix} D_0 \\ b \end{pmatrix} \qquad y = -\text{MSE} \tag{3.14}$$

This implies that maximizing the objective function y is equivalent to minimizing the mean square error MSE.
After multiple iterations, the optimal parameters for maximizing the objective function are obtained as

$D_0 = 2.7 \cdot 10^{-8}$ m^2/s and $b = -3$

The numerical results are in agreement with the experimental data only if a dependence of the diffusion coefficient on the solute concentration is taken into account in the simulation. An exponential decrease of the diffusion coefficient, when GaSb concentration increases, is found and follows the expression:

$$D = 2.7 \cdot 10^{-8} \times e^{-3 \cdot C} \tag{3.15}$$

This relationship can also be utilized for low concentrations, however, the initially performed numerical calculations indicated that it is particularly suitable in the GaSb concentration range throughout the InGaSb crystals growth stage ($0.7 < C < 0.9$), as the value of the diffusion coefficient used prior to that did not have a notable effect on crystal growth rates.

The change of the average solute concentration throughout the growth process, as well as the corresponding diffusion coefficients for the growth of InGaSb crystals from GaSb (111)A orientation, are shown in **Fig. 3.8**.

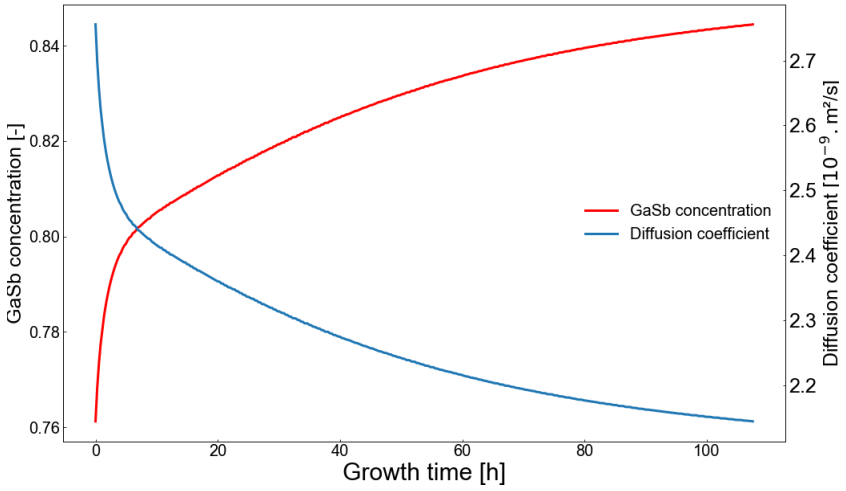

Figure 3.8. Variation of the average GaSb concentration in the solution over time and the corresponding diffusion coefficients of GaSb in the InSb melt.

Figure 3.9 compares between the experimental and computed crystal growth rates using the new equation of the diffusion coefficient for three different GaSb crystal orientations: (111)A, (111)B and (110).

It is deduced that the developed concentration-dependent diffusion coefficient gives fairly accurate predictions, especially during the early stages of the growth process when the saturation ratio of the melt was relatively low. A similar order to the space experiments in terms of growth rate values was also followed Case(111)B > Case(110) > Case(111)A.

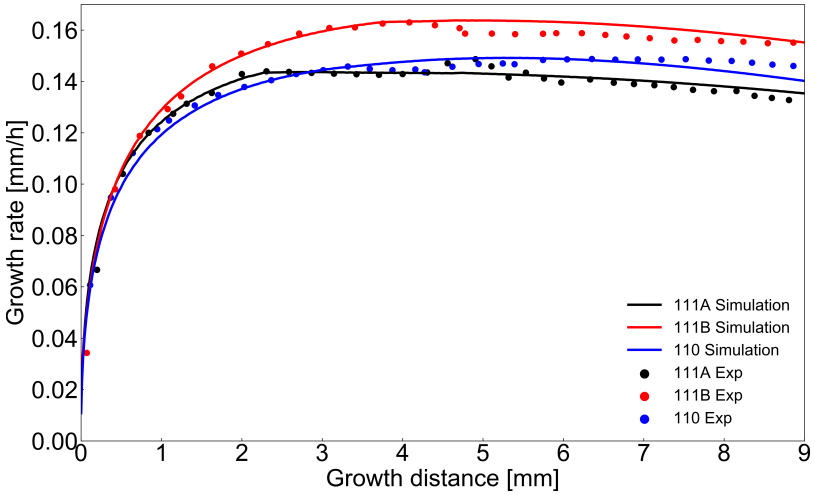

Figure 3.9. Experimental and computed growth rates using the newly developed diffusion coefficient equation for three different GaSb crystal orientations.

3.4 Conclusion

In this study, a relationship between the diffusion coefficient of GaSb in InSb melt and its concentration was established based on the International Space Station experimental results. Bayesian optimization methods were also utilized in order to resolve the computational demand issue.

The suppressed convection under μG affects greatly the dissolution and growth process of InGaSb alloy semiconductor and it is concluded that under diffusion-controlled environment, the growth rate, the feed and seed dissolution rates, as well as the final grown crystal length are influenced by the diffusion coefficient values, thus, GaSb concentration variation in the melt.

The experimental results are in good agreement with the numerical results provided that an exponential variation of the coefficient of diffusion according to the solute concentration is taken into account in the numerical calculations. This modified numerical model can be implemented in further calculations to identify optimization possibilities using various methods, such as applying to the system external fields (magnetic field, vibration, rotation...) so as to reach high and uniform crystal growth rate and improve its quality on earth gravity level.

Research remains to be conducted on the study of the variation of the diffusion coefficient as a function of the concentration for other materials in order to find a possible physical explanation at the molecular level for this phenomenon.

Chapter 4

Control of growth interface shape during InGaSb growth by Vertical Gradient Freezing method under microgravity, and optimization using machine learning

4.1 Background and purpose

In the growth of InGaSb crystals by Vertical Gradient Freezing (VGF) method, the interface shape is a dominant factor affecting the quality and homogeneity of the grown crystals. Its optimal control is therefore very important. However, this is a difficult task because of the influence of natural convection in the melt, compositional segregation, and heat and mass transfer in the vicinity of the dissolution and growth interfaces [26, 24, 25]. As a general rule, to prevent solvent inclusions and polycrystalline growth, a convex or flat growth interface shape is desirable. The use of inadequate growth conditions will indubitably result in undesirable interface shape deformations. To address this issue, an axisymmetric two-dimensional numerical simulation analysis is carried out to determine the conditions for an optimum growth interface shape using a combination of different techniques.

This study is conducted under microgravity and reproduces conditions similar to those of the experiments performed onboard the International Space Station (ISS) by Inatomi *et al.* [55]. Microgravity is an appropriate environment where the undesirable effect of natural convection can be minimized for better quality crystals [103, 104]. In addition, such experiments may also help to gain a deeper insight into the transport phenomena and growth kinetics involved in growth of InGaSb crystals. As for crystal growth optimization possibilities, the utilized experimental apparatus onboard the ISS is rather restricted, and thus the application of external forces for optimization, such as magnetic fields, is either not possible or difficult and limited.

It is known that the temperature gradient is a dominant factor of seed/feed dissolution rates and interface shapes in crystal growth by Vertical Gradient Freezing method. Besides, some studies [105, 46, 106] reported that applying crucible rotation with an adequate rotation rate is generally beneficial in suppressing natural convection in the melt and obtaining an interface shape with a smaller curvature. These alternatives (optimization of the thermal boundary conditions and application of crucible rotation) seem to hold great potential and therefore are considered in this study for the growth of homogeneous InGaSb crystals.

In recent years, AI and machine learning tools are increasingly being used in fluid control and crystal growth problems [107, 108, 109, 110]. We utilized for instance Bayesian optimization in our previous work [111] for the estimation of the diffusion coefficient of GaSb in InSb melt. This approach showed promising results and proved to be useful for the rapid estimation of unknown variables. Wang *et al.* [109] also developed a reinforcement learning model to control the melt flow in the radio frequency (RF) top-seeded solution growth (TSSG) process for the growth of uniform SiC crystals.

In this chapter, we discuss the results of combining Computational fluid dynamics (CFD), Bayesian optimization, and reinforcement learning for determination of control parameters in the growth of high quality InGaSb crystals with a higher growth rate.

4.2 Numerical Analysis

4.2.1 Simulation model

A GaSb(111)A/Te-doped InSb/GaSb(111)A sandwich sample was used for the VGF growth of InGaSb bulk crystal under µG on the ISS. A schematic description of the dissolution and growth system used in the simulation is shown **Fig. 4.1**. The sample was stacked in a quartz tube and sealed with Boron Nitride (BN) and carbon sheet as seen in **Fig. 4.1(a)** and was subjected to a fixed temperature gradient (**Fig. 4.1(b)**) with the top being hotter and the bottom being cooler. The whole system was heated at a heating rate of 0.01 K/s up to the target temperature (heating period) and then kept constant (keeping period) until the end of the growth process. The two-dimensional axisymmetric rectangular computational domain used for the simulation is also shown in **Fig. 4.1(c)**. The computational domain is divided into 132 (x-axis) and 420 (y-axis) segments and a non-uniform mesh arrangement with local clustering close to the liquid-solid interfaces is used to allow an efficient meshing in the high gradient regions. The mesh size was selected after a dependency study performed for several different mesh sizes. The fineness of the mesh was based on a reasonable balance between accuracy and computing time. Having a sufficiently high mesh number in the central area is also crucial in order to assure precise and smooth interface shapes.

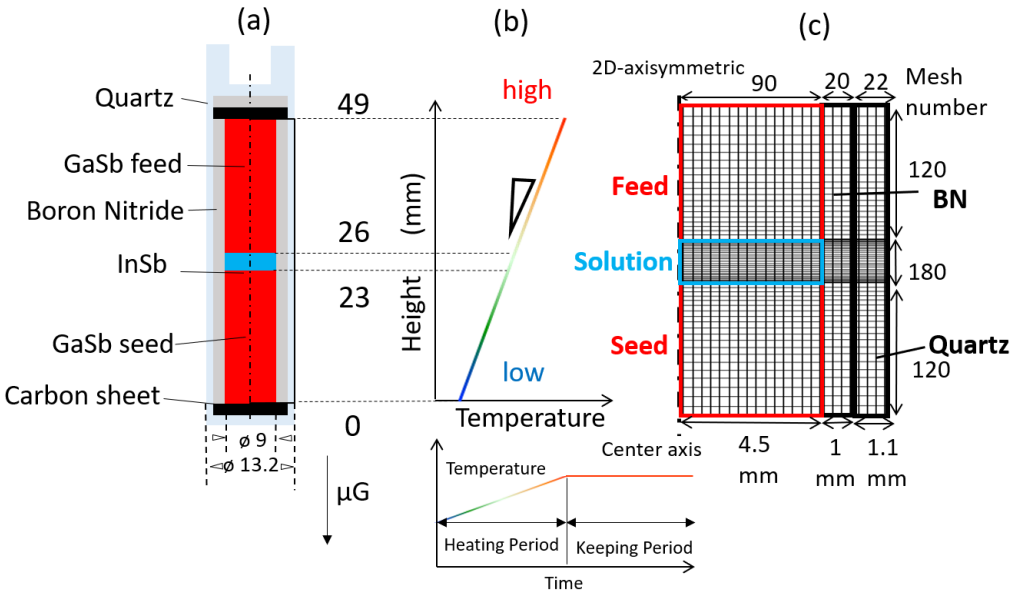

Figure 4.1. Schematics of the Vertical Gradient Freezing method: growth ampoule (a), applied temperature profile (b) and grid system of the simulation (c) [63, 64].

4.2.2 Governing equations and associated boundary conditions

The following assumptions were made in the present numerical simulation model:
(i) Liquid phase (InGaSb solution) is an incompressible Newtonian fluid;
(ii) Densities of the solid and liquid phases remain constant, thus the associated volume changes (shrinkage and expansion) due to phase changes are negligible;
(iii) Changes in physical properties resulting from compositional variations during the dissolution and growth processes are not significant;
(iv) The complete molten state of InSb was regarded as the initial state, thus, the initial GaSb concentration in the solution was taken zero;
(v) Gravity fluctuations (g-jitter effect) on the ISS were not taken into account and the microgravity level of 10^{-4} G (that corresponds to a typical average gravity level observed on the ISS) was used in the simulation.

Three calculation regions are considered: Crystal, BN crucible and Quartz ampoule whose physical properties and operating conditions are shown in the previous chapter.

Under the assumptions mentioned above, the governing equations of the liquid phase, namely

continuity, momentum balance, energy, and mass transport equations are given as:

$$\nabla \cdot \boldsymbol{u} = 0 \tag{4.1}$$

$$\frac{\partial \boldsymbol{u}}{\partial t} + (\boldsymbol{u} \cdot \nabla)\boldsymbol{u} = -\frac{1}{\rho}\nabla p + \nu \nabla^2 \boldsymbol{u} + \boldsymbol{g}(\beta_{\mathrm{T}} \Delta T + \beta_{\mathrm{C}} \Delta C) + \frac{\boldsymbol{F}_{\mathrm{r}}}{\rho} \tag{4.2}$$

$$\frac{\partial T}{\partial t} + (\boldsymbol{u} \cdot \nabla)T = \alpha \nabla^2 T \tag{4.3}$$

$$\frac{\partial C}{\partial t} + (\boldsymbol{u} \cdot \nabla)C = \nabla \cdot (D \nabla C) \tag{4.4}$$

where u is the flow velocity, ρ melt density, p pressure, ν kinematic viscosity, g gravitational acceleration, β_T thermal expansion coefficient, β_C solutal expansion coefficient, T temperature, α thermal diffusivity, $\boldsymbol{F}_{\mathrm{r}}$ centrifugal force term, C solute concentration and D is the diffusion coefficient of GaSb in InSb melt defined as [111]:

$$D = 2.7 \cdot 10^{-8} \cdot e^{-3 \cdot C} \tag{4.5}$$

For the solid phases, the governing equation is the following heat conduction equation:

$$\frac{\partial T}{\partial t} = \alpha_{\mathrm{i}} \nabla^2 T \tag{4.6}$$

i subscript stands for BN and Quartz.
- No slip condition on flow velocity is assumed on all boundary walls (top and bottom walls, boundaries between the feed/seed crystals, walls and seals (BN and Quartz));
- No flux condition (in the normal direction to the ampoule walls) for the concentration field;
- Top and bottom walls are adiabatic for the temperature field.
The governing equations together with the boundary conditions were discretized by the finite volume method and the pressure-velocity coupling was handled by the Pressure Implicit with Splitting of Operators (PISO) algorithm and then solved using OpenFOAM, an open-source CFD software package and the new volume-average continuum model [65, 57]. This model utilizes volume fractions of the solid and liquid phases determined by using the applied temperature and concentration profiles, as well as the phase diagram of the binary system GaSb-InSb.

4.3 Results and discussion

4.3.1 Bayesian optimization: Fixed control recipe

In our previous work [111], Bayesian optimization was utilized to construct an equation relating the diffusion coefficient of GaSb in InSb melt to its concentration. This allowed us to estimate more accurately the crystal growth rates and explain the microgravity experimental results. The same principle is applied here but with different parameters and objective functions. The

optimization process flow is summarized in **Fig. 3.7** and is performed using the python machine learning library *scikit-learn* [101, 102]. The goal of Bayesian optimization is to search for the parameter vector $\boldsymbol{x} = (x_0, ..., x_n)_T$ that maximizes an objective function $y = f(\boldsymbol{x})$ based on the Gaussian process regression and using the variance and the predicted mean value.

In this numerical study, the growth interface shape is investigated from the computed solute concentration distribution as shown in **Fig. 4.2(a-c)**. During the calculations, the interface positions were determined at each time step and the growth interface shape change was evaluated from the difference between the growth interface positions at the periphery Y_p and at the center axis Y_c. The degree of deformation ΔY_d is then calculated as:

$$\Delta Y_d = Y_p - Y_c \tag{4.7}$$

Hence, a large positive value of ΔY_d indicates an undesirable highly concave interface shape, a value closer to zero indicates a flat one and a negative value is an indicator of a favorable convex growth interface shape. Accordingly, we aim to minimize ΔY_d by means of crucible rotation and the use of different thermal boundary conditions. The temperature gradient $\frac{\Delta T}{\Delta Y}$ and the rotation speed ω represent therefore the control parameters to be optimized for controlling the growth interface shape of InGaSb crystal and improving its quality.

The parameter $\boldsymbol{x}$ and the objective function y are selected as:

$$\boldsymbol{x} = \begin{pmatrix} \frac{\Delta T}{\Delta Y} \\ \omega \end{pmatrix} \qquad\qquad y = -1 \times M^*_{\Delta Y_d} \tag{4.8}$$

$M*_{\Delta Y_d}$ is the normalized mean of the deformation rate such as:

$$M^*_{\Delta Y_d} = \frac{M_{\Delta Y_d}}{M_{\Delta Y_d}|_{\omega=0}} \tag{4.9}$$

Where $M_{\Delta Y_d}|_{\omega=0}$ is the deformation rate mean of the non-optimized case (before applying crucible rotation and modifying the temperature gradient).

This simply implies that maximizing the objective function y is equivalent to minimizing the interface shape deformation over time.

Initial numerical calculations were performed to gauge the realistic rotational speed and temperature gradient ranges for this system. Results indicated that applying very high rotational speeds (more than 200 rpm) or temperature gradients (more than 2.5 K/mm) is detrimental to the dissolution and growth processes and causes odd interface shape deformations. Therefore, in this numerical model, the rotation speed range and temperature gradient range were limited to less than 200 rpm and 2.5 K/mm respectively. In addition, two different temperature gradients were selected since subjecting the system to a relatively lower temperature gradient near the feed crystal (compared to the seed crystal), promoted a less concave growth interface shape. Thus, $(\frac{\Delta T}{\Delta Y})_1$ and $(\frac{\Delta T}{\Delta Y})_2$ were designated as the temperature gradients for the upper ($Y \geq 25$ mm) and lower ($Y < 25$ mm) regions of the sandwich sample respectively.

After multiple iterations, the optimum growth conditions for a more desirable interface shape were obtained as follows:

$(\frac{\Delta T}{\Delta Y})_1 = 0.23$ K/mm $(\frac{\Delta T}{\Delta Y})_2 = 0.81$ K/mm $\omega = 60$ rpm

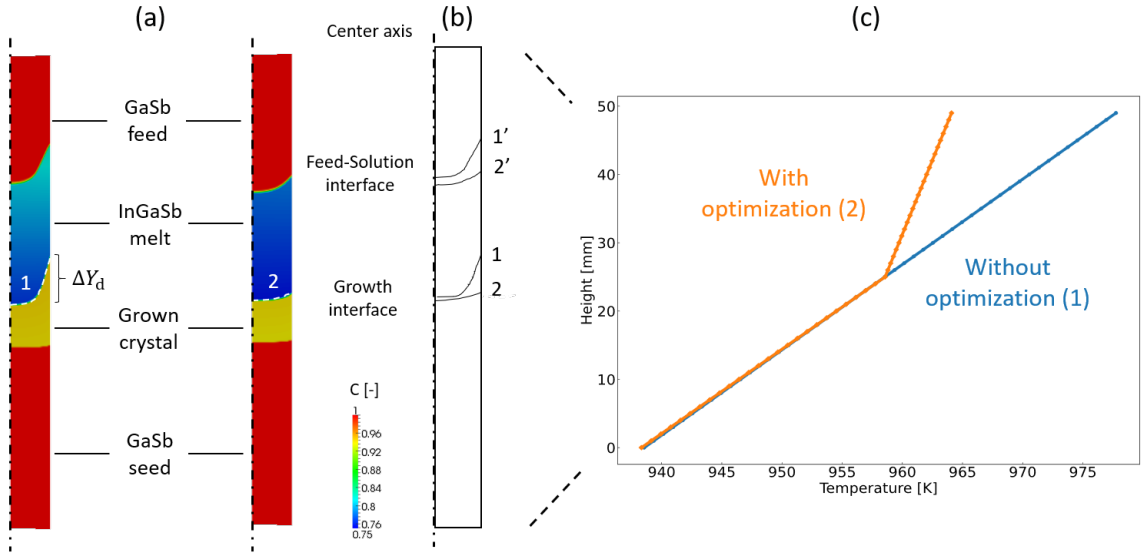

Figure 4.2. GaSb concentration distribution (a), interface shapes (b) and temperature gradients (c) of the optimized and non-optimized cases.

Figure 4.2 illustrates the effects of constant crucible rotation and temperature gradient change on the concentration distribution (**Fig. 4.2(a)**) and interface shapes (**Fig. 4.2(b)**). Initially, both of the growth and feed interfaces were highly concave. After optimization, a flatter growth and feed interface shapes are obtained and the GaSb concentration in the melt is overall more uniform compared to the initial case. By using a smaller temperature gradient near the feed region, as shown in **Fig. 4.2(c)**, there is a diminishment in the feed dissolution rate, therefore a decrease in the solute concentration in the melt. In addition, under the effect of the centrifugal force, due to its lower melting point, InSb, which represents the heaviest compound in the InGaSb solution, is pulled towards the wall side where it remains liquid at relatively low temperatures, promoting hence a desirable flat interface shape.

The time variation of the deformation degree ΔY_d of the growth interface (melt/InGaSb crystal interface) is shown in **Fig. 4.3**. From the figure, the degree of deformation of the non-optimized case is seen to rapidly increase with time and reach a large value of about 5.4 mm after 47.5 h of growth time. After optimization, the degree of deformation is significantly reduced and throughout the whole crystal growth process does not exceed the value of 0.8 mm. From the computed results, it is deduced that subjecting the system to two different temperature gradients (with a smaller temperature gradient near the feed crystal) and rotating the crucible is sufficient to change the solute concentration distribution, reduce the growth interface deformation degree and promote the transition to a flatter shape.

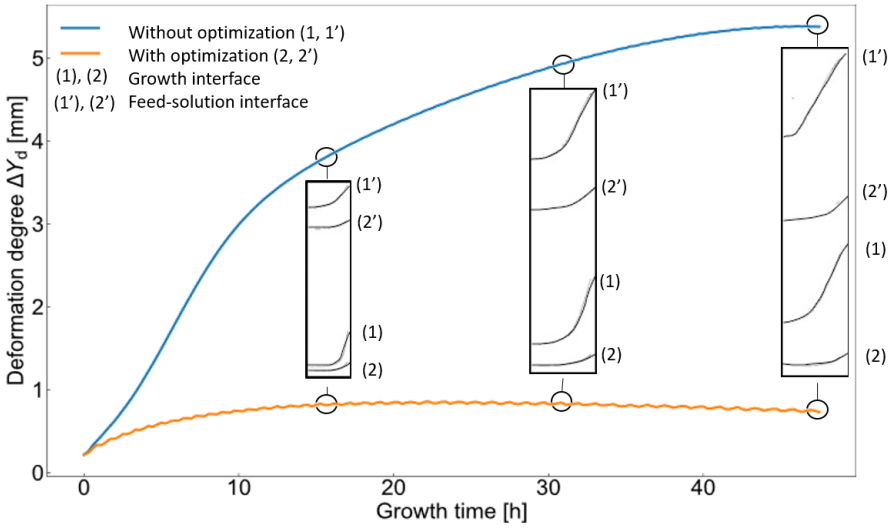

Figure 4.3. Comparison between the deformation degree over time of the crystal growth interface and feed-solution interface with and without Bayesian optimization.

4.3.2 Reinforcement learning: Adaptive control recipe

In the previous section, for simplicity and due to Bayesian optimization limitations, we only considered constant control parameters and one objective function (desirable growth interface shape). As a next step, we fixed the optimized temperature gradients and varied the crucible rotation rate values with time. Our goal is to both maximize the growth rate and maintain a flat growth interface throughout the whole growth process. Consequently, we consider another optimization method which is reinforcement learning.

In artificial intelligence, more precisely in machine learning, reinforcement learning consists in learning the actions a_t to be taken by an autonomous agent from the experiments to optimize a quantitative reward over time. The agent is immersed in an environment and makes decisions according to its current state s_t. In return, the environment provides the agent with a reward r_t, which can be positive or negative. The agent seeks, through iterated experiments (or simulations), an optimal decisional behavior (called strategy or policy, which is a function associating the current state with the action to be executed), in the sense that it maximizes the sum of rewards over time:

$$R_{\max} = \max \mathbb{E}\left[\sum_{t=0}^{\tau} \gamma^t r_t \mid a_t = \pi_\Theta\left(s_t\right)\right] \tag{4.10}$$

where t is the discrete time step when the interaction takes place, γ is the discount factor (ranging from 0 to 1), π_Θ is the policy function described here by the Artificial Neural Networks and Θ is the weights.

As computing technology advances, reinforcement learning techniques are rapidly finding new applications, therefore their implementation in our optimization study. A similar method was

used by Wang *et al.*[109] to find the optimal control values of the Lorentz force in radio frequency (RF) top-seeded solution growth (TSSG) process for the growth of uniform SiC crystals with a higher growth rate.

The present reinforcement learning model training is based on an episode; the model learns an active control strategy in a limited time, analyzes the acquired results and resumes learning with a new episode. As shown in **Fig. 4.4**, one episode of the learning process interacts with the CFD simulation of InGaSb crystal growth process. The agent interacts with the environment via a state inquiry, an action decision is made during the simulation at every t = 1000 seconds and one episode training lasts 10000 seconds. The states in this model are chosen as the solid-liquid interface positions or heights. The control value a in the initial case is equal to 1.0 (optimized control parameters from Bayesian optimization) and the agent imposes actions on the simulation (more precisely on the crucible rotation speed) such as:

$$\omega_t = a_t \cdot \omega_{BO} \tag{4.11}$$

The objective of reinforcement learning is, in addition to flattening the growth interface shape

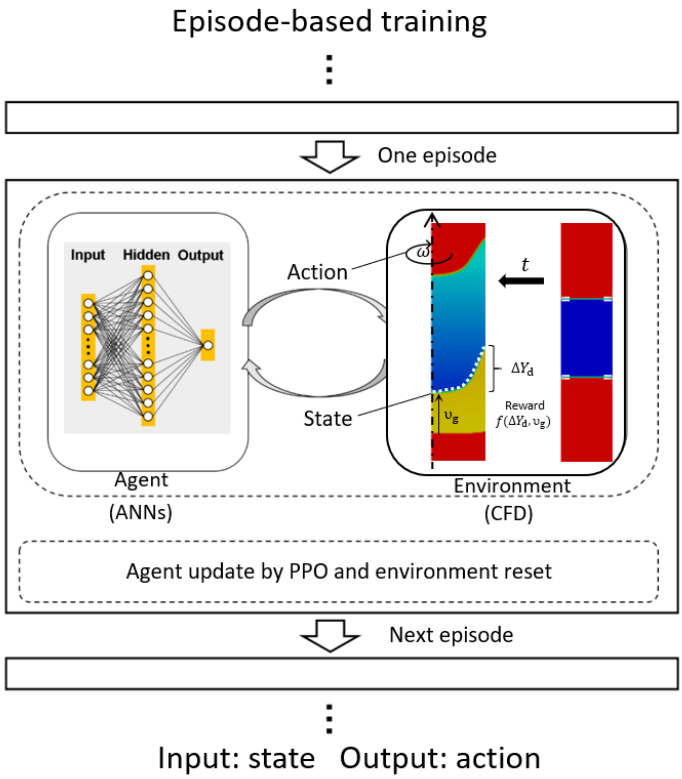

Figure 4.4. Illustration of a simplified reinforcement learning model for the InGaSb crystal growth process.

over time, to improve the growth rate, thus, the instantaneous reward function r_t consists of

two contributions: a negative contribution from the deformation rate and a positive contribution from the growth rate.

$$r_t = -0.01\Delta Y_{dt} + V_t \tag{4.12}$$

The growth rate is defined as $V = \frac{l}{t_{growth}}$ where l is the crystal growth length and t_{growth} is the elapsed time from the beginning of the growth. Due to the large order difference between ΔY_d and V, a factor of 0.01 is set to balance the growth rate contribution. The agent consists of simple feed-forward ANNs with a hidden layer of 512 neurons. The discount factor τ is set as 0.95. Proximal Policy Optimization PPO algorithm, which belongs to the policy gradient class, is used to update the agent. Details regarding this type of policy gradient can be found in this article [112].

After adapting the hyperparameters and algorithm mentioned above, we performed a reinforcement learning training for our system. The reward of each training episode increases quickly and converges after about 50 episodes as shown in **Fig. 4.5(a)**. We considered that the policy at the 60th episode can represent the optimal one and it was chosen to control the initial simulation case for over 100000 seconds (which is 10 times longer than the training time). **Figure 4.5(b)** shows the action values a_t over time of the selected corresponding control strategy. The values of the crucible rotation rate for this adaptive control recipe follow therefore the same tendency (**Fig, 4.5(c)**).

The crystal growth rates at the center axis are calculated and compared in **Fig. 4.6** in the case of utilizing only Bayesian optimization and in the case of combining it with reinforcement learning. It can be seen that, by using the developed control recipe, there was an increase of about 18% in the crystal growth rate.

Figure 4.7 shows the time variation of the crystal growth interface deformation degree ΔY_d for the three cases: non-optimized, fixed recipe and adaptive control method. It is clear that utilizing a reinforcement learning model further reduces the degree of deformation (down to a value of 0.5 mm) and helps keep a flat interface shape throughout the entire crystal growth process. Solute concentration distributions and growth interface shapes after 30 hours of growth are also shown in **Fig. 4.8**.

4.4 Conclusion

In order to investigate the conditions to grow semiconductor crystals with a flatter solid-liquid interface, a numerical simulation study was carried out for controlling the growth interface shape of InGaSb crystals in the Vertical Gradient Freezing (VGF) method under microgravity conditions. The simulation results show that, by applying crucible rotation and different temperature gradients along crucible, a flatter growth interface and a high growth rate can be

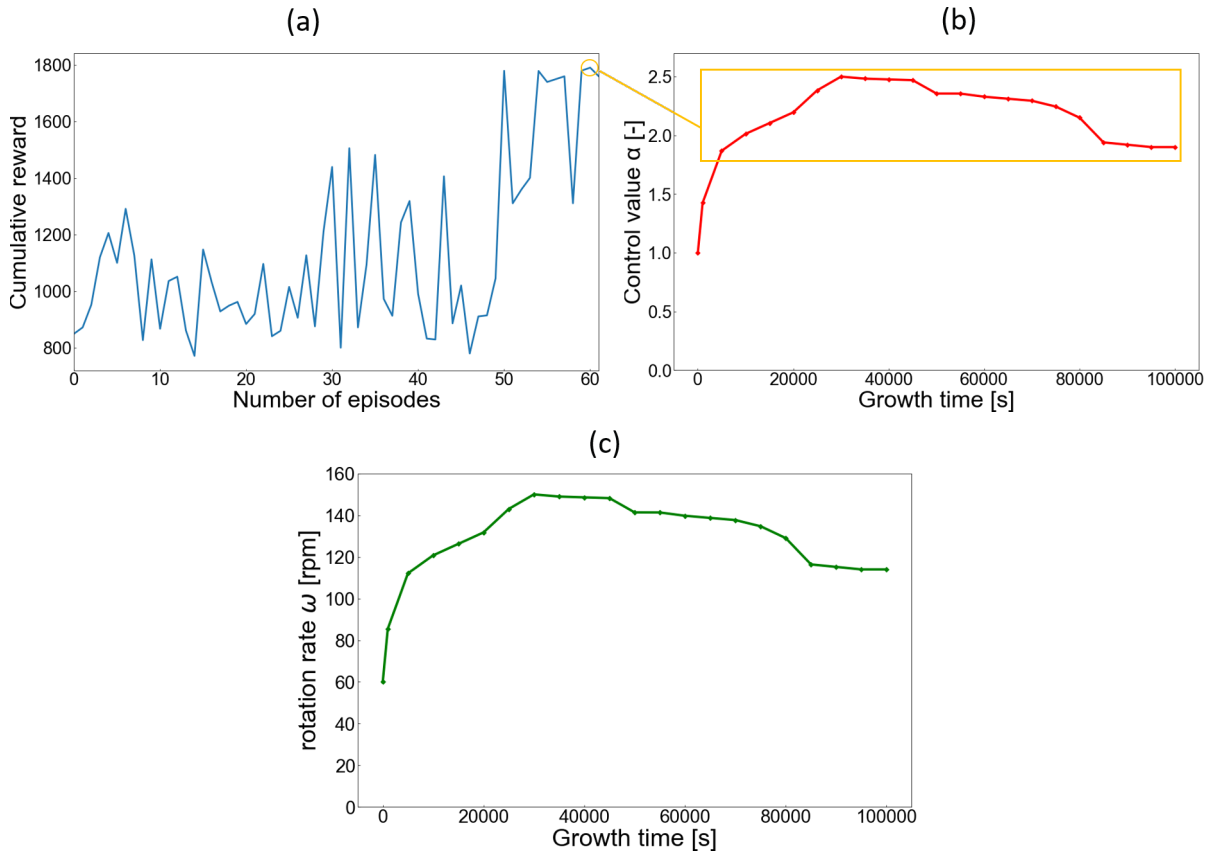

Figure 4.5. Cumulative reward for each episode of the learning process (a), control strategy at the 60th episode (b) and corresponding rotation rate over time (c).

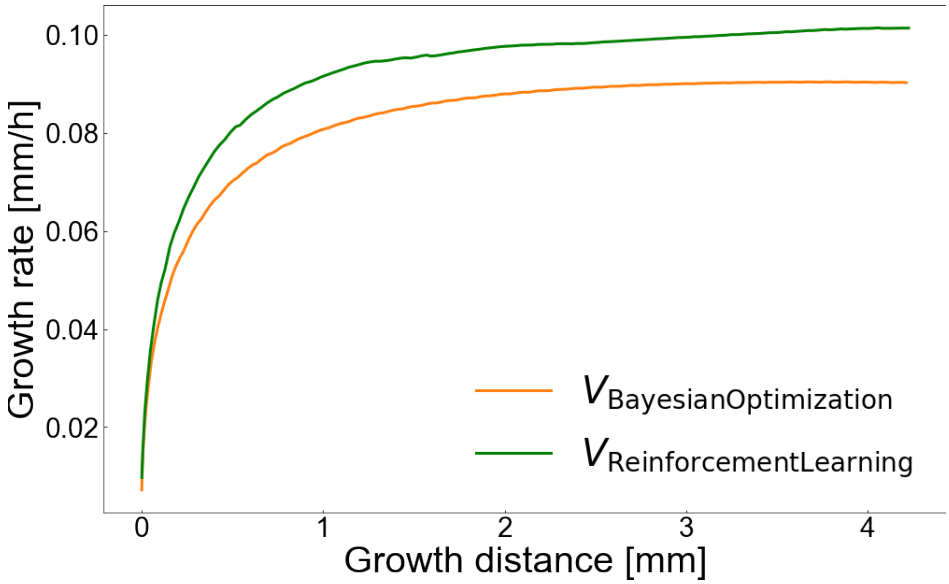

Figure 4.6. Growth rates comparison between the controlled (reinforcement learning) and non-controlled (Bayesian optimization) cases.

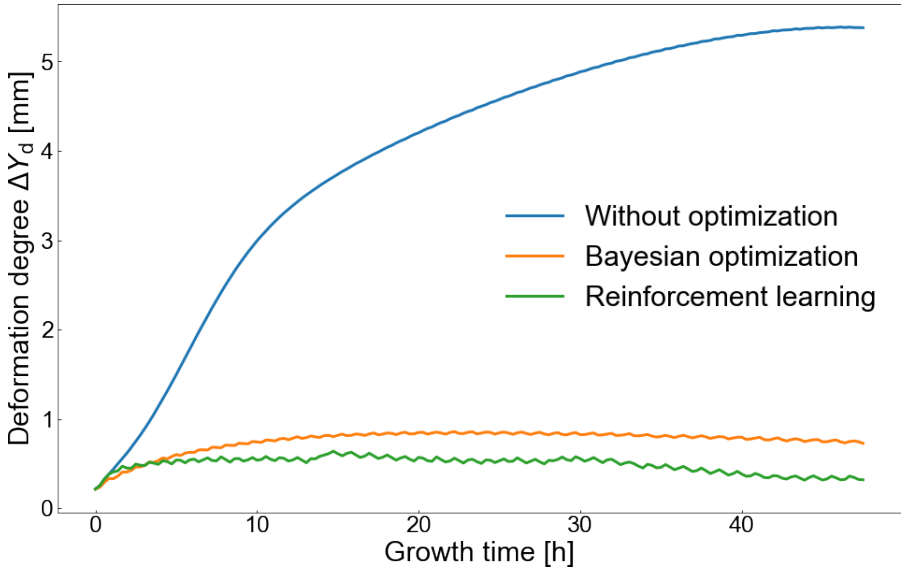

Figure 4.7. Comparison between the interface shape deformation degree over time with and without optimizations.

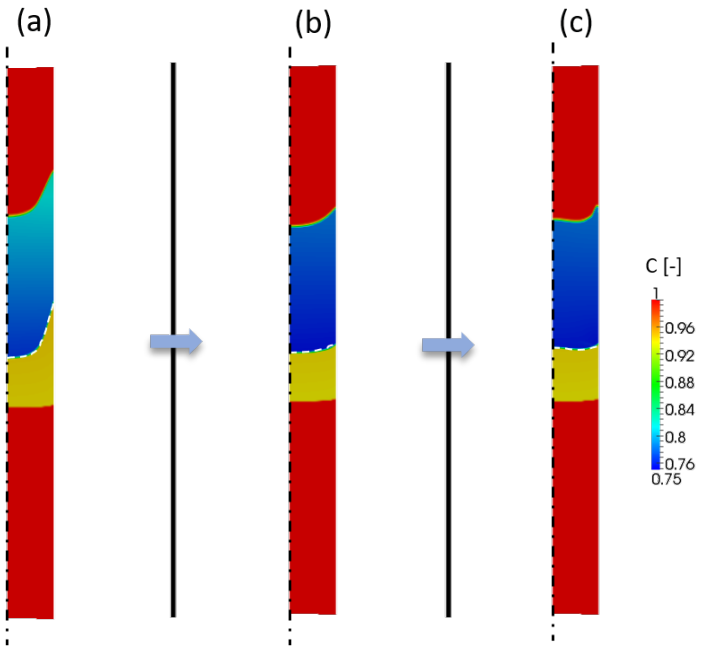

Figure 4.8. GaSb concentration distribution of the non-optimized case (a), after utilizing Bayesian optimization (b) and reinforcement learning (c).

maintained throughout the growth process. The optimum growth conditions for the desired interface shape were obtained utilizing machine learning methods, namely Bayesian optimization and reinforcement learning to resolve the computational demand issue and considerably accelerate the optimization process. Bayesian optimization was utilized first to optimize the temperature gradient and reduce the growth interface curvature. Afterwards, a trained reinforcement model

was added to the optimization algorithm which resulted in growth rate improvement and interface shape flatness throughout the growth stage. The developed adaptive control recipe can be implemented for the growth of high quality InGaSb crystals under normal gravity conditions, as a way to quickly find the best growth conditions and parameters to be used for ground-based experiments. Trials remain to be conducted for the application of these optimization methods in other crystal growth systems in order to validate their usefulness and merits.

Chapter 5

A numerical study for the growth of InGaSb crystals with a flatter interface by Vertical Gradient Freezing method under normal gravity and utilizing Bayesian optimization

5.1 Background and purpose

The growth of high quality InGaSb crystals with desired properties is difficult due to the adverse effect of Earth's gravity. It gives rise to compositional nonuniformity and micro-cracks in the grown crystals, complex heat and mass transfer in the vicinity of the growth and dissolution interfaces, and strong natural convection in the melt [24, 25, 26].

This chapter aims to address these important issues by numerically investigating the VGF growth process of InGaSb crystals in a sandwiched structure of GaSb(seed)/InSb/GaSb(feed). Studies carried out in the last decades have clearly shown that the control of natural convection in the melt plays a key role in optimization of growth processes. Industrial demand is to increase crystal growth yield without compromising the quality. This requires a precise control of convection in the melt. To this end, there have been two main approaches [44]: i) Mechanical control: such as crucible or/and crystal rotation, and ii) Use of external forces: such as applied magnetic fields in metallic semiconducting melts.

These techniques serve two main purposes: damping convective flow fluctuations that can adversely affect growth rate, growth interface shape, and nucleation, and facilitating a better melt mixing, particularly for the growth of doped crystals to ensure homogenized dopant distributions. In our previous work [113], by rotating the crucible according to a specific program, we

achieved an optimal control of growth interface shape during the VGF growth of InGaSb under microgravity. In addition, some studies have shown that applied magnetic fields can be used to suppress natural convection in the melt ([114, 107, 45, 109]). Hence, in this study we considered the applications of both approaches; the use of crucible rotation and applied magnetic field to effectively control the growth of InGaSb crystals under normal gravity, and minimize the undesirable effects of natural convection on the growth interface shape.
Computational Fluid Dynamics (CFD) is a powerful tool for predictions in various fields. Depending on the complexity of a system, CFD may require significant computational resources. CFD simulations for large and complex systems take long computing times. For instance, simulating the growth process of InGaSb crystals by VGF method under normal gravity typically takes a few days, especially, if additional system equations, related to the external applied forces for instance, needed to be solved together with the governing equations. To search for optimal crystal growth conditions, simulations must be repeated several times using different values of the control parameters involved (such as crucible rotation speed, magnetic field strength, temperature gradient etc.). To address this issue, we have utilized Bayesian optimization, which proved to be a promising tool for fast predictions of optimal growth conditions leading to high quality InGaSb crystals with a higher growth rate [111, 113]. Bayesian optimization is a robust approach for locating the extremum of objective functions (high growth rate and minimal interface deflection, for instance) that are typically costly to evaluate. It is useful when a closed-form expression for the objective function is unavailable, but observations (which may be noisy) of the function can be obtained at sampled values [93]. In the present study, we numerically investigated the VGF growth of InGaSb alloy crystals with a flatter interface and high growth rate under normal gravity by utilizing the Bayesian optimization.

5.2 Numerical procedure

5.2.1 Simulation model

Growth of InGaSb crystal by the VGF method is realized using a sandwich system of a thin InSb layer placed between thicker sections of GaSb as seen in **Fig. 5.1**. The growth ampoule in the furnace is subjected to a fixed temperature gradient. In this method, the system is heated over the melting point of InSb crystal which melts first. GaSb seed and feed materials then start to dissolve into the InSb melt and forms an InGaSb growth solution. When the solution tends to attain equilibrium under the applied temperature profile, the low-temperature seed interface reaches supersaturation and crystal growth is initiated on the seed interface. Subsequently, the dissolution of the feed crystal supports the continued growth of the InGaSb crystal.
Figure 5.2(a) presents a schematic description of the GaSb(seed)/Te-doped InSb/ GaSb(feed) sandwich-structured system used in the simulations. The sample was stacked in a Quartz tube

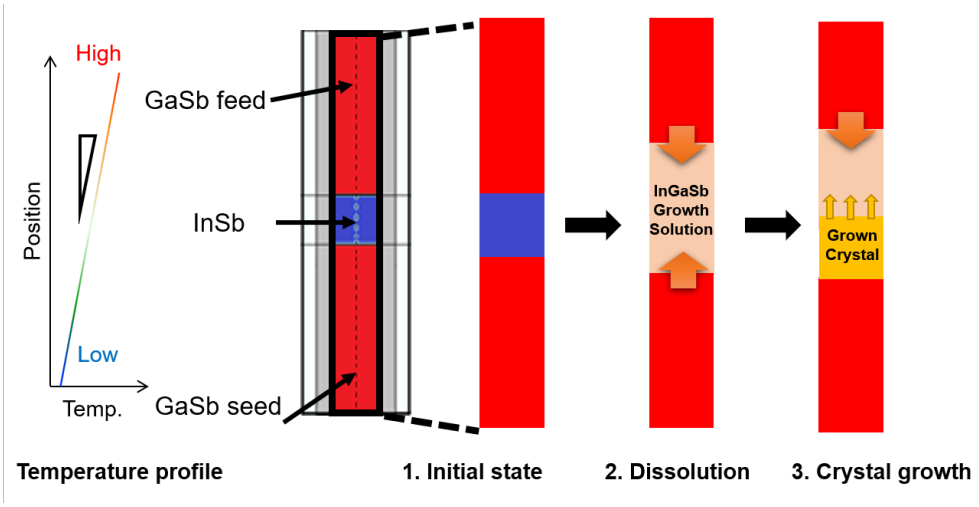

Figure 5.1. Simplified schematic diagram of the temperature profile and stages of InGaSb crystals growth by Vertical Gradient Freezing method [55].

and sealed with Boron Nitride (BN) and carbon sheets. Hence, the computational domain consists of the Crystals, the BN crucible and the Quartz ampoule. The operational parameters and physical properties of these components are given in **Table 3.1**. The temperature gradient in the axial direction is fixed throughout the dissolution and growth processes (**Fig. 5.2(b)**). The system is initially heated at a heating rate of 0.01 K/s up to the target temperature and then maintained unchanged until the end of the growth process. The two-dimensional axisymmetric computational domain used in the numerical calculations is also shown in **Fig. 5.2(c)**. It consists of 132 (x-axis) and 420 (y-axis) segments and was selected after a mesh dependency study performed for different mesh sizes. Ensuring precise and smooth interface shapes requires a domain with a sufficiently high mesh number, particularly in the central area. The level of fineness in the mesh was determined based on striking a balance between computational cost and numerical accuracy.

5.2.2 Governing equations

The following assumptions have been made in the simulation: (i) the liquid phase, i.e. InGaSb growth solution, is an incompressible Newtonian fluid, (ii) Boussinesq approximation holds, (iii) the complete molten state of InSb was regarded as the initial state, and (iv) the temperature dependence of physical properties, such as viscosity, was not considered since the temperature difference in the growth melt is small, only about 2-3 K.

Under the above assumptions, the equations governing of the liquid phase, namely, the continuity, momentum balance, energy balance, and mass transport equations are given as:

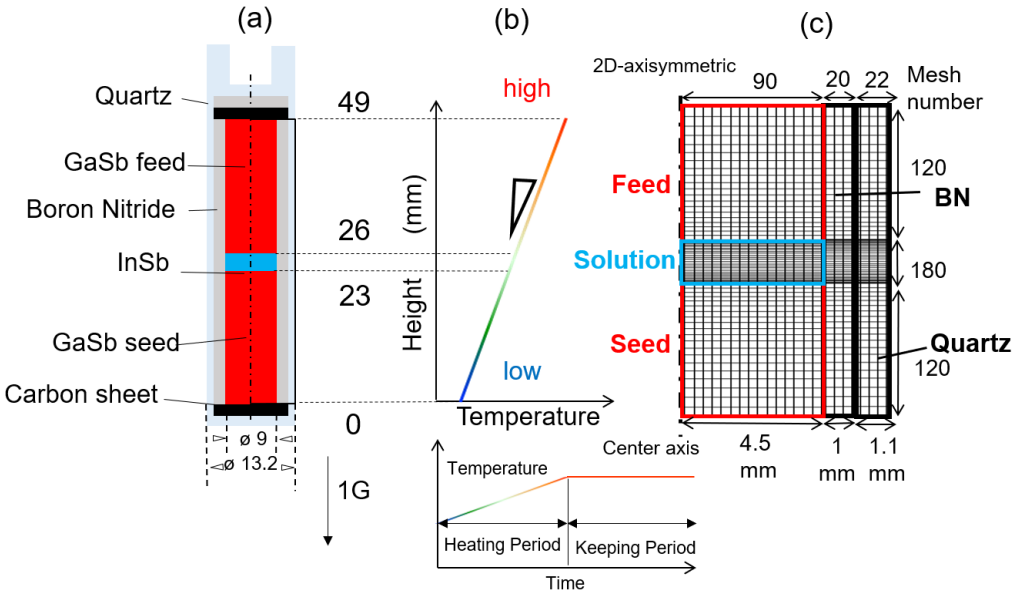

Figure 5.2. Schematic diagrams of the VGF method and computational domain: growth ampoule (a), applied temperature profile (b) and grid system of the simulation (c).

$$\nabla \cdot \boldsymbol{u} = 0 \tag{5.1}$$

$$\frac{\partial \boldsymbol{u}}{\partial t} + (\boldsymbol{u} \cdot \nabla)\boldsymbol{u} = -\frac{1}{\rho}\nabla p + \nu \nabla^2 \boldsymbol{u} + \boldsymbol{g}(\beta_{\mathrm{T}} \Delta T + \beta_{\mathrm{C}} \Delta C) + \frac{\boldsymbol{F}_{\mathrm{r}}}{\rho} + \frac{\boldsymbol{J} \times \boldsymbol{B}}{\rho} \tag{5.2}$$

$$\frac{\partial T}{\partial t} + (\boldsymbol{u} \cdot \nabla)T = \alpha \nabla^2 T \tag{5.3}$$

$$\frac{\partial C}{\partial t} + (\boldsymbol{u} \cdot \nabla)C = \nabla \cdot (D \nabla C) \tag{5.4}$$

where $\boldsymbol{u}$ is flow velocity, ρ melt density, p pressure, ν kinematic viscosity, $\boldsymbol{g}$ gravitational acceleration, β_{T} thermal expansion coefficient, β_{C} solutal expansion coefficient, T temperature, α thermal diffusivity, $\boldsymbol{F}_{\mathrm{r}}$ centrifugal force term, $\boldsymbol{J}$ induced electric current density, $\boldsymbol{B}$ magnetic field, C solute concentration and D represents the diffusion coefficient of GaSb in InSb melt expressed as [111]:

$$D = 2.7 \cdot 10^{-8} \cdot e^{-3 \cdot C} \tag{5.5}$$

The electric current density $\boldsymbol{J}$ in the Lorentz force term is calculated by Ohm's law:

$$\boldsymbol{J} = \sigma(\boldsymbol{E} + \boldsymbol{u} \times \boldsymbol{B}) \tag{5.6}$$

with the introduction of an electrical potential:

$$\boldsymbol{J} = \sigma(-\nabla \phi + \boldsymbol{u} \times \boldsymbol{B}) \tag{5.7}$$

the scalar potential ϕ satisfies the electric charge balance equation of:

$$\nabla \cdot \boldsymbol{J} = 0 \tag{5.8}$$

The vertical magnetic field distribution is described by:

$$\boldsymbol{B} = B_0[0\boldsymbol{i} + \boldsymbol{j} + 0\boldsymbol{k}] \tag{5.9}$$

where B_0 is the magnetic field strength.
The solid phase is governed by the following heat conduction equations:

$$\frac{\partial T}{\partial t} = \alpha_{\mathrm{BN}} \nabla^2 T \tag{5.10}$$

$$\frac{\partial T}{\partial t} = \alpha_{\mathrm{Quartz}} \nabla^2 T \tag{5.11}$$

5.2.3 Boundary conditions, discretization and numerical procedure

The top and bottom walls are adiabatic for the temperature field, and no-slip conditions for the flow velocity field are assumed, while the concentration field has a no-flux condition in the normal direction. On the boundaries between the feed and seed crystals, the walls and the seals (BN and Quartz) have no-slip conditions for the flow velocity field, and no-mass and heat fluxes are allowed in the normal direction to the wall and seal boundaries. The temperature profile on the outer walls of the ampoule is the specified temperature gradient. The simulations were performed under the gravity level of 9.81 m/s^2, with a direction aligned with the sandwich system's axis (y-axis) and directed towards the seed crystal.
To discretize the governing equations along with the boundary conditions, the Finite Volume Method (FVM) was applied, and the Pressure Implicit with Splitting of Operators (PISO) algorithm was utilized to handle pressure-velocity coupling. The simulations were carried out using OpenFOAM, an open-source CFD software package (`https://www.openfoam.com/`). In the present study, we utilize the new volume-average continuum model [57]. This is a good choice for simulating the transport phenomena (momentum, mass and heat transport with phase changes) involved in the melts of binary and ternary growth systems. This technique can handle both microscopic and macroscopic considerations together in one system of equations. The solution procedure can be summarized as follows (see also [57, 63]): The governing equations (complemented with additional relationships in terms of phase mass or volume fractions, concentrations of the solid and liquid phases...) are first solved with the available mass fraction field of the liquid phase f_l. The newly estimated T and C values are then used to update the liquid mass fraction f_l field using the phase diagram of InGaSb. This pseudo-binary phase diagram does not exhibit eutectics; therefore, it is divided into two regions, each region having a set of equations used to update the liquid mass fraction f_l field. Also, at this stage, new values of liquid phase concentration C_l and solid phase concentration C_s are updated using the

new f_1 field. The iterative procedure continues until the solution converges. Once the solution has converged, the simulation moves to the next time step where the iterative cycle is followed once again. In summary, the motion of melting/dissolution and solidifying/growth interfaces can easily be traced by calculating the phase volume fractions (therefore identifying the liquid and solid phases in the domain) from the applied temperature and composition profiles, as well as the pseudo-binary phase diagram of InSb-GaSb. Further information regarding the numerical approach and code validation for comparable systems can be found in previous articles [57, 63, 64].

5.2.4 Bayesian optimization

In many engineering control problems, the number of function evaluations is severely limited by time or cost. One way to address this challenge is by utilizing tools such as Bayesian Optimization. Bayesian optimization makes use of the Bayesian methodology of setting a prior over the objective function and combining it with empirical evidence to obtain a posterior distribution. Doing so allows a utility-based selection of the next observation to make on the objective function. This selection must be balanced between exploration (sampling from areas of high uncertainty) and exploitation (sampling areas likely to offer improvements over the current best observation) [93].

Bayesian optimization aims to find the parameter vector $\boldsymbol{x} = (x_0, ..., x_n)^T$ that maximizes a given objective function $y = f(\boldsymbol{x})$ based on the Gaussian process regression (GPR) and using the variance and predicted mean value.

If $\boldsymbol{D}$ is a known data-set obtained by initial trials: $\boldsymbol{D} = \{(\boldsymbol{x}^0, y^0), ..., (\boldsymbol{x}^m, y^m)\}$, and y^{new} is the value of the objective function at the new parameter $\boldsymbol{x}^{new} = ({x_0}^{new}, ..., {x_n}^{new})^T$ predicted by Gaussian process regression using the data-set $\boldsymbol{D}$, then y^{new} follows the Gaussian distribution and its mean value m and variance σ^2 are as follows:

$$m = \boldsymbol{k}^T \boldsymbol{\Sigma}^{-1} \boldsymbol{y} \tag{5.12}$$

$$\sigma^2 = \boldsymbol{K}(\boldsymbol{x}^{new}, \boldsymbol{x}^{new}) - \boldsymbol{k}^T \boldsymbol{\Sigma}^{-1} \boldsymbol{k} \tag{5.13}$$

where

$$\boldsymbol{k} = \begin{pmatrix} \boldsymbol{K}(\boldsymbol{x}^1, \boldsymbol{x}^{new}) \\ \vdots \\ \boldsymbol{K}(\boldsymbol{x}^m, \boldsymbol{x}^{new}) \end{pmatrix} \quad \boldsymbol{\Sigma} = \begin{pmatrix} \boldsymbol{K}(\boldsymbol{x}^1, \boldsymbol{x}^1) & \dots & \boldsymbol{K}(\boldsymbol{x}^1, \boldsymbol{x}^m) \\ \vdots & \ddots & \vdots \\ \boldsymbol{K}(\boldsymbol{x}^m, \boldsymbol{x}^1) & \dots & \boldsymbol{K}(\boldsymbol{x}^m, \boldsymbol{x}^m) \end{pmatrix} \tag{5.14}$$

$\boldsymbol{K}(\boldsymbol{x}^i, \boldsymbol{x}^j)$ is a kernel function used in this research and defined as:

$$\boldsymbol{K}(\boldsymbol{x}^i, \boldsymbol{x}^j) = \theta_0 \exp\left(-\frac{\theta_1}{2} \parallel \boldsymbol{x}^i, \boldsymbol{x}^j \parallel^2\right) + \theta_2 \tag{5.15}$$

θ_0, θ_1 and θ_2 are hyperparameters determined by the maximum likelihood estimation.

Table 5.1 Bayesian optimization algorithm.

1: **for n loops do**
2: Find $\boldsymbol{x}_{n+1}$ by optimizing the acquisition function over the GP: $\boldsymbol{x}_{n+1} = \arg\max_{x} a(\boldsymbol{x}; \boldsymbol{D}_n)$.
3: Sample the objective function and get a new observation $\boldsymbol{y}_{n+1} = f(\boldsymbol{x}_{n+1})$.
4: Augment the data $\boldsymbol{D}_{n+1} = \{\boldsymbol{D}_n, (\boldsymbol{x}_{n+1}, y_{n+1})\}$.
5: Update the statistical model.
6: **end for**

An acquisition function $a(\boldsymbol{x})$ is used in Bayesian optimization in order to decide the next sample point ($\boldsymbol{x}^{\text{next}}$) so as:

$$\boldsymbol{x}^{\text{next}} = \arg\max_{x} a(\boldsymbol{x}) \tag{5.16}$$

This implies that the parameter with the largest value of the acquisition function is the parameter that should be calculated next.
The Bayesian optimization procedure is summarized in **Table 5.1** and performed using a python code (`https://github.com/hkaneko1985/design_of_experiments`) and the machine learning library *scikit-learn* (`https://scikit-learn.org/stable/`).

5.3 Results and discussion

5.3.1 Optimal control parameters

In order to track the solid-liquid interface shape evolution over time, we calculate the deformation degree ΔY_d such as:

$$\Delta Y_d = Y_p - Y_c \tag{5.17}$$

Y_p and Y_c are the growth interface positions at the periphery and the center axis, respectively. The interface positions are determined at each time step from GaSb concentration distribution. A large positive value of ΔY_d indicates an undesirable highly concave growth interface shape and a value closer to zero indicates a favorable flat one.
The growth rate is another important characteristic of the growth process of InGaSb crystals. It is defined as:

$$v = \frac{l}{t_{\text{growth}}} \tag{5.18}$$

where l is the length of the grown crystal and t_{growth} is the elapsed time since the start of the growth process.

Accordingly, we aim to minimize ΔY_d and maximize v by optimizing the applied temperature gradient, and by the application of a vertical static magnetic fields and by also rotating the crucible. Thus, the following control parameters of the growth process are considered: crucible rotation speed ω, temperature gradient $\frac{\Delta T}{\Delta Y}$ and static vertical magnetic field strength B_0. The realistic parametric ranges for this system (available at JAXA's facilities and numerically achievable) are:

$$\begin{pmatrix} \frac{\Delta T}{\Delta Y} \\ \omega \\ B_0 \end{pmatrix} = \begin{pmatrix} \leq 2.5 \text{ K/mm} \\ 0 \sim 200 \text{ rpm} \\ 0 \sim 6 \text{ T} \end{pmatrix}$$

Moreover, we selected two distinct temperature gradients since exposing the system to a relatively lower temperature gradient near the feed crystal (compared to the seed crystal), shows to promote noticeably less deformed growth interface shapes [113]. $(\frac{\Delta T}{\Delta Y})_1$ and $(\frac{\Delta T}{\Delta Y})_2$ are then designated as the temperature gradients for the upper ($Y \geq 25$ mm) and lower ($Y < 25$ mm) regions of the sandwich sample respectively.

The parameter vector $\boldsymbol{x}$ and the objective function y are finally defined as:

$$\boldsymbol{x} = \begin{pmatrix} (\frac{\Delta T}{\Delta Y})_1 \\ (\frac{\Delta T}{\Delta Y})_2 \\ \omega \\ B_0 \end{pmatrix} \qquad y = M_v^* - M_{\Delta Y_\mathrm{d}}^* \tag{5.19}$$

$M*_{\Delta Y_\mathrm{d}}$ and M_v^* are the normalized mean of the deformation rate and growth rate, respectively, such as:

$$M_{\Delta Y_\mathrm{d}}^* = \frac{M_{\Delta Y_\mathrm{d}}}{M_{\Delta Y_\mathrm{d}}^0} \qquad M_v^* = \frac{M_v}{M_v^0} \tag{5.20}$$

where $M_{\Delta Y_d}^0$ and M_v^0 are respectively the deformation rate and growth rate mean of the initial state, which refers to the non-optimized state (without the application of external forces and crucible rotation $(M_{\Delta Y_\mathrm{d}}, M_v)|_{\omega=0}^{B_0=0}$, and under an arbitrary temperature gradient of 0.6 K/mm). In other words, the maximization of the objective function y involves minimizing the concaveness of the interface shape over time, while also maximizing the growth rate.

After several iterations, the optimum growth conditions were obtained to achieve a more desirable interface shape, as follows:

$(\frac{\Delta T}{\Delta Y})_1 = 0.21$ K/mm $\quad (\frac{\Delta T}{\Delta Y})_2 = 0.79$ K/mm $\quad \omega = 70$ rpm $\quad B_0 = 1.3$ T

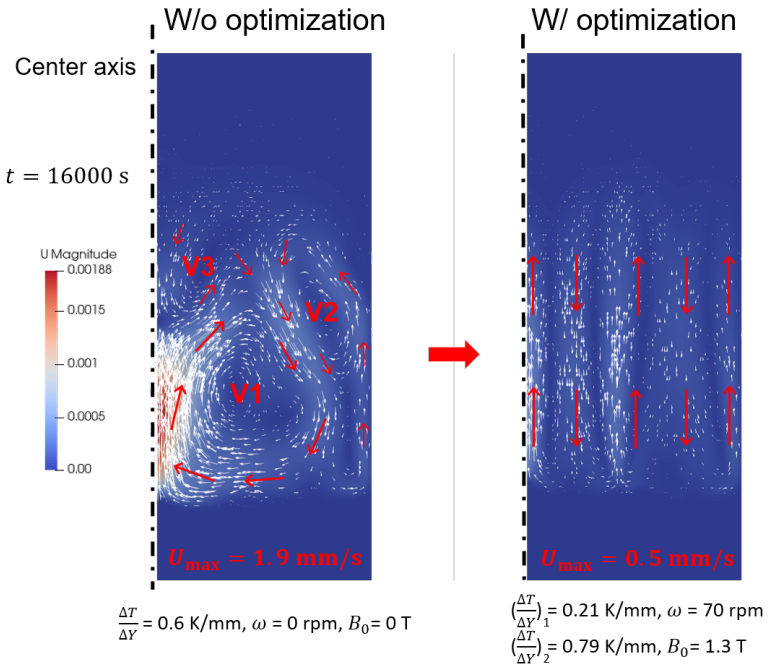

Figure 5.3. Flow velocity fields vectors in the melt before growth starts.

5.3.2 Effects on the velocity field and solute distribution

Figure 5.3 illustrates the velocity field prior to the beginning of the growth process. In the initial state, under normal gravity, there are relatively strong convective and vortex flows (V1, V2, V3) in the melt which promotes solute transport from the center to the periphery. The flow velocity is lower at the peripheries compared to that the center, hence, the solute accumulates at the peripheries while the solution at the center remains undersaturated because of strong convection. This hinders the solution from attaining simultaneous equilibrium; the solution at the peripheries becomes supersaturated first and then the growth is initiated at the peripheries leading to solid-liquid interface deflection. After applying a Vertical Magnetic Field (VMF), the disturbing convective fluctuations are weakened, and the flow velocity magnitude is decreased. VMF affects the melt flow so that strong convection is suppressed and the solute is evenly transported by diffusion from feed to seed in the whole solution region, rather than only at the periphery. This is confirmed by taking a closer look at GaSb concentration distribution in the vicinity of the s/l interface shape in **Fig. 5.4**. By applying VMF, more effective mixing of the solution is achieved leading to radial homogeneity and concentration uniformity.

5.3.3 Effects on the solid-liquid interface and deformation degree

Figure 5.5 shows GaSb concentration distribution and growth interface shape at the beginning of the growth process. In the initial state, because of the reasons mentioned earlier, the crystal growth begins at the peripheries and melt-crystal interface deflection also increases during

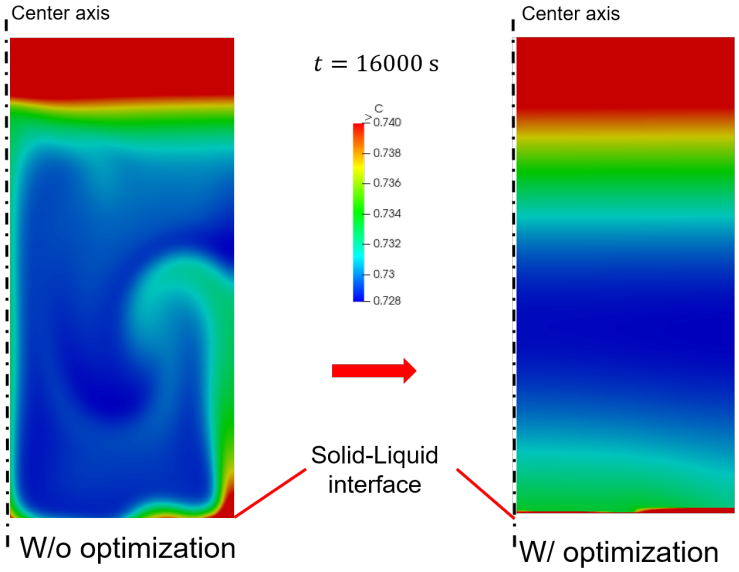

Figure 5.4. Solute concentration distribution at the vicinity of the solid-liquid interface.

the solidification, promoting hence a concave interface shape over time. In the optimal state, because the solution reaches an equilibrium at nearly the same time at the seed interface, growth is initiated almost simultaneously at both the center and peripheries. This helps maintain a flat growth interface shape, thus, growing high quality of InGaSb crystals.

Figure 5.6 compares the solute concentration distribution and interface shapes of the initial and optimal states under normal gravity conditions after 40 h of growth.

In the initial state, the growth and feed interfaces had a highly concave shape. However, after optimization, the interfaces were flattened and a more uniform GaSb distribution in the solution is achieved.

As a result of the centrifugal force effects, the heaviest compound in the InGaSb solution, InSb, which has a lower melting point, is drawn towards the peripheries or wall sides, where it stays liquid at relatively low temperatures. This promotes a desirable flat growth interface shape. The density and melting point of InGaSb, GaSb, and InSb are provided in Table 3.1.

Figure 5.7 shows the time variation of the deformation degree ΔY_{d} of the growth interface. The degree of deformation in the non-optimized case increases rapidly with time, reaching a significant value of about 6 mm after 40 h of growth time. After optimizing the growth conditions, the degree of deformation is significantly reduced and fluctuates around 1 mm throughout the entire crystal growth process. Based on the computed results, it can be concluded that optimizing the temperature gradient, rotating the crucible, and applying a vertical magnetic field effectively influence the melt flow, improve solution homogeneity, and lead to a favorable flatter growth interface shape.

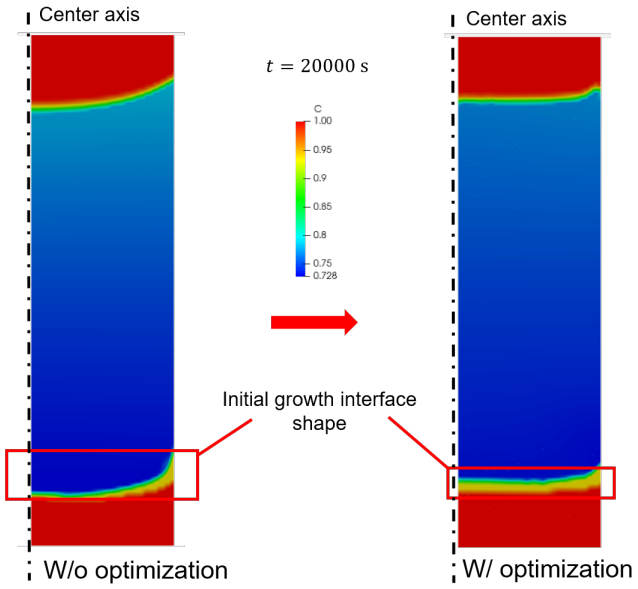

Figure 5.5. GaSb concentration distribution at the beginning of growth and initial growth interface shape.

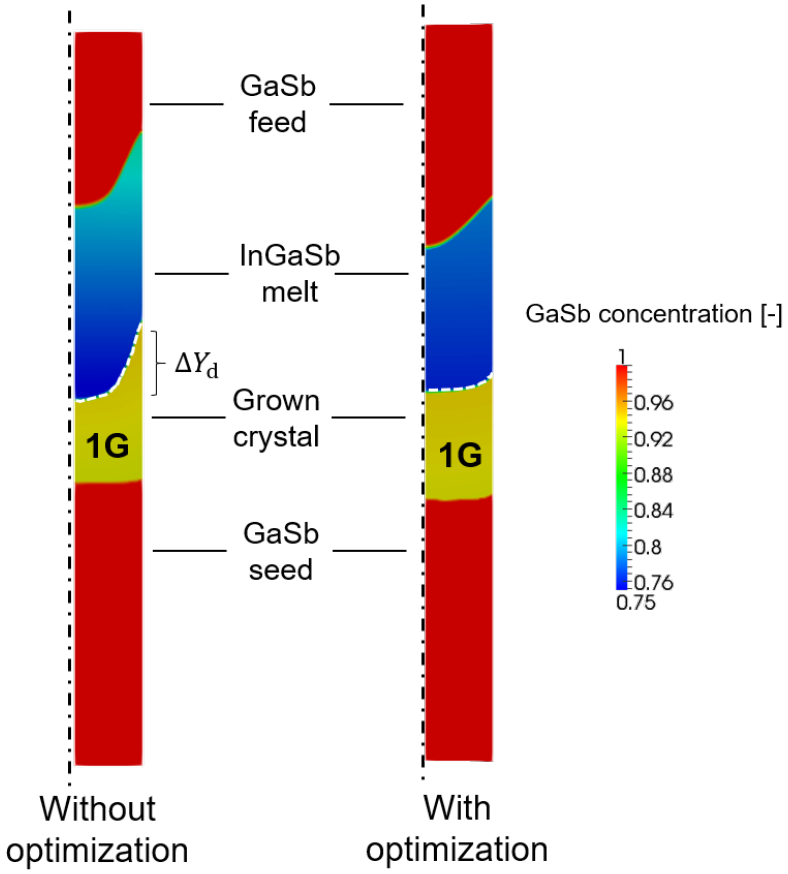

Figure 5.6. GaSb concentration distribution and final crystal-melt interface shape in the initial and optimized states.

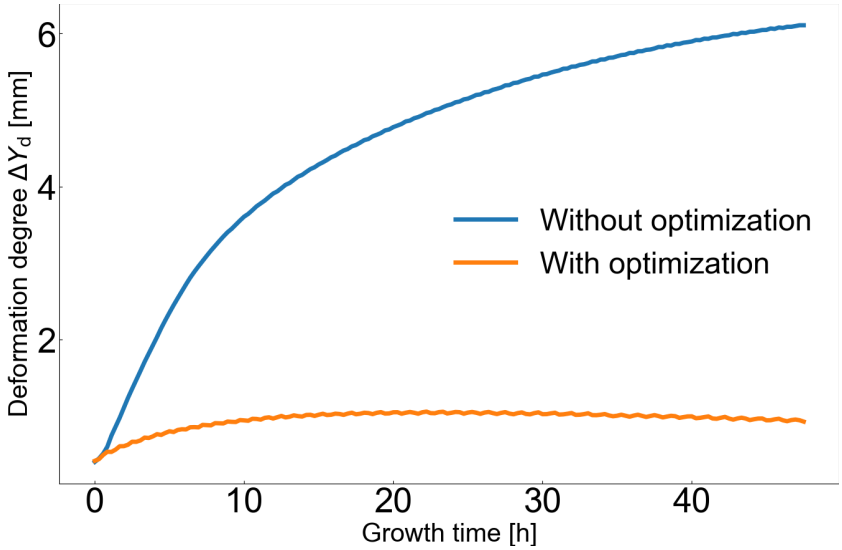

Figure 5.7. Interface shape deformation degree over time in the optimal and non-optimal states.

5.3.4 Effects on crystal growth rate

Figure 5.8(a) illustrates how the crystal growth rate varies along the growth direction in the µG and 1G experiments [55]. The experimental growth rate of the crystal was determined by measuring the distances between growth striations in the grown crystal. These striations were introduced by means of periodic heat pulses that were intentionally applied during the growth process. As for the growth rates calculated from the numerical simulations, they are shown in **Fig. 5.8(b)**. Crystal growth under terrestrial conditions leads overall to lower and non-uniform growth rates. By optimizing the growth conditions, especially the temperature gradients, the growth rate rapidly increases to a maximum of 0.12 mm/h and becomes nearly stable after the growth length of about 2.5 mm. This indicates a diffusion-controlled steady-state growth, similar to the crystal growth under microgravity. One can state that optimizing the temperature field, rotating the crucible and applying an external force achieve a better controlled growth process, and give rise to uniform crystal growth rates in experiments under terrestrial conditions.
It should be noted that the crystal growth rate under microgravity was higher than that under normal gravity, in both the experiments and numerical simulations. Increasing the temperature gradient might further increase the growth rate, but it can lead to more solid-liquid interface deflection (and most likely, lower quality InGaSb crystals) and complete feed dissolution, which should be avoided for post-processing purposes [115, 116].

5.4 Conclusion

In order to investigate the conditions required to grow high quality alloy crystals with a flatter solid-liquid interface, a numerical investigation was performed. The objective was to improve

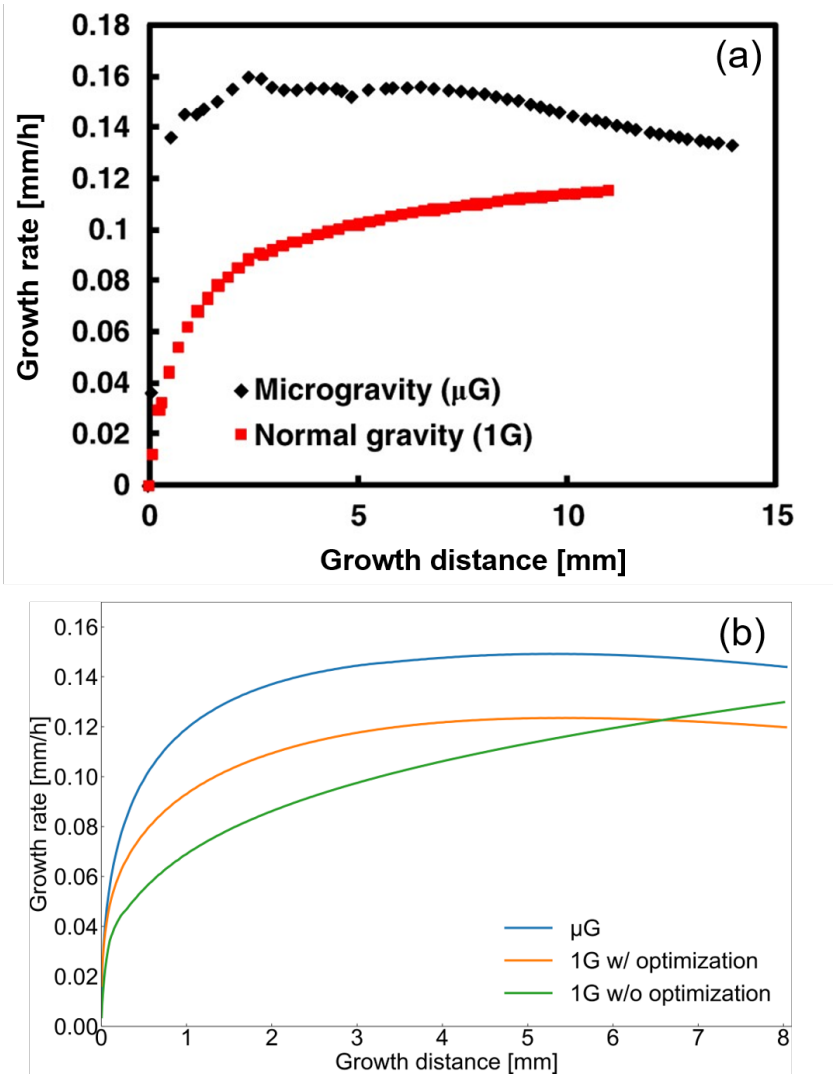

Figure 5.8. Comparison between experimental growth rates (a) and calculated growth rates (b) under μG and 1G conditions.

the crystal growth rate and effectively control the growth interface shape of InGaSb crystals in the Vertical Gradient Freezing (VGF) method under normal gravity conditions. Natural convection significantly contributes to the dissolution and growth of InGaSb semiconductor crystals, and, therefore, affects the solute transport in the solution. The degree of this contribution can be minimized by means of external forces, rotation, etc.

The calculation results show that, by applying a vertical magnetic field, rotating the crucible and optimizing the temperature gradient, the following outcomes can be achieved:

- High and uniform growth rate along the center axis;
- Damping of melt flow oscillations and weakening of adverse convective flows;
- Improved solution homogeneity, and flatter growth interface shape, which are required for the growth of better quality crystals.

To resolve the computational cost and effectively accelerate the optimization process, the optimum growth conditions were acquired using Bayesian optimization, Predicted values of the control parameters can be implemented in future ground-based experiments for the growth of homogeneous high quality InGaSb crystals to provide the needed substrates for device developments in the electronic, optoelectronic and energy conversion fields.

Chapter 6

Thesis summary and future perspectives

6.1 Summary

Firstly, to overcome the limitations of conducting costly and rare space experiments for growing InGaSb alloy crystals under microgravity, we employed in this study a numerical approach using OpenFOAM and the new volume-average continuum model. By developing an adequate numerical analysis technique and utilizing experimental data from the International Space Station (ISS), we aimed to gain insights into InGaSb crystal growth process. Accurate definition of physical properties is crucial in numerical calculations, however, measuring diffusion coefficients on Earth is challenging due to natural convection effects and numerical simulation models using these diffusion coefficients overpredict growth and dissolution rates. To obtain more precise estimations, we employed Bayesian optimization method to analyze the available microgravity experimental results. By incorporating an exponential variation of GaSb diffusion coefficient in InSb melt according to its concentration into the numerical calculations, we achieved good agreement between the experimental and numerical outcomes. Under a diffusion-controlled environment, we concluded that the growth rate, feed and seed dissolution rates, and the final length of the grown crystal are influenced by the values of the diffusion coefficient and their corresponding variation in solute concentration within the melt. This finding highlights the importance of accurately considering the diffusion coefficient in understanding and controlling the growth process of InGaSb crystals under microgravity conditions.

Afterwards, to investigate the growth conditions for semiconductor crystals with a flatter solid-liquid interface, a numerical simulation study under microgravity was conducted. The study focused on controlling the growth interface shape of InGaSb crystals in the Vertical Gradient Freezing (VGF) method. The simulation findings demonstrated that by employing crucible rotation and applying different temperature gradients along the crucible, it was possible to maintain a flatter growth interface and achieve a high growth rate throughout the entire growth process. To optimize the growth conditions for the desired interface shape, machine learning

techniques, specifically Bayesian optimization and reinforcement learning, were utilized. These methods successfully resolved the computational demand issue and significantly accelerated the optimization process. Bayesian optimization was employed initially to optimize the temperature gradient and minimize the curvature of the growth interface. Subsequently, an adaptive control recipe (trained reinforcement model) was incorporated into the optimization algorithm, resulting in improved growth rates and interface flatness throughout the growth stage.
Subsequently, after studying the growth conditions under microgravity, our investigation shifted towards determining the optimal conditions necessary to grow high-quality alloy crystals with a flatter solid-liquid interface under the earth's gravity level and in preparation for future ground experiments. A numerical investigation is performed with the objective of improving the crystal growth rate and effectively controlling the growth interface shape of InGaSb crystals in the VGF method under normal gravity conditions.
It was observed that natural convection plays a significant role in the dissolution and growth of InGaSb semiconductor crystals, impacting the transport of solutes within the solution. The impact of natural convection can be minimized by introducing crucible rotation and external forces such as a vertical magnetic field and optimizing the temperature gradient.
By implementing these measures, several benefits can be achieved, including a high and uniform growth rate along the center axis, reduction of melt flow oscillations, mitigation of adverse convective flows, improved solution homogeneity, and a flatter solid-liquid interface shape. These factors are crucial for the growth of high-quality uniform InGaSb crystals.
To address the computational cost and expedite the optimization process, Bayesian optimization was employed to determine the optimal growth conditions. The predicted values of the control parameters obtained through this optimization approach can be applied in future ground-based experiments for the production of suitable substrates for advancements in electronic, optoelectronic, and energy conversion device technologies.

6.2 Future work

In this thesis, we aimed to gain a fundamental understanding of the transport phenomena and growth mechanism of InGaSb crystals grown on the International Space Station and under normal gravity conditions, using numerical simulations as precise as possible. However, a number of unresolved issues remain:

- The current numerical research primarily focuses on a 2D axisymmetric model to study axial crystal growth and reduce computational costs. However, the growth in the radial direction is also crucial, and its mechanism has not been investigated, leaving it unclear. Therefore, despite the significant computational expense, future research should incorporate three-dimensional numerical simulations to address this aspect.

- Although CFD is a reliable tool, inaccuracies can still happen, therefore explore further tools that are more representative of the physical system and governing equations, such as Physics Informed Neural Networks (PINNs).
- To save computation time, certain physical property changes were neglected in this thesis, including density variations that can lead to volume reduction and bubble generation. It is advisable to consider these small changes as they can have important implications for the crystal growth process.
- As an initial condition, we assumed that GaSb feed started to dissolve in the molten InSb immediately after the complete dissolution of InSb component. However, in actual experiments, once the feed interface reaches the melting point of InSb, the melting process of InSb begins and the feed starts to dissolve in the molten material. Therefore, future simulations should take the initial condition into more careful consideration to better reflect the experimental conditions.
- Consider other techniques to damp convective flows and effectively control melt flow, such as steady/non-steady magnetic fields (RMF, AMF, CMF..).
- The thesis primarily focused on establishing fundamental understandings rather than discussing applications and potential utilization in future industries. It is important to address optimization strategies for future InGaSb crystal manufacturing on Earth, considering practical implications and industrial-scale production. These aspects should be explored in future investigations.

Addressing these remaining issues is crucial for further advancement and comprehensive exploration of InGaSb crystal growth, allowing for a deeper understanding of the process and facilitating practical applications in various industries.

Appendix

Bayesian optimization example code:

```
#Load necessary libraries such as scikit-learn and numpy

import numpy as np
import matplotlib.pyplot as plt
from mpl_toolkits.mplot3d import Axes3D
from matplotlib import cm
import pandas as pd
from scipy.stats import norm
from sklearn.gaussian_process import GaussianProcessRegressor
from sklearn.gaussian_process.kernels import Matern, DotProduct, WhiteKernel, RBF, ConstantKernel
```

```
#Define the acquisition function

def bayesianoptimization(X, y, candidates_of_X, acquisition_function_flag, cumulative_variance=None):
    X = np.array(X)
    y = np.array(y)
    N=np.size(y)

    relaxation_value = 0.01
    delta = 10 ** -6
    alpha = np.log(2 / delta)

    autoscaled_X = (X - X.mean(axis=0)) / X.std(axis=0, ddof=1)
    autoscaled_candidates_of_X = (candidates_of_X - X.mean(axis=0)) / X.std(axis=0, ddof=1)
    autoscaled_y = (y - y.mean(axis=0)) / y.std(axis=0, ddof=1)
    gaussian_process_model = GaussianProcessRegressor(ConstantKernel() * RBF() + WhiteKernel(), alpha=0)
    gaussian_process_model.fit(autoscaled_X, autoscaled_y)
    autoscaled_estimated_y_test, autoscaled_std_of_estimated_y_test = gaussian_process_model.predict(
        autoscaled_candidates_of_X, return_std=True)

    if acquisition_function_flag == 1:
        acquisition_function_values = (autoscaled_estimated_y_test - max(autoscaled_y) - relaxation_value) * \
                                      norm.cdf((autoscaled_estimated_y_test - max(autoscaled_y) - relaxation_value) /
                                               autoscaled_std_of_estimated_y_test) + \
                                      autoscaled_std_of_estimated_y_test * \
                                      norm.pdf((autoscaled_estimated_y_test - max(autoscaled_y) - relaxation_value) /
                                               autoscaled_std_of_estimated_y_test)
    elif acquisition_function_flag == 2:
        acquisition_function_values = norm.cdf(
            (autoscaled_estimated_y_test - max(autoscaled_y) - relaxation_value) / autoscaled_std_of_estimated_y_test)

    elif acquisition_function_flag == 3:
        acquisition_function_values = autoscaled_estimated_y_test+(np.log(N)/N)**0.5*autoscaled_std_of_estimated_y_test

    selected_candidate_number = np.where(acquisition_function_values == max(acquisition_function_values))[0][0]
    selected_X_candidate = candidates_of_X[selected_candidate_number]
    print(np.max(acquisition_function_values))
    print(np.max(y))

    return selected_candidate_number, selected_X_candidate
```

```
#Load the experimental and initial simulation data set for GaSb (111)A crystal orientation
#D0 and b are the two unknowns to be determined using Bayesian optimization
#For simplicity, let's consider only the growth rate results of {D0=2.0e-9, b=0} and (D0=5.0e-9, b=1000) from OpenFOAM

data=pd.read_csv('111A_exp.csv')
x_exp=data['growth distance']
y_exp=data['growth rate']

data=pd.read_csv('111A_D0=2_b=0.csv')
x_D0_2_b_0=data['growth distance']
y_D0_2_b_0=data['growth rate']

data=pd.read_csv('111A_D0=5_b=1000.csv')
x_D0_5_b_1000=data['growth distance']
y_D0_5_b_1000=data['growth rate']
```

```
#Calculate the MSE, therefore, the objective function

y_pred_D0_2_b_0=np.poly1d(np.polyfit(x_exp,y_exp, 10))(x_D0_2_b_0)
err_D0_2_b_0=np.abs(y_pred_D0_2_b_0-y_D0_2_b_0)

y_pred_D0_5_b_1000=np.poly1d(np.polyfit(x_exp,y_exp, 10))(x_D0_5_b_1000)
err_D0_5_b_1000=np.abs(y_pred_D0_5_b_1000-y_D0_5_b_1000)

X=np.array([[2.0e-9,0],[5.0e-9,1000]])
y=np.array((-np.mean(err_D0_2_b_0**2),-np.mean(err_D0_5_b_1000**2)))
```

```
#Candidates sampling within the parameters range considered

n=301
m=101
candidates_of_X=[]
list1=[]
for i in range(n):
    for j in range(m):
        a=2e-9+i*(3e-9)/(n-1)
        b=j*1000/(m-1)
        list_1=[a,b]
        candidates_of_X.append(list_1)
```

```
#Perform the Bayesian optimization using 3 different types of acquisition functions

bayesianoptimization(X, y, candidates_of_X, 1, cumulative_variance=None) #Use EI to select the next candidate
bayesianoptimization(X, y, candidates_of_X, 2, cumulative_variance=None) #Use PI to select the next candidate
bayesianoptimization(X, y, candidates_of_X, 3, cumulative_variance=None) #Use UCB to select the next candidate
```

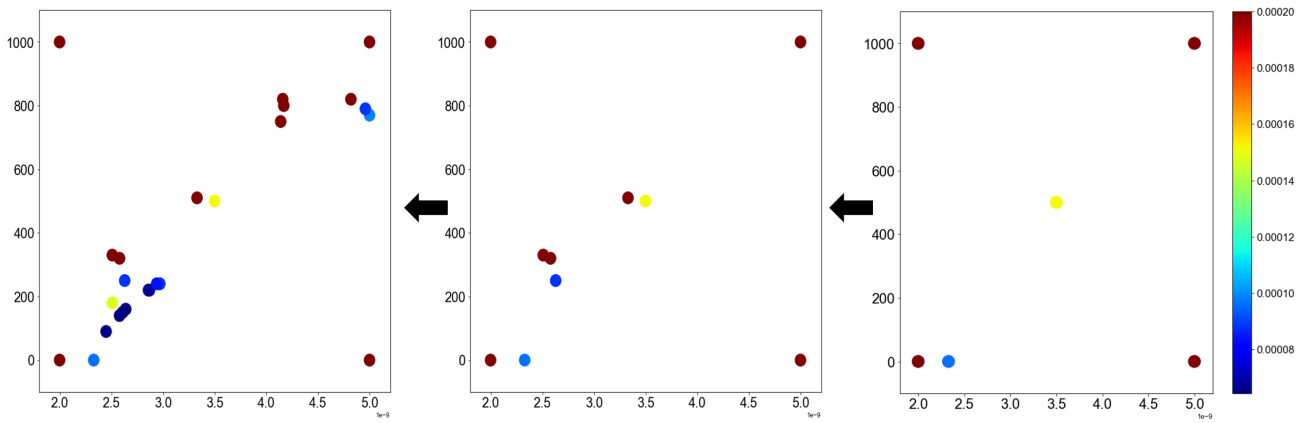

Candidate sampling evolution and corresponding error in the Bayesian optimization procedure.

Bibliography

[1] P. Safa O. Kasap, Principles of Electronic Materials and Devices, McGraw-Hill Education, 2017.
URL https://books.google.co.jp/books?id=2vz3nAAACAAJ

[2] B. Yacobi, Semiconductor Materials: An Introduction to Basic Principles, Microdevices Series, Kluwer Academic/Plenum Publishers, 2003.
URL https://books.google.co.jp/books?id=6FAbQCiaNPEC

[3] S. Sze, K. Ng, Physics of Semiconductor Devices, Wiley, 2006.
URL https://books.google.co.jp/books?id=o4unkmHBHb8C

[4] I. Vurgaftman, J. R. Meyer, L. R. Ram-Mohan, Band parameters for III–V compound semiconductors and their alloys, Journal of Applied Physics 89 (11) (2001) 5815–5875.
URL https://doi.org/10.1063/1.1368156

[5] K. Brennan, The Physics of Semiconductors: With Applications to Optoelectronic Devices, Cambridge University Press, 1999.
URL https://books.google.co.jp/books?id=6JElXbZpX3IC

[6] M. Razeghi, The MOCVD Challenge: A survey of GaInAsP-InP and GaInAsP-GaAs for photonic and electronic device applications, Second Edition, Electronic materials and devices series, CRC Press, 2010.
URL https://books.google.co.jp/books?id=BRq9CNL9wZ8C

[7] P. Bhattacharya, Semiconductor Optoelectronic Devices, Prentice Hall, 1994.
URL https://books.google.co.jp/books?id=_15TAAAAMAAJ

[8] A. Joullie, P. Esquirol, G. Bougnot, Solution growth of n-type gainsb crystals and application to gunn effect, Materials Research Bulletin 9 (3) (1974) 241–250. doi:https://doi.org/10.1016/0025-5408(74)90073-7.
URL https://www.sciencedirect.com/science/article/pii/0025540874900737

[9] R. Biefeld, J. Cederberg, G. Peake, S. Kurtz, The growth and characterization of gainassb and algaassb on gasb by metal-organic chemical vapor deposition, Journal of Crystal Growth 225 (2001) 384–390. doi:10.1016/S0022-0248(01)00886-7.

[10] J. Piprek, Semiconductor Optoelectronic Devices: Introduction to Physics and Simulation, Elsevier Science, 2013.
URL https://books.google.co.jp/books?id=qqVuFz1kDp0C

[11] S. Wang, Lattice Engineering: Technology and Applications, Pan Stanford, 2012.
URL https://books.google.co.jp/books?id=fPGz9IcSS-UC

[12] E. Palik, Handbook of Optical Constants of Solids: Volume 1, Elsevier Science, 2012.
URL https://books.google.co.jp/books?id=h8mEd9no5-kC

[13] S. Adachi, Handbook on Physical Properties of Semiconductors, Information Technology Series, Springer US, 2004.
URL https://books.google.co.jp/books?id=U-4T5Kvfdx0C

[14] P. Capper, C. Elliott, Infrared Detectors and Emitters: Materials and Devices, Electronic Materials Series, Springer US, 2013.
URL https://books.google.co.jp/books?id=bKEACAAAQBAJ

[15] S. Gupta, Optoelectronic devices and systems, PHI Learning, 2014.
URL https://books.google.co.jp/books?id=zmfkBQAAQBAJ

[16] N. Dutta, X. Zhang, Optoelectronic Devices, World Scientific Publishing Company, 2018.
URL https://books.google.co.jp/books?id=pFZoDwAAQBAJ

[17] S. Niu, Z. Wei, X. Fang, D. Wang, X. Wang, X. Gao, R. Chen, Brief review of epitaxy and emission properties of gasb and related semiconductors, Crystals 7 (11). doi:10.3390/cryst7110337.
URL https://www.mdpi.com/2073-4352/7/11/337

[18] H. J. Haugan, G. J. Brown, B. V. Olson, E. A. Kadlec, J. K. Kim, E. A. Shaner, Demonstration of long minority carrier lifetimes in very narrow bandgap ternary InAs/GaInSb superlattices, Applied Physics Letters 107 (13), 131102. doi:10.1063/1.4932056.
URL https://doi.org/10.1063/1.4932056

[19] K. Yang, D. Heinecke, J. Paajaste, C. Kölbl, T. Dekorsy, S. Suomalainen, M. Guina, Mode-locking of 2 μm tm,ho:yag laser with gainas and gasb-based sesams, Opt. Express 21 (4) (2013) 4311–4318. doi:10.1364/OE.21.004311.
URL https://opg.optica.org/oe/abstract.cfm?URI=oe-21-4-4311

[20] M. Zierak, J. M. Borrego, I. Bhat, R. J. Gutmann, G. Charache, Modeling of InGaSb thermophotovoltaic cells and materials, AIP Conference Proceedings 401 (1) (1997) 55–64. arXiv:https://pubs.aip.org/aip/acp/article-pdf/401/1/55/11410082/55_1_online.pdf, doi:10.1063/1.53288.
URL https://doi.org/10.1063/1.53288

[21] S. G. Ghalamestani, M. Ek, M. Ghasemi, P. Caroff, J. Johansson, K. A. Dick, Morphology and composition controlled gainsb nanowires: understanding ternary antimonide growth, Nanoscale 6 (2014) 1086–1092. doi:10.1039/C3NR05079C.
URL http://dx.doi.org/10.1039/C3NR05079C

[22] D. Hurle, Bulk Crystal Growth: Part B. Bulk Crystal Growth, Handbook of Crystal Growth, Elsevier Science, 2016.
URL https://books.google.co.jp/books?id=OESPDAAAQBAJ

[23] S. M. Pimputkar, S. Ostrach, Convective effects in crystals grown from melt, Journal of Crystal Growth 55 (3) (1981) 614–646. doi:https://doi.org/10.1016/0022-0248(81)90121-4.
URL https://www.sciencedirect.com/science/article/pii/0022024881901214

[24] G. M. Blom, T. S. Plaskett, The in-ga-sb ternary phase diagram, Journal of The Electrochemical Society 118 (11) (1971) 1831. doi:10.1149/1.2407845.
URL https://dx.doi.org/10.1149/1.2407845

[25] K. M. Kim, Morphological instability under constitutional supercooling during the crystal growth of InSb from the melt under stabilizing thermal gradient, Journal of Crystal Growth 44 (4) (1978) 403–413. doi:10.1016/0022-0248(78)90006-4.

[26] Y. Hayakawa, Y. Okano, A. Hirata, N. Imaishi, Y. Kumagiri, X. Zhong, X. Xie, B. Yuan, F. Wu, H. Liu, T. Yamaguchi, M. Kumagawa, Experimental and numerical investigations on dissolution and recrystallization processes of Gasb/Insb/Gasb under microgravity and terrestrial conditions, Journal of Crystal Growth 213 (2000) 40–50. doi:10.1016/S0022-0248(00)00340-7.

[27] K. Kakimoto, Heat and mass transfer during crystal growth, Science reports of the Research Institutes, Tohoku University. Ser. A, Physics, chemistry and metallurgy 41 (2) (1996) 107–112.

[28] A. G. Ostrogorsky, M. E. Glicksman, 25 - segregation and component distribution, in: P. Rudolph (Ed.), Handbook of Crystal Growth (Second Edition), second edition Edition, Handbook of Crystal Growth, Elsevier, Boston, 2015, pp. 995–1047. doi:https://doi.org/10.1016/

B978-0-444-63303-3.00025-0.
URL https://www.sciencedirect.com/science/article/pii/B9780444633033000250

[29] D. Zhao, Y. Li, Revealing the factors influencing grain boundary segregation of p, as in si: Insights from first-principles, Acta Materialia 168 (2019) 52–62. doi:https://doi.org/10.1016/j.actamat.2019.02.014.
URL https://www.sciencedirect.com/science/article/pii/S1359645419300928

[30] K. A. Jackson, Segregation, John Wiley & Sons, Ltd, 2004, Ch. 11, pp. 129–142. doi:https://doi.org/10.1002/3527603891.ch11.
URL https://onlinelibrary.wiley.com/doi/abs/10.1002/3527603891.ch11

[31] J. Mullin, Crystallization, Chemical, Petrochemical & Process, Elsevier Science, 2001.
URL https://books.google.co.jp/books?id=Et0EtojQmvsC

[32] L. Liu, N. Chen, F. Gao, Z. Yin, M. Cui, Y. Bai, X. Zhang, Growth of gasb and gainassb layers for thermophotovoltaic cells by liquid phase epitaxy, Proceedings of SPIE - The International Society for Optical Engineering 6841. doi:10.1117/12.755597.

[33] J. Steinshnider, J. Harper, M. Weimer, C. Lin, S. Pei, D. Chow, Origin of antimony segregation in gainsb / inas strained-layer superlattices, Physical review letters 85 (2000) 4562–5. doi:10.1103/PhysRevLett.85.4562.

[34] A. Chandola, Bulk crystal growth and infared absorption studies of gallium indium antimonide, Ph.D. thesis, Rensselaer Polytechnic Institute, New York (Jan. 2005).

[35] N. Murakami, T. Hikida, A. Konno, K. Arafune, T. Koyama, Y. Momose, T. Ozawa, M. Miyazawa, M. Kumagawa, Y. Hayakawa, Growth of homogeneous ingasb ternary alloy semiconductors on insb seed, Journal of Crystal Growth 310 (7) (2008) 1433–1437, proceedings of the 15th International Conference on Crystal Growth (ICCG-15). doi:https://doi.org/10.1016/j.jcrysgro.2007.11.067.
URL https://www.sciencedirect.com/science/article/pii/S0022024807010524

[36] G. Dhanaraj, K. Byrappa, V. Prasad, M. Dudley, Springer Handbook of Crystal Growth, Springer Handbook of Crystal Growth, Springer Berlin Heidelberg, 2010.
URL https://books.google.co.jp/books?id=izaSIl0ahJkC

[37] T. Ozawa, N. Murakami, K. Arafune, Y. Okano, T. Suzuki, M. Kumagawa, Y. Hayakawa, Numerical analysis of constitutional supercooling in ingasb crystal growth under different gravity levels, Journal of Crystal Growth 275 (1-2) (2005) 1507–1512. doi:10.1016/j.jcrysgro.2004.11.183.
URL https://cir.nii.ac.jp/crid/1360292619084572672

[38] P. Rudolph, Thermodynamics, Origin, and Control of Defects, John Wiley & Sons, Ltd, 2008, Ch. 3, pp. 73–101. doi:https://doi.org/10.1002/9783527623440.ch3.
URL https://onlinelibrary.wiley.com/doi/abs/10.1002/9783527623440.ch3

[39] S. L. Pyshkin, Excitonic crystal and perfect semiconductors for optoelectronics, in: S. L. Pyshkin, J. Ballato (Eds.), Optoelectronics, IntechOpen, Rijeka, 2015, Ch. 1.
URL https://doi.org/10.5772/60431

[40] P. Capper, Bulk Crystal Growth of Electronic, Optical and Optoelectronic Materials, Wiley, 2010. doi:10.1002/9780470012086.

[41] F. Rosenberger, Fundamentals of Crystal Growth I: Macroscopic Equilibrium and Transport Concepts, Springer Series in Solid-State Sciences, Springer Berlin Heidelberg, 2012.
URL https://books.google.co.jp/books?id=LCjqCAAAQBAJ

[42] P. Rudolph, Crystal growth from the melt under external force fields, MRS Bulletin 34 (2009) 251 – 258. doi:10.1557/mrs2009.75.

[43] Y. Okano, M. Tachibana, A. Hatano, A. Hirata, Control of crystal-melt interface shape during czochralski growth of oxide single crystals, Journal of Chemical Engineering of Japan 22 (4) (1989) 389–394. doi:10.1252/jcej.22.389.

[44] D. Vizman, 23 - flow control by magnetic fields during crystal growth from melt, in: P. Rudolph (Ed.), Handbook of Crystal Growth (Second Edition), second edition Edition, Handbook of Crystal Growth, Elsevier, Boston, 2015, pp. 909–950. doi:https://doi.org/10.1016/B978-0-444-63303-3.00023-7.
URL https://www.sciencedirect.com/science/article/pii/B9780444633033000237

[45] L. Wang, Y. Takehara, A. Sekimoto, Y. Okano, T. Ujihara, S. Dost, Numerical study of three-dimensional melt flows during the tssg process of sic crystal for the influence of input parameters of rf-coils and an external rotating magnetic field, Crystals 10 (2).
URL https://www.mdpi.com/2073-4352/10/2/111

[46] B. Hong, S. Zhang, L. Zheng, H. Zhang, C. Wang, B. Zhao, Studies on thermal and interface optimization for cdznte crystals by unseeded traveling heater method, Journal of Crystal Growth 546, cited by: 10. doi:10.1016/j.jcrysgro.2020.125776.
URL https://www.scopus.com/inward/record.uri?eid=2-s2.0-85086516193&doi=10.1016%2fj.jcrysgro.2020.125776&partnerID=40&md5=e5bdd9a01db22f7578fc8924daf0a3f9

[47] W. Benz, Crystal growth in space, Advanced Materials 4 (9) (1992) 538–539. doi:https://doi.org/10.1002/adma.19920040902.
URL https://onlinelibrary.wiley.com/doi/abs/10.1002/adma.19920040902

[48] J. Yu, Y. Inatomi, N. Velu, Y. Hayakawa, Y. Okano, M. Arivanandhan, Y. Momose, X. Pan, Y. Liu, X. Zhang, X. Luo, Homogeneous ingasb crystal grown under microgravity using chinese recovery satellite sj-10, npj Microgravity 5. doi:10.1038/s41526-019-0068-1.

[49] Z. Yin, X. Zhang, W. Wang, X. Li, J. Yu, Melt Growth of Semiconductor Crystals Under Microgravity, 2019, pp. 327–360. doi:10.1007/978-981-13-1340-0_13.

[50] C. E. Chang, V. F. Yip, W. R. Wilcox, Vertical gradient freeze growth of gallium arsenide and naphthalene: Theory and practice, Journal of Crystal Growth 22 (4) (1974) 247–258. doi:https://doi.org/10.1016/0022-0248(74)90169-9.
URL https://www.sciencedirect.com/science/article/pii/0022024874901699

[51] Y. Park, S. Min, Vertical gradient freeze and vertical bridgman compound semiconductor crystal growth apparatus capable of applying axial magnetic field, patent US 5769944A (1998).
URL https://patents.google.com/patent/US5769944A/en

[52] A. Vere, Crystal Growth: Principles and Progress, Updates in Applied Physics and Electrical Technology, Springer US, 2013.
URL https://books.google.co.jp/books?id=icy9BwAAQBAJ

[53] C. Szeles, S. Cameron, J. Ndap, W. Chalmers, Advances in the crystal growth of semiinsulating cdznte for radiation detector applications, Vol. 4, 2001, pp. 2424–2428. doi:10.1109/NSSMIC.2001.1009309.

[54] H. J. Kim, Bulk crystal growth process for compositionally homogeneous gallium indium antimonide substrates, Ph.D. thesis, Rensselaer Polytechnic Institute, New York (Aug. 2008).

[55] Y. Inatomi, K. Sakata, M. Arivanandhan, G. Rajesh, N. Velu, T. Koyama, Y. Momose, T. Ozawa, Y. Okano, Y. Hayakawa, Growth of InGaSb alloy semiconductor at the international space station (ISS) and comparison with terrestrial experiments, npj Microgravity 1. doi:10.1038/npjmgrav.2015.11.

[56] Q. Chen, Y. Jiang, J. Yan, M. Qin, Progress in modeling of fluid flows in crystal growth processes, Progress in Natural Science 18 (12) (2008) 1465–1473. doi:https://doi.org/10.1016/j.pnsc.2008.06.003.
URL https://www.sciencedirect.com/science/article/pii/S100200710800302X

[57] T. Yamamoto, H. Mirsandi, X. Jin, Y. Takagi, Y. Okano, Y. Inatomi, Y. Hayakawa, S. Dost, Numerical simulation model by volume averaging for the dissolution process of Gasb into Insb in a sandwich system, Numerical Heat Transfer, Part B: Fundamentals 70 (5) (2016) 441–458. doi:10.1080/10407790.2016.1230397.

[58] C. Beckermann, R. Viskanta, Double-diffusive convection during dendritic solidification of a binary mixture, PhysicoChemical Hydrodynamics 10 (1988) 195–213.

[59] V. Voller, A. Brent, C. Prakash, The modelling of heat, mass and solute transport in solidification systems, International Journal of Heat and Mass Transfer 32 (9) (1989) 1719–1731. doi:https://doi.org/10.1016/0017-9310(89)90054-9.
URL https://www.sciencedirect.com/science/article/pii/0017931089900549

[60] W. Bennon, F. Incropera, A continuum model for momentum, heat and species transport in binary solid-liquid phase change systems—i. model formulation, International Journal of Heat and Mass Transfer 30 (10) (1987) 2161–2170. doi:https://doi.org/10.1016/0017-9310(87)90094-9.
URL https://www.sciencedirect.com/science/article/pii/0017931087900949

[61] V. Voller, C. Prakash, A fixed grid numerical modelling methodology for convection-diffusion mushy region phase-change problems, International Journal of Heat and Mass Transfer 30 (8) (1987) 1709–1719. doi:https://doi.org/10.1016/0017-9310(87)90317-6.
URL https://www.sciencedirect.com/science/article/pii/0017931087903176

[62] J. Vreeman, P. Incropera, Numerical discretization of species equation source terms in binary mixture models of solidification and their impact on macrosegregation in semicontinuous, direct chill casting systems, Numerical Heat Transfer, Part B: Fundamentals 36 (1) (1999) 1–14. doi:10.1080/104077999275749.
URL https://doi.org/10.1080/104077999275749

[63] X. Jin, H. Mirsandi, T. Yamamoto, Y. Takagi, Y. Okano, Y. Inatomi, Y. Hayakawa, S. Dost, Numerical simulation of ingasb crystals growth under microgravity onboard the international space station, JJAP Conference Proceedings 4 (2016) 011107–011107. doi:10.56646/jjapcp.4.0_011107.

[64] X. Jin, T. Yamamoto, Y. Takagi, Y. Okano, Y. Inatomi, Y. Hayakawa, S. Dost, A numerical study on the dissolution process of InGaSb under zero gravity, Int. J. Microgravity Sci. Appl. 34. doi:10.15011//jasma.34.340206.

[65] [link].
URL https://www.openfoam.com/

[66] G. Chen, Q. Xiong, P. Morris, E. Paterson, A. Sergeev, Y. Wang, Openfoam for computational fluid dynamics, Notices of the American Mathematical Society 61 (4) (2014) 354–363. doi:10.1090/noti1095.

[67] K. Mooney, T. Maric, J. Höpken, The OpenFOAM Technology Primer, 2021. doi:10.13140/2.1.2532.9600.

[68] [link].
URL https://paraview.org/

[69] J. Ahrens, B. Geveci, C. Law, Visualization Handbook, Elsevier Inc., Burlington, MA, USA, 2005, Ch. ParaView: An End-User Tool for Large Data Visualization, pp. 717–731.
URL https://www.sciencedirect.com/book/9780123875822/visualization-handbook

[70] K. P. Murphy, Probabilistic Machine Learning: An introduction, MIT Press, 2022.
URL https://probml.github.io/pml-book/

[71] A. Géron, Hands-on machine learning with Scikit-Learn and TensorFlow : concepts, tools, and techniques to build intelligent systems, 1st Edition, O'Reilly, 2019.
URL https://cir.nii.ac.jp/crid/1130289132726962085

[72] C. M. Bishop, Pattern Recognition and Machine Learning (Information Science and Statistics), Springer-Verlag, Berlin, Heidelberg, 2006.

[73] C. Dösinger, T. Spitaler, A. Reichmann, D. Scheiber, L. Romaner, Applications of data driven methods in computational materials designanwendungen von datengetriebenen methoden in computergestütztem materialdesign, BHM Berg- und Hüttenmännische Monatshefte 167. doi:10.1007/s00501-021-01182-3.

[74] R. Ramprasad, R. Batra, G. Pilania, A. Mannodi-Kanakkithodi, C. Kim, Machine learning in materials informatics: recent applications and prospects, npj Computational Mathematics 3 (2017) 54. arXiv:1707.07294, doi:10.1038/s41524-017-0056-5.

[75] U. Toru, T. Yosuke, H. Goki, K. Kentaro, I. Akio, M. Kenta, N. Taka, H. Shunta, T. Miho, The prediction model of crystal growth simulation built by machine learning and its applications, Vacuum and Surface Science 62 (3) (2019) 136–140. doi:10.1380/vss.62.136.

[76] L. Himanen, A. Geurts, A. S. Foster, P. Rinke, Data-driven materials science: Status, challenges, and perspectives, Advanced Science 6 (21) (2019) 1900808. doi:https://doi.org/10.1002/advs.201900808.
URL https://onlinelibrary.wiley.com/doi/abs/10.1002/advs.201900808

[77] R. Pollice, G. dos Passos Gomes, M. Aldeghi, R. J. Hickman, M. Krenn, C. Lavigne, M. Lindner-D'Addario, A. Nigam, C. T. Ser, Z. Yao, A. Aspuru-Guzik, Data-driven strategies for accelerated materials design, Accounts of Chemical Research 54 (4) (2021) 849–860, pMID: 33528245. doi:10.1021/acs.accounts.0c00785.
URL https://doi.org/10.1021/acs.accounts.0c00785

[78] B.-Y. Tseng, C.-W. C. Guo, Y.-C. Chien, J.-P. Wang, C.-H. Yu, Deep learning model to predict ice crystal growth, Advanced Science n/a (n/a) (2023) 2207731. doi:https://doi.org/10.1002/advs.202207731.
URL https://onlinelibrary.wiley.com/doi/abs/10.1002/advs.202207731

[79] K. Ryan, J. Lengyel, M. Shatruk, Crystal structure prediction via deep learning, Journal of the American Chemical Society 140 (32) (2018) 10158–10168, pMID: 29874459. doi:10.1021/jacs.8b03913.
URL https://doi.org/10.1021/jacs.8b03913

[80] D. Fan, L. Yang, Z. Wang, M. S. Triantafyllou, G. E. Karniadakis, Reinforcement learning for bluff body active flow control in experiments and simulations, Proceedings of the National Academy of Sciences 117 (42) (2020) 26091–26098. doi:10.1073/pnas.2004939117.
URL https://www.pnas.org/doi/abs/10.1073/pnas.2004939117

[81] J. Viquerat, J. Rabault, A. Kuhnle, H. Ghraieb, A. Larcher, E. Hachem, Direct shape optimization through deep reinforcement learning, Journal of Computational Physics 428 (2021) 110080. doi:https://doi.org/10.1016/j.jcp.2020.110080.
URL https://www.sciencedirect.com/science/article/pii/S0021999120308548

[82] J. Rabault, M. Kuchta, A. Jensen, U. Réglade, N. Cerardi, Artificial neural networks trained through deep reinforcement learning discover control strategies for active flow control, Journal of Fluid Mechanics 865 (2019) 281–302. doi:10.1017/jfm.2019.62.

[83] N. Dropka, M. Holena, Application of artificial neural networks in crystal growth of electronic and opto-electronic materials, Crystals 10 (8). doi:10.3390/cryst10080663.
URL https://www.mdpi.com/2073-4352/10/8/663

[84] N. Dropka, K. Böttcher, M. Holena, Development and optimization of VGF-GaAs crystal growth process using data mining and machine learning techniques, Crystals 11 (10). doi:10.3390/cryst11101218.
URL https://www.mdpi.com/2073-4352/11/10/1218

[85] R. Sutton, A. Barto, Reinforcement learning: An introduction, IEEE Transactions on Neural Networks 9 (5) (1998) 1054–1054. doi:10.1109/TNN.1998.712192.

[86] K. Arulkumaran, M. Deisenroth, M. Brundage, A. Bharath, A brief survey of deep reinforcement learning, IEEE Signal Processing Magazine 34. doi:10.1109/MSP.2017.2743240.

[87] A. Gosavi, Reinforcement learning: A tutorial survey and recent advances, INFORMS J. Comput. 21 (2009) 178–192.

[88] T. P. Lillicrap, J. J. Hunt, A. Pritzel, N. Heess, T. Erez, Y. Tassa, D. Silver, D. Wierstra, Continuous control with deep reinforcement learning, in: Y. Bengio, Y. LeCun (Eds.), 4th International Conference on Learning Representations, ICLR 2016, San Juan, Puerto Rico, May 2-4, 2016, Conference Track Proceedings, 2016.
URL http://arxiv.org/abs/1509.02971

[89] L. P. Kaelbling, M. L. Littman, A. W. Moore, Reinforcement learning: A survey 4 (1) (1996) 237–285.

[90] [link].
URL https://pythongeeks.org/reinforcement-learning-in-machine-le

[91] B. Shahriari, K. Swersky, Z. Wang, R. P. Adams, N. de Freitas, Taking the human out of the loop: A review of bayesian optimization, Proceedings of the IEEE 104 (1) (2016) 148–175. doi:10.1109/JPROC.2015.2494218.

[92] P. Frazier, W. Powell, S. Dayanik, The knowledge-gradient policy for correlated normal beliefs, INFORMS Journal on Computing 21 (4) (2009) 599–613. doi:10.1287/ijoc.1080.0314.
URL https://doi.org/10.1287/ijoc.1080.0314

[93] E. Brochu, V. M. Cora, N. de Freitas, A tutorial on bayesian optimization of expensive cost functions, with application to active user modeling and hierarchical reinforcement learning, CoRR abs/1012.2599.
URL http://arxiv.org/abs/1012.2599

[94] J. Snoek, H. Larochelle, R. P. Adams, Practical bayesian optimization of machine learning algorithms, in: F. Pereira, C. Burges, L. Bottou, K. Weinberger (Eds.), Advances in Neural Information Processing Systems, Vol. 25, Curran Associates, Inc., 2012.
URL https://proceedings.neurips.cc/paper_files/paper/2012/file/05311655a15b75fab86956663e1819cd-Paper.pdf

[95] V. Nguyen, Bayesian optimization for accelerating hyper-parameter tuning, 2019 IEEE Second International Conference on Artificial Intelligence and Knowledge Engineering (AIKE) (2019) 302–305.

[96] V. N. Kumar, Effects of gravity and orientation on the growth properties of InGaSb ternary alloy semiconductors : Experiments under microgravity on board the International Space Station and normal gravity on Earth , Theses, Shizuoka University (2016).
URL http://doi.org/10.14945/00009909

[97] Y. Sato, T. Nishizuka, T. Takamizawa, T. Yamamura, Y. Waseda, Viscosity of molten Gasb and Insb, International Journal of Thermophysics 23 (1) (2002) 235–243. doi:10.1023/a:1013969430449.
URL https://cir.nii.ac.jp/crid/1361981471023658496

[98] C. Stelian, T. Duffar, I. Nicoara, Comparison between numerical simulation and experimental measurement of solute segregation during directional solidification, Journal of Crystal Growth 255 (1) (2003) 40–51. doi:https://doi.org/10.1016/S0022-0248(03)01199-0.
URL https://www.sciencedirect.com/science/article/pii/S0022024803011990

[99] V. N. Kumar, H. Yasuhiro, U. Haruhiko, I. Yuko, An approach to optimize the thermoelectric properties of iii–v ternary ingasb crystals by defect engineering via point defects and microscale compositional segregations, Inorganic Chemistry 58 (17) (2019) 11579–11588. doi:10.1021/acs.

inorgchem.9b01430.
URL https://cir.nii.ac.jp/crid/1360290617843466496

[100] C. Stelian, Convection thermo-solutale et ségrégations chimiques lors de la solidification Bridgman d'alliages semiconducteurs concentrés sous champs externes, Theses, INSTITUT NATIONAL POLYTECHNIQUE DE GRENOBLE (Sep. 2005).
URL https://hal.archives-ouvertes.fr/tel-01338677

[101] [link].
URL https://scikit-learn.org/

[102] [link].
URL https://datachemeng.com/bayesianoptimization/

[103] N. F. Chen, X. Zhong, L. Lin, M. Zhang, Y. Wang, X. Bai, J. Zhao, Comparison of field effect transistor characteristics between space-grown and earth-grown gallium arsenide single crystal substrates, Applied Physics Letters 78 (4) (2001) 478–479. doi:10.1063/1.1342201.
URL https://doi.org/10.1063/1.1342201

[104] E. H. Snell, R. A. Judge, L. Crawford, E. L. Forsythe, M. L. Pusey, M. Sportiello, P. Todd, H. Bellamy, J. Lovelace, J. M. Cassanto, G. E. O. Borgstahl, Investigating the effect of impurities on macromolecule crystal growth in microgravity, Crystal Growth & Design 1 (2) (2001) 151–158. doi:10.1021/cg0055474.
URL https://doi.org/10.1021/cg0055474

[105] Y. Okano, S. Nishino, S. Ohkubo, S. Dost, Numerical study of transport phenomena in the thm growth of compound semiconductor crystal, Journal of Crystal Growth 237-239 (2002) 1779–1784, the thirteenth international conference on Crystal Growth in conj unction with the eleventh international conference on Vapor Growth and Epitaxy. doi:https://doi.org/10.1016/S0022-0248(01)02339-9.

URL https://www.sciencedirect.com/science/article/pii/S0022024801023399

[106] S. Dost, Y. Liu, Controlling the growth interface shape in the growth of cdte single crystals by the traveling heater method, Comptes Rendus Mécanique 335 (5) (2007) 323–329, melting and solidification: processes and models. doi:https://doi.org/10.1016/j.crme.2007.05.011.
URL https://www.sciencedirect.com/science/article/pii/S1631072107000824

[107] Y. Takehara, A. Sekimoto, Y. Okano, T. Ujihara, S. Dost, Bayesian optimization for a high- and uniform-crystal growth rate in the top-seeded solution growth process of silicon carbide under applied magnetic field and seed rotation, Journal of Crystal Growth 532 (2020) 125437. doi:https://doi.org/10.1016/j.jcrysgro.2019.125437.
URL https://www.sciencedirect.com/science/article/pii/S0022024819306529

[108] Y. Dang, C. Zhu, M. Ikumi, M. Takaishi, W. Yu, W. Huang, X. Liu, K. Kutsukake, S. Harada, M. Tagawa, T. Ujihara, Adaptive process control for crystal growth using machine learning for high-speed prediction: application to sic solution growth, CrystEngComm 23 (2021) 1982–1990. doi:10.1039/D0CE01824D.
URL http://dx.doi.org/10.1039/D0CE01824D

[109] L. Wang, A. Sekimoto, Y. Takehara, Y. Okano, T. Ujihara, S. Dost, Optimal control of sic crystal growth in the rf-tssg system using reinforcement learning, Crystals 10 (9). doi:10.3390/cryst10090791.
URL https://www.mdpi.com/2073-4352/10/9/791

[110] Y. Takehara, A. Sekimoto, Y. Okano, T. Ujihara, S. Dost, Explainable machine learning for the analysis of transport phenomena in top-seeded solution growth of sic single crystal, Journal of Thermal Science and

Technology 16 (1) (2021) JTST0009–JTST0009. doi:10.1299/jtst.2021jtst0009.

[111] R. Ghritli, Y. Okano, Y. Inatomi, A. Sekimoto, S. Dost, Estimation of the diffusion coefficient of GaSb in InSb melt using Bayesian optimization and the ISS experimental results, Journal of Crystal Growth 573 (2021) 126280. doi:10.1016/j.jcrysgro.2021.126280.

[112] J. Schulman, F. Wolski, P. Dhariwal, A. Radford, O. Klimov, Proximal policy optimization algorithms (2017). arXiv:1707.06347.

[113] R. Ghritli, Y. Okano, Y. Inatomi, S. Dost, Control of growth interface shape during ingasb growth by vertical gradient freezing under microgravity, and optimization using machine learning, Japanese Journal of Applied Physics 61 (11) (2022) 115502. doi:10.35848/1347-4065/ac99c2.
URL https://dx.doi.org/10.35848/1347-4065/ac99c2

[114] C. Frank-Rotsch, N. Dropka, F.-M. Kießling, P. Rudolph, Semiconductor crystal growth under the influence of magnetic fields, Crystal Research and Technology 55 (2) (2020) 1900115. doi:https://doi.org/10.1002/crat.201900115.
URL https://onlinelibrary.wiley.com/doi/abs/10.1002/crat.201900115

[115] X. Jin, A. Sekimoto, Y. Okano, T. Yamamoto, Y. Hayakawa, Y. Inatomi, S. Dost, Numerical investigation of the effect of heating rate on ingasb crystal growth under zero-gravity, Microgravity Science and Technology 31. doi:10.1007/s12217-019-9698-x.

[116] X. Jin, B. Wang, Numerical investigation of the effects of axial temperature gradient and cooling rate on ingasb crystal growth under microgravity, Journal of Crystal Growth 607 (2023) 127110. doi:https://doi.org/10.1016/j.jcrysgro.2023.127110.
URL https://www.sciencedirect.com/science/article/pii/S0022024823000362

List of Tables

List of Figures

Acknowledgements

I am filled with immense gratitude and appreciation as I write these acknowledgements, reflecting on the invaluable support and encouragement I have received throughout my academic journey.

First and foremost, I would like to express my heartfelt thanks and appreciation to my supervisor, Prof. Okano, for his expertise, knowledge, kindness and encouragement that have pushed me to work hard and stay genuinely interested in my research. He did not care only about the students' research outcomes, but also about our mental health and overall well-being. Prof. Okano has my deepest gratitude as he provided me with the great opportunity to fulfill my dream of pursuing a PhD at a prestigious university such as Osaka University. The completion of this thesis could not have been possible without his valuable guidance, patience and advice.

I am also thankful to Prof. Nishiyama, Prof. Matsubayashi and Dr. Yamamoto for taking time out of their busy schedule and kindly participating in my thesis committee and reviewing this research work. I wish to acknowledge Dr. Yamamoto, Dr. Jin and Mr. Okita, for their valuable research work on the topic of InGaSb crystals growth and improvements made to the numerical code.

A debt of gratitude is also owed to Prof. Inatomi, for the useful research discussions and for providing us with important experimental data. I would like also to express my gratitude to Dr. Kumar for devoting some of his time to explain the experimental procedures in JAXA facilities and providing me with hands-on

experience in the field of crystal growth. Moreover, I thank Prof. Dost for his assistance and for the essential revisions he provided during paper submissions, this also contributed to improving my academic writing skills.

I sincerely thank every member of Okano Laboratory (current and former ones) for their motivating hard work, for stimulating research discussions during seminars, and for providing feedback during rehearsals, leading to improving my presentations prior to domestic and international conferences. I particularly appreciate Mr. Takehara for his invaluable help in solving various problems, for fruitful discussions and for being so friendly. I also acknowledge Dr. Sekimoto for the support he provided, especially during my first months in the laboratory and for his technical help in understanding numerical simulations and parallel computing.

I would like to express my deepest appreciation to the professors of the Department of Chemical Engineering, for their invaluable guidance; I am grateful for the opportunity to learn from them, especially during the doctor colloquium Q&A sessions. Furthermore, I extend my warmest thanks to the staff of the Graduate School of Engineering Science and the Advising Room for the International Students; I could never thank enough Matsuzuki-san, Tasaka-san and Ishikawa-san for their kindness and tremendous help, as well as all the students I met in ARIS. I consider myself privileged to have met such a talented and diverse group of young leaders from around the world with a shared passion for learning and exchange.

Last but not least, I would like to express my profound gratitude and appreciation to my family for their support, love and encouragement throughout my whole life. I am deeply indebted to them, only with their selfless support and unconditional love, I could overcome various difficulties and complete my studies.

Being a student at Osaka University is a rewarding experience, I am extremely

grateful for the wonderful memories and meaningful connections I have made and for all the people that helped me shape my career and myself as a resilient researcher.

Funding and computational resources

This research work received financial support from Grant-in-Aid for Science Research (B) (JSPS KAKENHI, JP19H02491) and (A) (JSPS KAKENHI, JP20H00320). The calculations were carried out using the computational resources provided by The Institute for Information Management and Communication, Kyoto University and The Research Institute for Information Technology (RIIT), Kyushu University.
I would also like to express my deep gratitude to the Japanese Government for awarding me this scholarship (Monbukagakusho-MEXT) to pursue my academic goals and for providing me with a nurturing and empowering academic environment.

List of Publications and Participations

Original papers

1. R. Ghritli, Y. Okano, Y. Inatomi, A. Sekimoto and S. Dost, "Estimation of the diffusion coefficient of GaSb in InSb melt using Bayesian optimization and the ISS experimental results", *Journal of Crystal Growth*, vol. 573, pp. 126280, 2021, publisher: Elsevier, ISSN: 0022-0248. DOI: 10.1016/j.jcrysgro.2021.126280. URL: https://www.sciencedirect.com/science/article/pii/S0022024821002554.

2. R. Ghritli, Y. Okano, Y. Inatomi and S. Dost, "Control of growth interface shape during InGaSb growth by vertical gradient freezing under microgravity, and optimization using machine learning", *Japanese Journal of Applied Physics*, vol. 61, no. 11, pp. 115502, 2022, publisher: IOP Publishing, ISSN: 1347-4065. DOI: 10.35848/1347-4065/ac99c2. URL: https://dx.doi.org/10.35848/1347-4065/ac99c2.

3. R. Ghritli, Y. Okano, Y. Inatomi and S. Dost, "A numerical study for the growth of InGaSb crystals with a flatter interface by Vertical Gradient Freezing under normal gravity and utilizing Bayesian optimization", *Journal of Chemical Engineering of Japan*, vol. 56, no.1, pp. 2222757, 2023, publisher: Taylor & Francis, ISSN: 1881-1299. DOI: 10.1080/00219592.2023.2222757. URL: https://doi.org/10.1080/00219592.2023.2222757.

List of international and domestic conferences

1. R. Ghritli, Y. Okano, Y. Inatomi and A. Sekimoto, "Estimation of Diffusion Coefficient of GaSb into InSb Melt by using Bayesian Optimization Method Based on the ISS Experimental Results", The 32nd Academic Lecture Meeting of The Japan Society of Microgravity Application (JASMAC-32), Online (Zoom), October 2020.

2. R. Ghritli, Y. Okano, Y. Inatomi and S. Dost, "Estimation of diffusion coefficient of GaSb into InSb melt by using Bayesian optimization method based on the ISS experimental results", The 8th Asian Conference on Crystal Growth and Crystal Technology, Online (Zoom), March 2021.

3. R. Ghritli, Y. Takehara, Y. Okano,Y. Inatomi and S. Dost, "Growth interface shape control of InGaSb crystals in the Vertical Gradient Freeze method under microgravity conditions and optimization using machine learning methods", The 33rd Academic Lecture Meeting of The Japan Society of Microgravity Application (JASMAC-33), Online (Zoom), October 2021.

4. R. Ghritli, Y. Okano and Y. Inatomi, "Optimal control of growth interface shape through machine learning in the growth of InGaSb crystal under microgravity", The 53rd Autumn Meeting of the Society of Chemical Engineers of Japan (SCEJ), Shinshu University, Nagano, Japan, September 2022.

5. R. Ghritli, Y. Okano and Y. Inatomi, "Growth interface shape optimization and adaptive process control for InGaSb crystal growth under microgravity using machine learning", The 83rd Japan Society of Applied Physics (JSAP) Autumn Meeting, Tohoku University, Sendai, Japan, September 2022.

6. R. Ghritli, Y. Okano, Y. Inatomi and S. Dost, "Control of growth interface shape in growth of InGaSb by Vertical Gradient Freezing under microgravity and optimization using machine learning", The American Society for Gravitational and Space Research Annual Meeting 2022 (ASGSR 2022), Royal Sonesta Hotel, Houston, USA, November 2022.

Awards

Dr. Mohri Poster Session Encouragement Award (JASMAC-32, JASMAC-33).